UNIVERSIDAD NACIONAL AUTÓNOMA DE MEXICO
POSGRADO EN CIENCIA E INGENIERÍA DE MATERIALES
INSTITUTO DE CIENCIAS FÍSICAS

DIPOLE AND GENERALIZED OSCILLATOR STRENGTH DEPENDENT PROPERTIES OF FREE AND AT EXTREME CONDITIONS SYSTEMS WITH APPLICATIONS TO MATERIAL DAMAGE

TESIS
QUE PARA OPTAR POR EL GRADO DE:
DOCTOR EN CIENCIA EN INGENIERÍA DE MATERIALES

PRESENTA:
CÉSAR MARTÍNEZ FLORES

TUTOR
Dr. REMIGIO CABRERA TRUJILLO
INSTITUTO DE CIENCIAS FÍSICAS

MIEMBROS DEL COMITÉ TUTOR
Dr. JOSÉ IGNACIO JIMÉNEZ MIER Y TERÁN
INSTITUTO DE CIENCIAS NUCLEARES

Dr. GUILLERMO SANTANA RODRÍGUEZ
INSTITUTO DE INVESTIGACIÓN EN MATERIALES

CIUDAD UNIVERSITARIA, CIUDAD DE MÉXICO, AGOSTO 2018

Dipole and generalized oscillator strength dependent properties of free and at extreme conditions systems with applications to material damage
César Martínez-Flores

Supervisor:
Dr. Remigio Cabrera-Trujillo, Instituto de Ciencias Físicas UNAM
Examiners:
Dr. Jacques Soullard Saintrains, IF-UNAM
Dr. Remigio Cabrera Trujillo, ICF-UNAM
Dr. Salvador Cruz Jiménez UAM-I
Dr. Jorge Garza Olguin UAM-I
Dr. Ricardo Méndez Fragoso FC-UNAM

Ph.D. Thesis 2018
Posgrado en Ciencia e Ingeniería de Materiales
Física atómica, molecular y óptica experimentales
Instituto de Ciencias Físicas
Universidad Nacional Autónoma de México
Cuernavaca Morelos, Ap. Postal 43-8, México

Typeset in LaTeX
Ciudad de México, August 2018.

Dipole and generalized oscillator strength dependent properties of free and at extreme conditions systems with applications to material damage

C. Martínez-Flores

Instituto de Ciencias Físicas

Universidad Nacional Autónoma de México

Abstract

In this thesis, I explore the dipole and generalized oscillator strength (DOS and GOS, respectively) derived properties of atomic systems for free and at extreme conditions by means of *ab initio* and numerical approaches with relevance in material damage. For extreme conditions I mean in confinement environments, e.g. atomic systems encaged by fullerene molecules and/or embedded in a plasma. I show results for DOS and GOS derived electronic properties for atoms subjected to confinement environments, e.g. photo-ionization cross section, mean excitation energy, and energy deposition of heavy ions (energy loss). I present the study in next chapters with the following structure. In Chapter 1, I give a general introduction and the purpose of this thesis. In Chapter 2, I show the theoretical approach used in this thesis where I establish the physical properties to study. In the field of energy loss for free atomic systems (no extreme conditions), in Chapter 3, I present results of energy deposition of heavy ions colliding with atoms and molecules within the Bethe's theory. I show that, there is an universal scaling when the electronic stopping cross section and projectile kinetic energy are scaled properly in terms of the target mean excitation energy, I_0, for all projectile-target combinations. Our findings are compared with available experimental data observing a good agreement for high projectile energies. In the same Chapter, continuing with the study of energy deposition for atomic systems, I present preliminary results of the initial target symmetry effect on the GOS and its consequences on the electronic stopping cross section. Our results make evident the relevance of the initial target symmetry on the determination of the stopping cross section. For systems under confinement, in Chapter 4, I consider the case of a hydrogen atom encaged by a C_{60} cavity obtaining the eigenvalues and eigenfunctions from the time-independent Schrödinger equation by means of a finite-differences approach. The C_{60} is described by a model potential that assumes that the fullerene cage has a static electronic configuration. I find that the physical properties are modified strongly and the drastic changes are predominant near the first avoided crossing of the energy levels. In Chapter 5, I present results for a hydrogen atom encaged by an endohedral cavity under the influence of a weak plasma interaction by solving the Schrödinger equation by means of a finite-differences approach. The plasma interaction is described by a Debye-Hückel screening potential. We find that for low screening lengths, the endohedral cavity potential dominates over the plasma interaction by confining the electron within the cavity. For large screening lengths, a competition between both interactions is observed. As a consequence, the DOS and GOS derived properties are modified. In Chapter 6, I present the study of Li atom encaged by an endohedral cavity implementing the Hartree-Fock approach. I find that the DOS and GOS are modified drastically for low values of confinement and as a consequence their derived dependent electronic properties are modified too. Finally, in Chapter 7 I give the general conclusions and perspectives about this scientific research.

Acknowledgements

<div align="right">C. Martínez-Flores, Ciudad de México, August 2018.</div>

Contents

Publications

This thesis is the result of the theoretical study of the dipole and generalized oscillator strength for free atomic systems and at extreme conditions on several interesting research areas. The main results presented in this work constitute my research contribution as a PhD. student. In Paper I and III I show results for free atomic systems. In Paper I, I study the scaling law behavior at high collision energy for the stopping power of heavy projectile ions colliding with atoms and molecules. Paper III analyzes the role of the initial target orbital symmetry on the generalized oscillator strength and their implications on the stopping cross section. In Paper II and IV I present results for atomic systems at extreme conditions. I show results for the hydrogen atom encaged by a C_{60} fullerene molecule in Paper III, and how the dipole and generalized oscillator strength derived properties are modified. Paper IV is about the study of the hydrogen atom encaged by a fullerene molecule and embedded in a plasma interaction. Here, I show results for the dipole and generalized dependent electronic properties. In Paper V, I show results for dipole dependent properties of an endohedral lithium atom under the Hartree-Fock approach. This thesis is based mainly on the scientific work developed in these research papers that are listed in chronological order of appearance.

- **Paper I**: *On the universal scaling in the electronic stopping cross section for heavy ion projectiles.*
  Authors: R. Cabrera-Trujillo, **C. Martínez-Flores**, L.N. Trujillo-López and L.N. Serkovic-Loli.
  Journal: Radiation Effects and Defects in Solids, **171**,1-2, (2016).
  DOI: https://doi.org/10.1080/10420150.2016.1155581
  In 2016, I attended the *8th International Workshop on High-Resolution Depth Profiling (HRDP8)* from August 7-11 at the Western University in London, Ontario, Canada. During the event, this work was presented in the poster session on Tuesday 9, winning the second place in the Student Poster Competition.

- **Paper II**: *Derived properties from the dipole and generalized oscillator strength distributions of an endohedral confined hydrogen atom.*
  Authors: **C. Martínez-Flores** and R. Cabrera Trujillo.
  Journal: J. Phys.B: At. Mol. Opt. Phys. B, **51**, 055203, (2018).
  DOI: https://doi.org/10.1088/1361-6455/aaa662

- **Paper III**: *Effects of the s- and p-orbital target symmetry on the Generalized Oscillator Strength and its role on the electronic stopping cross-section: Preliminary results within a harmonic oscillator approach.*
  Authors: **C. Martínez-Flores** and R. Cabrera Trujillo.
  Journal: Radiation Effects and Defects in Solids, **173**, 1-2, 85-92, (2018).
  DOI: https://doi.org/10.1080/10420150.2018.1442463

- **Paper IV**: *Dipole and generalized oscillator strength derived electronic properties of an endohedral hydrogen atom embedded in a Debye-Hückel plasma.*
  Authors: **C. Martínez-Flores** and R. Cabrera Trujillo.
  Journal: Matter and Radiation at extremes (In press), (2018).
  DOI: https://doi.org/10.1016/j.mre.2018.05.001

- **Paper V**: *The role of unrestricted and restricted Hartree-Fock approach in the dipole oscillator strength derived electronic properties of an endohedral lithium atom.*
  Authors: **C. Martínez-Flores** and R. Cabrera Trujillo.
  Journal: (in preparation).

1
Introduction

The photo-ionization process and the energy deposition of ions (energy loss) are of crucial importance in determining the damage to materials with implications in areas such as material science, plasma physics, radiotherapy, and dosimetry. In the photo-ionization case, the response of atomic systems to ionizing radiation is a dominant process in the universe that involves neutral atoms, molecules, clusters, as well as their ions (positive or negative) and is carried out in many physical systems [1, 2]. These include a variety of astrophysical systems, the upper atmosphere and different types of plasma. The plasma is directly related to the knowledge of the internal structure of materials and their application [3, 4], for example, the plasmas produced by a laser. Here, the interaction of intense laser beams or synchrotron light with the materials leads to changes in phase transitions and the production of hot plume of the material. Thus the investigation of these system has practical interest, e.g. in the deposition of materials [5], in lithography [6], and microscopy [7], among others.

In the study of the energy deposition of swift, heavy bare ions colliding with an atomic or molecular target, Bethe [8] proposed the first quantum mechanical treatment of the problem using perturbation theory for the projectile–target interaction by means of the first Born approximation. From Bethe's theory, the electronic stopping cross section is a function of the mean excitation energy, I_0, that plays a crucial role. This I_0 parameter accounts for the average energy that a target absorbs from the projectile kinetic energy during the collision process. The determination of I_0 is a difficult problem since it requires the knowledge of the full excitation spectrum of the target. For molecular targets, the situation is even more complicated due to the multi-center many-electron problem. In the literature, there have been reported analytic functional fits or universal curves [9, 10] that facilitate the determination of the electronic stopping cross section. These expressions require adjustable parameters for each projectile–target combination. Another approach, is the use of the harmonic oscillator model to account for the electronic stopping cross section [11], which allows us to obtain I_0 using the Virial theorem. Under this approach, in the intermediate to high collision energies, the following question arises: Is it possible to find an universal scaling behavior for the electronic stopping cross section as a function of target properties of atoms and molecules? In the following chapters, I explore this possibility (Paper I).

As mentioned above, in Bethe's approximation, the energy deposition is characterized by the mean excitation energy, I_0. This parameter depends on the target's dipole oscillator strength (DOS) and consequently, on the whole target excitation spectrum. It has been found that the mean excitation energy has a dependence on the target orientation [12, 13]. However this orientational dependence has not been assessed in the generalized oscillator strength (GOS) and its effects in the stopping cross-section, but only through the mean excitation energy. Another important issue that has not been considered before is the initial target orbital symmetry state and the role it plays in the dipole and generalized oscillator strength. Considering the harmonic oscillator approach [11], I formulate the following two questions: How are the generalized oscillator strengths modified if I consider the initial symmetry of the target? and How is the stopping cross section modified? In this work, I present preliminary results on the initial target symmetry effect on the GOS and on the stopping cross section (Paper III).

Furthermore, in the field of atomic systems subjected to different external environments (extreme conditions), there are new challenges to investigate related to changes in their electronic properties

[4, 14, 15, 16]. The study of hydrogenic impurities inside spherical or cilindrical cavities has been related to the promise of applications in photo-voltaic materials, quantum computing, semiconductor nanocrystals, hydrogen storage or medicine treatments [14, 17, 18, 19, 20, 21]. For example, atoms encapsulated inside a fullerene molecule, known as endohedral systems (A@C), or quantum dots which are small impurities that are grown or recorded in semiconductor materials with diameters of a few nanometers. Here, the motion of the electrons is confined in the three spatial directions and when stimulated with an external potential or light, they can only emit/absorpt in certain energy spectra (light of a certain color). This technology is currently used in various electronic devices [19]. Thus, in these problems, you need to have a precise knowledge of the interaction between light and certain materials. Here, the systems encaged in a cavity can be considered as subjected to a spatial confinement.

A consequence of the spatial confinement on the atomic systems is the energy level shift and the modification of the wave function with a consequently change in the dipole and generalized oscillator strength, and therefore consequences in determining the damage to materials through the energy-loss function. Some modified electronic properties are the ionization potential, polarization, the static and dynamic polarizability, hyper-fine splitting, magnetic screening constants, orbital distortion, photo-ionization, mean excitation energy, and the energy deposition of ions (projectile energy loss) or material damage. For example, the photo-ionization of an atom in an endohedral cavity has been studied previously for one-electron and multi-electronic systems finding huge energy resonances consequence of the trapping of incoming and outgoing waves in the endohedral cavity [14, 15, 16, 22, 23, 24, 25, 26, 27, 28, 29, 30, 31].

In the case of a free hydrogen atom, the analytic expressions for the generalized oscillator strength have been available in the literature [32, 33, 34], however for endohedral systems this is not the case. There is no work reporting generalized oscillator strength properties for a hydrogen or lithium atom encaged by an endohedral cavity to our knowledge. Then, naturally, some questions arise as: How are modified the dipole and generalized oscillator strength by the presence of the endohedral cavity in comparison with the available free expressions? How are modified the dipole and generalized oscillator strength derived dependent properties for an atom encaged in a fullerene molecule? And what is the role of the different parameter sets reported in the literature on the dipole and generalized oscillator strength for endohedral system? Through this thesis, I address these questions (Paper II).

Another example of confinement environment for atoms or ions is under a weak plasma environment. Here, the coupling strength of the plasma with the electrons of immersed atoms has consequences in the modification of their electronic properties [4, 35], with applications in many research areas, e.g. materials processing, fusion processes, and astrophysics environments. As before, the plasma environment modifies the dipole and generalized oscillator strength derived electronic properties of relevance in material damage. For the dipole oscillator strength derived properties, the photo-ionization cross section of atoms embedded in a plasma interaction has been studied previously (see Refs. [35, 36, 37, 38] and references therein) finding that the effects of the screening potential on the photo-ionization produces multiple shape and virtual-state resonances for continuum states.

The energy loss by heavy ions colliding with a plasma, a generalized oscillator strength derived electronic property, has been investigated from the theoretical and experimental point of view in recent years [39, 40, 41]. These studies find an enhanced stopping power due to the increased energy transfer to the free plasma electrons and the charges of the projectiles inside the plasma. However, there is no work in the literature reporting generalized oscillator strength expressions for a hydrogen atom encapsulated by a fullerene molecule embedded in a plasma interaction and their dependent electronic properties. Because of this, I am interested in answering the following questions: How are modified the energy levels of the endohedral atom embedded in a plasma interaction? And how are modified the dipole and generalized oscillator strength derived dependent properties for an atom encaged in a fullerene molecule and embedded in a plasma interaction? In this work, I present some answers to these questions (Paper IV).

In the case of multielectronic systems, the photo-ionization cross section for the lithium atom has been previously studied using several theretical methods, for example the use of psuedo-potentials, Hartree-Fock methods, random phase approximations, to mentioned a few [42, 43, 44]. These methods

have rendered good results when compared to the experimental data for the free lithium atom.

In a recent paper Hasoğlu et al. [31] studied the correlation energy of the ground state of alkali-earth-metal atoms for an endohedral system A@C_{60} through multiconfiguration Hartree-Fock methods. Hasoğlu et al. did not consider the specific case of photo-ionization problem, however they found that with the increase of well depth, the valence electrons become trapped in the confining well and, as a consequence, the correlation energy increases. Then, several intrigin aspects of the multielectronic systems arise, for example, in the case of lithium atom, what is the influence of the endohedral cavity on the core electrons? How are modified the energy levels? How the DOS and GOS dependent electronic properties change? In this thesis, I give some answers to these questions (Paper V).

1.1   Outline of the thesis

Based on the previous discussion, in this thesis, I present original and novel research to explore the dipole and generalized oscillator strength derived electronic properties for atomic systems at free and at extreme conditions. The later class of systems are relevant to understand the electronic and optical response of novel materials relevant in the determination of material damage. The electronic properties under study are the photo-ionization cross section, energy mean excitation energy, and the energy deposition of heavy ions colliding with atoms and molecules (energy loss).

This thesis is presented as follows. In Chapter 2, I present the theoretical approach used to study the dipole and generalized oscillator strength derived electronic properties at free and extreme conditions for atomic systems. Thus, in the next chapters we only show results and the reader would be referred to Chapter 2 for all theoretical details. In Chapter 3, I present results of energy deposition of ions when penetrating a material considering no confinement environments (free systems). Then, in Chapter 4, I show results for the hydrogen atom under an endohedral confinement. In Chapter 5, I study the endohedral hydrogen atom embedded in a plasma interaction. In Chapter 6, the results and findings are discussed for the lithium atom encaged by an endohedral cavity. Furthermore, at the end of each chapter, we give particular conclusions and perspectives. Finally, in Chapter 7, I give the general conclusion and perspectives of this work. We use atomic units unless physical units are explicitly stated.

2

Theoretical approach

In this chapter, I provide an overview of the theoretical approach used to obtain the photo-ionization cross section, mean excitation energy, and stopping cross section (energy loss), i.e. dipole and generalized oscillator strength (DOS and GOS) derived dependent properties. For this, it is required to determine the eigenvalues and eigenfunctions of atomic systems at free and at extreme conditions, e.g. hydrogen and lithium atoms. In sections 2.1–2.3, I present a general treatment to study the DOS and GOS physical derived properties under confinement conditions, e.g. valid for any radial confinement potential. In section 2.4, it is shown the general approach to obtain the electronic spectrum for atomic systems for free and confinement conditions. Finally, I review a finite-differences numerical approach to obtain the energy spectrum and specify the numerical details used in the results.

2.1 Photo-ionization cross section

In this section, I present the theory to calculate the photo-ionization cross section (PCS) within Bethe's approach. Furthermore, I present the spherical symmetry results to obtain the PCS as a function of the dipole oscillator strength (DOS) directly from the eigenvalues and eigenfunctions through the finite-differences approach.

2.1.1 Bethe approach for the hydrogen atom

Let us consider the case of an atomic system that interacts with an electromagnetic field where one assumes that the movement of a particle of mass m is quantized and the electromagnetic field is considered as classical [45]. The Schrödinger equation for a particle with charge q and mass m_e in an electromagnetic field is described by

$$H = \frac{1}{2m_e} \left(\mathbf{p} - \frac{e}{c} \mathbf{A}(\mathbf{r}, t) \right)^2 - e\phi(\mathbf{r}, t) + V_0(\mathbf{r}), \tag{2.1}$$

where we have assumed that the vector potential $\mathbf{A}$ is given by Maxwell's equations. Here, we simplify Eq. (2.1) if we know the following relation $\mathbf{A} \cdot \mathbf{p} - \mathbf{p} \cdot \mathbf{A} = i\hbar\nabla \cdot \mathbf{A}$, where we have assumed that there is no source of electrostatic radiation, i.e. $\phi = 0$ and $\nabla \cdot \mathbf{A} = 0$ (Coulomb gauge). Thus

$$H \cong \frac{p^2}{2m_e} + \frac{e}{m_e c} (\mathbf{A} \cdot \mathbf{p}) + V_0, \tag{2.2}$$

where we have neglected the quadratic term from the expansion of Eq. (2.1). Thus, the Hamiltonian of a charged particle in the presence of an electromagnetic field in the Coloumb gauge is given as

$$\hat{H} = \hat{H}_0 + \hat{V}(t), \tag{2.3}$$

where

$$\hat{H}_0 = -\frac{\hbar^2}{2m_e}\nabla^2 + \hat{V}_0, \tag{2.4}$$

$$\hat{V}(t) = \frac{e}{m_e c}\left(\mathbf{A}\cdot\mathbf{p}\right). \tag{2.5}$$

Here, we consider $\hat{V}(t)$ as a perturbation to the Hamiltonian $\hat{H}_0$. We know in advance that this semiclassical approximation gives a good description of the influence of the external radiation field on the particle (**absorption and induced emission**), but it does not contain the description of the influence of the particles on external radiation (**spontaneous emission**).

Consider a Hamiltonian consisting of two parts, one independent of time $\hat{H}_0$ and another dependent on time $\hat{V}(t)$, as in Eq. (2.3). From perturbation theory, we obtain the transition probability, to first order, and defining the absorption coefficient in terms of the density matrix and the transition probability [45], we obtain

$$\frac{d\sigma}{d\Omega} = \frac{W_{fi}^{abs}}{Nd\Omega} = \frac{e^2}{(2\pi\hbar c)}\frac{v}{\omega}|\langle\psi_f|e^{-ik\cdot r}\epsilon\cdot p|\psi_i\rangle|^2. \tag{2.6}$$

This is the differential PCS for absorption, that describes an electron ejected from an atom under the influence of a classic electromagnetic field [34]. Here ω and k are the angular frequency, and wave vector of the incident electromagnetic radiation, respectively, v is the electron velocity, and, ψ_i and ψ_f are the wave-functions for an initial and final state. Rewriting the PCS for absorption, we obtain

$$\frac{d\sigma}{d\Omega} = -\frac{e^2}{(2\pi mc)}\frac{k_f}{\omega}|\langle\psi_f|e^{-ik\cdot r}\epsilon\cdot\nabla|\psi_i\rangle|^2, \tag{2.7}$$

where we have used $v = \hbar k/m$ and $p = -i\hbar\nabla$. From the dipole approximation, i.e. $e^{-ik\cdot r} \cong 1 + ik\cdot r + \cdots$, and assuming a linear polarization, the matrix element is modified and the PCS can be written as

$$\frac{d\sigma}{d\Omega} = \frac{8\pi^3 e^2\nu}{c}\left|\int\psi_f^* \, x \, \psi_i \, d\tau\right|^2. \tag{2.8}$$

Then, Eq. (2.8) is the PCS for absorption in terms of the frequency of the incident photon ν. The expression $|\int\psi_f^* x\psi_i d\tau|^2$ is the dipole moment between the initial and final state, which are related to the DOS. Here x is the direction of the polarization of the photon [46].

To evaluate the dipole moment that appears in Eq. (2.8) for the hydrogen atom [46], we consider that ψ_i is an eigenfunction of the ground state of the hydrogen atom, and the eigenfunction ψ_f is a continuous state. The eigenfunction of the continuum depends on the energy (or frequency ν) and on the quantum numbers l and m. The integral in Eq. (2.8) must be evaluated for all values of l and m and the results must be added. In the case of the continuous spectrum, we will use the one proposed by Bethe and Salpeter [46]. From here, we obtain an integral for the dipole moment in terms of the eigenfunctions in the continuum. Using the residue theorem to perform this integral, we obtain that the dipolar term can be written as

$$\left|\int\psi_f^* x\psi_i d\tau\right|^2 = \frac{2^8}{3Z^4}\left(\frac{n'^2}{1+n'^2}\right)^5 \frac{e^{-4n'arccotn'}}{1-e^{-2\pi n'}}, \tag{2.9}$$

where $n' = Z/k$ and Z is the atomic number. This equation is written in atomic units.

To rewrite the dipole moment [Eq. (2.9)] in terms of the frequency of the photon ν, we note that the frequency is given as $\nu_1 = E_1/\hbar$ [46]. Furthermore, the kinetic energy of the free electron W is

related to the energy of the absorbed photon $h\nu$ as $W = h\nu - I_b$. Here I_b is the ionization potential, $E = h\nu$ and $W = Z^2/n'^2$. Then, the frequency is given as

$$\nu = \nu_1(1 + 1/n'^2), \qquad n' = \left(\frac{\nu_1}{\nu - \nu_1}\right)^{1/2}. \tag{2.10}$$

Finally the PCS for the hydrogen atom is

$$\sigma(h\nu) = \sigma_H \left(\frac{E_1^3}{E^4}\right) \frac{e^{-4n' arccot n'}}{1 - e^{-2\pi n'}}, \tag{2.11}$$

where $\sigma_H = \left(2^{10}\pi^2/3\right)\left(\hbar^2/2m\right)\left(e^2/\hbar c\right) = 9364.48 \times 10^{-18} \text{eVcm}^2$ and $\sigma(h\nu)$ is a function of the photo-electron energy, E. This equation permits us to obtain the PCS for the hydrogen atom under free conditions (without confinement environment).

2.1.2 Results for spherical symmetry and pseudo-states in the continuum

Let us consider the spherical symmetry of an atomic system to obtain the PCS as a function of the DOS. In the previous section, we have seen that the PCS, Eq. (2.8), is given by

$$\sigma_{nl} = 4\pi^2 \left(\frac{e^2}{\hbar c}\right) \hbar\omega_{n_f n_i} |\langle \psi_{n_f,l_f,m_f} | \mathbf{r} \cdot \epsilon | \psi_{n_i,l_i,m_i}\rangle|^2, \tag{2.12}$$

where we have written it in terms of ω. Thus, we can rewrite the PCS as a function of the DOS as

$$\sigma_{nl} = 4\pi^2 \left(\frac{e^2\hbar}{2mc}\right) f_{n_f l_f, n_i l_i}, \tag{2.13}$$

with

$$f_{n_f l_f, n_i l_i} = \frac{2m}{\hbar} \omega_{n_f n_i} |\langle \psi_{n_f,l_f,m_f} | \mathbf{r} \cdot \epsilon | \psi_{n_i,l_i,m_i}\rangle|^2. \tag{2.14}$$

Here the $f_{n_f l_f, n_i l_i}$ depends on the polarization of the incident light and the orientation, that is, the azimuthal quantum number (m) of the initial and final state, as well as the quantum number l. The wave-functions of Eq. (2.13), for an initial and final state, are given by

$$\psi_{n_i,l_i,m_i} = \frac{u_{n_i,l_i}(r)}{r} Y_{l_i,m_i}(\theta, \phi), \tag{2.15}$$

$$\psi_{n_f,l_f,m_f} = \frac{u_{n_f,l_f}(r)}{r} Y_{l_f,m_f}(\theta, \phi). \tag{2.16}$$

When we sum over all the initial states n_i, l_i, m_i, and average over all the final states n_f, l_f, m_f [34], we obtain

$$\bar{f}_{n_f l_f, n_i l_i} = \frac{1}{2l_i + 1} \sum_{m_f=-l_f}^{+l_f} \sum_{m_i=-l_i}^{+l_i} \frac{1}{3} \sum_{i=1}^{3} f_{n_f l_f, n_i l_i}, \tag{2.17}$$

$$\bar{f}_{n_f l_f, n_i l_i} = \frac{2m}{3\hbar} \omega_{n_f n_i} \sum_{m_f=-l_f}^{l_f} \frac{1}{2l_i + 1} \underbrace{\sum_{m_i=-l_i}^{l_i} |\langle \psi_{n_f,l_f,m_f} | \mathbf{r} \cdot \epsilon | \psi_{n_i,l_i,m_i}\rangle|^2}, \tag{2.18}$$

which are known as the *mean* DOS. The underlined part will be modified (see below) to write it in terms of radial functions for the spherical symmetry.

From Eq. (2.18), the transition probability depends on the dipole matrix elements, therefore, it is convenient to write them in simpler terms using the spherical symmetry for one active electron, e.g. the hydrogen atom [47]. Thus, carrying out the matrix elements of Eq. (2.18), we obtain the Clebsch-Gordan coefficients $\langle l_f, m_f | 1, \nu, l_i, m_i \rangle$ for the coupling of the initial l_i, m_i and final angular momentum l_f, m_f. Here, for a dipole transition, the selection rule associated with the quantum number m is $\Delta m = 0, \pm 1$ and for l is $\Delta l = l_f - l_i = \pm 1$. The underlined expression, in brackets, from Eq. (2.18) is rewritten as

$$\sum_{m_i=-l_i}^{l_i} |\langle \psi_{n_f, l_f, m_f} | \mathbf{r} \cdot \epsilon | \psi_{n_i, l_i, m_i} \rangle|^2 = \left(\int_0^\infty u_{n_f l_f}(r)\, r\, u_{n_i l_i}(r)\, dr \right)^2 \frac{l_>}{2l_f + 1}, \tag{2.19}$$

where $l_>$ is the maximum of the initial and final angular momentum, $\max(l_i, l_f)$. Furthermore, taking the average over the final angular momentum

$$\sum_{m_f=-l_f}^{l_f} \frac{1}{2l_f + 1} = 1, \tag{2.20}$$

the mean DOS is given as

$$\bar{f}_{n_f l_f, n_i l_i} = \frac{2m}{3\hbar} \omega_{n_f n_i} \frac{l_>}{2l_i + 1} \left(\int_0^\infty u_{n_f l_i}(r)\, r\, u_{n_i l_i}(r)\, dr \right)^2, \tag{2.21}$$

$$= \frac{2m}{3\hbar^2} (E_{n_f} - E_{n_i}) \frac{l_>}{2l_i + 1} \left(\int_0^\infty u_{n_f l_i}(r)\, r\, u_{n_i l_i}(r)\, dr \right)^2, \tag{2.22}$$

with $\omega_{n_f n_i} = (E_{n_f} - E_{n_i})/\hbar$. When the mean DOS is positive, for $E_f > E_i$, we are in the **absorption** case. When the DOS are negative, for $E_f < E_i$, we are in the **emission** case [47]. To verify that our numerical approach has rendered a complete set of states, the DOS satisfy the Thomas-Reiche-Kuhn (TRK) sum rule [34]. The TRK sum rule is given as

$$\sum_{n_f} \bar{f}_{n_f l_f, n_i l_i}(q) + \int \frac{d\bar{f}_{n_f l_f, n_i l_i}(q)}{dE_{n_f}} dE_{n_f} = 1. \tag{2.23}$$

We observe that it considers the contributions from the bound and continuum states.

To calculate the PCS for one active electron, it is necessary to use the continuum spectrum, thus, we rewrite Eq. (2.13) as a function of the DOS [Eq. (2.14)] to obtain

$$\sigma_{nl}(h\nu) = 4\pi^2 \left(\frac{e^2 \hbar}{2mc} \right) \frac{d\bar{f}_{n0}}{dE}, \tag{2.24}$$

where we simplify the notation in the DOS as $n_i l_i \rightarrow 0$ and $n_f l_f \rightarrow n$, for an initial and final state. Here $d\bar{f}_{n0}/dE$ is the dipole oscillator strength density within the energy E and $E + dE$.

In the case when we have to describe the continuum by pseudo-continuum states, as in the case of excited solutions in a box, then we require that the continuum wave-functions of the final excited state must be normalized with respect to the energy, $u \rightarrow u_E$, i.e.

$$\int u_{E'}^*(r) u_E(r) dr = \delta(E' - E), \tag{2.25}$$

such that

$$\frac{d\bar{f}_{n0}}{dE} = \frac{2}{3} (E_n - E_0) |\langle R_{E_n}(r) | r | R_0(r) \rangle|^2, \tag{2.26}$$

with $R_E(r) = u_E(r)/r$. To normalize the final wave-function we follow the procedure of Ugray et al. [48] given as

$$R_{E_n}(r) = \sqrt{\frac{2}{E_{n+1} - E_{n-1}}} R_n(r) \,, \tag{2.27}$$

where E_{n+1} (E_{n-1}) is the energy of the adjacent above (below) pseudo-continuum excited state and $R_n(r)$ is the radial wave-function of the pseudo-continuum. Finally, Eq. (2.24) let us to calculate the PCS of an atomic system with one active electron for a dipole transition as a function of the continuum spectrum of the electronic system, Eq. (2.26), [47].

2.2 Electronic stopping power

Another property of interest related to the DOS and GOS is the electronic stopping cross section. The Bethe's model for the stopping power [8, 32] is the first quantum treatment to account for the energy deposition of ions colliding with atomic or molecular targets, which is valid in the high energy regime. Bethe considers the projectile momentum transfer as the dynamic factor that describes the energy loss within the first Born approximation.

In this model, we consider the projectile interaction with the nucleus and the electron as a perturbation to the system. Furthermore, Bethe assumes that the projectile velocity is fast enough such that the momentum does not change in the transversal direction. Under this considerations, the Hamiltonian is

$$\hat{H} = \hat{H}_1 + \hat{H}_2 + \hat{V} \,, \tag{2.28}$$

$$\hat{H} = \hat{H}_0 + \hat{V} \,, \tag{2.29}$$

where $\hat{H}_0 = \hat{H}_1 + \hat{H}_2$ and $\hat{H}_1$, and $\hat{H}_2$ are the projectile and target Hamiltonian, respectively. $\hat{H}_0$ is the unperturbed Hamiltonian, and $\hat{V}$ is the interaction potential defined now as

$$\hat{V}_p = \frac{Z_1 Z_2 e^2}{R} - Z_1 e^2 \sum_{j=1}^{N_2} \frac{1}{|\mathbf{R} - \mathbf{r}_j|} \,. \tag{2.30}$$

Here, Z_1 and Z_2 are the atomic numbers for the projectile and target, N_2 is the target bound electrons. Thus, with the Hamiltonian given by Eq. (2.28) we solve the time-dependent Schrödinger equation during the collision defined as

$$(\hat{H}_1 + \hat{H}_2 + \hat{V})\psi = i\hbar \frac{\partial \psi}{\partial t} \,. \tag{2.31}$$

Using the time-dependent perturbation theory to solve Eq. (2.31) and considering that $\hat{V}$ is a perturbation to the free system $\hat{H}_0$, the Fermi golden rule for an electronic transition from an initial (n_0) to a final (n) state is given by [8, 32]

$$W_n = \frac{2\pi}{\hbar} |\langle n|\hat{V}|n_0\rangle|^2 \delta(E_n - E_{n_0}) \,, \tag{2.32}$$

where the total energy during the collision is conserved. Integrating Eq. (2.32) as a function of the final state (n), we obtain the probability transition per time and solid angle for a momentum between p and $p + dp$ as

$$dW_{nn_0} = \frac{k M_1}{\hbar^5 (2\pi)^5} |\langle n|\hat{V}|n_0\rangle|^2 d\Omega \,, \tag{2.33}$$

where M_1 is the projectile mass. Then, the differential cross section $d\sigma_n(\theta, \phi)/d\Omega$ is given by

$$d\sigma_n(\theta, \phi) = \frac{1}{(2\pi)^2} \frac{M_1}{\hbar^4} |\langle n|\hat{V}|n_0\rangle|^2 d\Omega. \tag{2.34}$$

From the energy conservation, the energy transferred by the projectile will be the energy gained by the target. Then, the stopping cross section is given as

$$S_e = \sum_n \int (E_n - E_{n_0}) \frac{d\sigma_n}{d\Omega} d\Omega, \tag{2.35}$$

and the sum is over all target states (bound and continuum).

From the matrix element of Eq. (2.34), one finds that the electronic stopping cross section is independent of the nuclear contribution as the wave-functions only represent electronic states of the target (see Ref. [46]). The momentum transfered ($\mathbf{q}$) is related to the wave vector ($\mathbf{k}$) by $\mathbf{q} = \mathbf{k} - \mathbf{k}_0$, and from the conservation of momentum, we obtain $q^2 = k^2 + k_0^2 - 2kk_0 \cos\theta$ and $d\Omega = 2\pi q dq/kk_0$. Thus, the stopping cross section [Eq. (2.35)] is

$$S_e = \frac{8\pi Z_1 e^4}{\hbar^2 v^2} \sum_n \int_{q_{min}}^{q_{max}} (E_n - E_{n_0}) |\langle n| \sum_{j=1}^{N_2} e^{-i\mathbf{q}\cdot\mathbf{r}_j}|n_0\rangle|^2 \frac{dq}{q^2}, \tag{2.36}$$

for a given projectile velocity v. The integration over q is carried out between a minimum and maximum momentum transfer value determined from energy and momentum conservation [49]

$$q_{min}^{max}(n) = \frac{M_1 v}{\hbar} \left[1 \pm \sqrt{1 - \frac{2(E_n - E_{n_0})}{M_1 v^2}} \right]. \tag{2.37}$$

Here E_0 and E_{n_0} are the initial and final energy levels of the system, respectively.

Summarizing the previous results, we have an ion that moves with velocity v, mass M_1, with a nuclear charge Z_1 that collides with a target of mass M_2 and with N_2 electrons bound to the nucleus in some initial state $|n_0\rangle$. After the collision, the target electrons will undergo a transition to a final state, denoted by $|n\rangle$ where a transfer of kinetic energy exists between the ion and the electrons. The kinetic energy transfer from the projectile to the target is given by $E_m - E_{m_0}$. Rewriting Eq. (2.36) we obtain

$$S_e(v) = \frac{4\pi Z_1^2 e^4}{m_e v^2} \sum_n \int_{q_{min}(n)}^{q_{max}(n)} F_{nn_0}(q) \frac{dq}{q^2}, \tag{2.38}$$

where $F_{nn_0}(q)$ are the generalized oscillator strength (GOS) defined as

$$F_{nn_0}(q) = \frac{2m_e}{\hbar^2 q^2} (E_n - E_{n_0}) |M_{nn_0}(\mathbf{q})|^2, \tag{2.39}$$

and the atomic form factor given by

$$M_{nn_0}(\mathbf{q}) = \langle n| \sum_{j=1}^{N_2} e^{-i\mathbf{q}\cdot\mathbf{r}_j}|n_0\rangle. \tag{2.40}$$

The integration limits of Eq. (2.38) are given by Eq. (2.37). Then, Eq. (2.38) requires the solution of the undisturbed Schrödinger equation for a system of N_2 electrons bound to the nucleus. In other words, the knowledge of the complete excitation spectrum and the corresponding wave-functions is required.

2.2.1 Independent electron model

Instead of trying to solve an N–body problem, it is proposed to use the independent electron model (see Ref. [11, 50]) for a multi-electronic system. This model implies that a system of N_2 electrons is described by a wave-function of the Hartree type of the form $|n\rangle = |n_1, n_2, n_3, ..., n_{N_2}\rangle$, where $|n_i\rangle$ is the eigenfunction for a single electron for a undisturbed system. The energy transfer from the ground state to any excited state is written as $E_n - E_{n_0} = \sum_{j=1}^{N_2} \left(E_{n_j} - E_{n_{0j}} \right)$ which permit us to obtain the i-th contribution to the electronic stopping cross section as

$$S_e(v) = \sum_{i=1}^{N_2} S_{e,i}(v) \,, \tag{2.41}$$

where

$$S_{e,i}(v) = \frac{4\pi Z_1^2 e^4}{m_e v^2} \sum_n \int_{q_{min,i}(n)}^{q_{max,i}(n)} F_{n_i n_{0i}}^{(i)}(q) \frac{dq}{q^2} \,, \tag{2.42}$$

and the GOS for the i-th electron is given as

$$F_{n_j n_{0j}}^{(i)}(q) = \frac{2m_e}{\hbar^2 q^2} \left(E_{n_j} - E_{n_{0j}} \right) |\langle n_j|e^{-i\mathbf{q}\cdot\mathbf{r}_j}|n_{0j}\rangle|^2 \,. \tag{2.43}$$

This result reproduces the Bragg and Kleeman [51] addition rule for the electronic stopping cross section.

As a final remark, the oscillator strength is a dimensionless quantity that expresses the probability of absorption or emission of electromagnetic radiation in transitions between energy levels of an atom or molecule. Then, the GOS accounts for the probability transition from the ground state to a particular excited state for a given momentum transfer, $\mathbf{q}$, and is defined by Eq. (2.39).

The GOS, satisfy the Bethe's sum rule (BSR) [49, 34] given as

$$\sum_{n_j} F_{n_j n_0}(\mathbf{q}) + \int \frac{dF_{n_j n_0}(\mathbf{q})}{dE} dE = N_e \,, \tag{2.44}$$

where N_e is the number of bound electrons valid for any value of the transfered momentum q and is the generalization of the TRK sum rule [Eq. (2.23)]. The first term is the sum over the bound states and the second one is the sum over the continuum states. From the GOS we obtain the DOS for $q \to 0$ given as $f_{n_i n_{j0}} = \lim_{q \to 0} F_{n_j n_{j0}}(q)$, see Eq. (2.21).

2.2.2 Bethe approximation and mean excitation energy

A particular case of Eq. (2.42) is the Bethe approximation for the electronic stopping cross section for high energy regime. In the limit of high velocities ($v \gg v_e$, with v_e the target's electron velocity) Eq. (2.42) is given by kinematic considerations for binary collisions between heavy ions, such that $q_{max,i} = 2m_e v/\hbar$ and $q_{min,i} = (E_{n_i} - E_{n_{0i}})/\hbar v$. The lower limit is replaced by the independent average of the mean excitation energy, that is $q_{min,i} = I_{0i}/\hbar v$ (see Ref. [8, 46, 32]). Integrating Eq. (2.42) assuming the fulfillment of the BSR [Eq. (2.44)], with the limits defined as before, we obtain

$$S_{e,i}(v) = \frac{4\pi Z_1^2 e^4}{m_e v^2} \sum_n \int_{q_{min,i}}^{q_{max,i}} \frac{dq}{q^2} = \frac{4\pi Z_1^2 e^4}{m_e v^2} \ln \left(\frac{2m_e v^2}{I_{0i}} \right) \,. \tag{2.45}$$

Here, I_{0i} is the mean excitation energy of the i-th orbital, defined by the DOS, $f_{n_i n_{j0}} = \lim_{q \to 0} F_{n_j n_{j0}}(q)$ [Eq. (2.22)], as

$$\ln I_{0i} = \sum_{n_i} f_{n_i n_{j0}} \ln \left(E_{n_i} - E_{n_{0i}} \right) \,. \tag{2.46}$$

For high energy collisions and using the decomposition Bragg rule [Eq. (2.41)] [11, 51] which states that the mean excitation energy of an atom –molecule– is the sum of the $I_{n_{0i}}$ of all the electrons –atoms– composing the atom –molecule–. Thus, the mean excitation energy of the system is given by

$$N_2 \ln I_0 = \sum_{i=1} n_i \ln I_{n_{0i}}, \tag{2.47}$$

where n_i is the occupation number of the $i-$th orbital. This I_0 parameter accounts for the average energy that a target absorbs from the projectile kinetic energy during the collision process. The determination of I_0 is a difficult problem since it requires the knowledge of the full excitation spectrum of the target.

In summary, we know how to obtain the photo-ionization cross section [Eq. (2.24)] for atomic systems with one active electron through the mean DOS [Eq. (2.26)], the electronic stopping cross section as an orbital decomposition [Eqs. (2.41)-(2.42)] through the GOS [Eq. (2.43)], and the mean excitation energy as a function of the DOS [Eq. (2.46)]. As we observe from these physical properties, the DOS and GOS are the principal quantities to calculate as a function of the eigenvalues and eigenfunctions for a given electronic transition. Thus, in the next sections, I will show how to obtain the energy spectrum for atomic systems at free and extreme conditions.

2.3   Harmonic oscillator approach

As a first approach, the stopping cross section can be evaluated analytically, if we assume that the electrons are bound harmonically to the target. The wave-function of a three-dimensional isotropic harmonic oscillator, in Cartesian coordinates, is given as [52]

$$\phi_{n_{ix},n_{iy},n_{iz}}(x,y,z) = A_{n_i} e^{-\alpha_i^2(x^2+y^2+z^2)/2} \mathrm{H}_{n_{ix}}(\alpha_i x) \mathrm{H}_{n_{iy}}(\alpha_i y) \mathrm{H}_{n_{iz}}(\alpha_i z), \tag{2.48}$$

where $A_{n_i} = (\alpha_i^2/\pi)^{3/4}/\sqrt{2^{n_{ix}+n_{iy}+n_{iz}} n_{ix}! n_{iy}! n_{iz}!}$ is the normalization constant, $\mathrm{H}_{n_{ix}}$ is the Hermite polynomial, $\alpha_i^2 = m_e \omega_{0i}/\hbar$, and the energy of the state is given by $E_{n_i} = \hbar\omega_{0i}(n_{ix}+n_{iy}+n_{iz}+3/2)$. Here ω_{0i} is the angular frequency of the i-th electron [53]. Thus, assuming an s-initial state from Eq. (2.48) in (2.43) and (2.42) we obtain [54]

$$S_{e,i}(v) = \frac{4\pi e^4 Z_1^2}{m_e v^2} L_i(v) \,. \tag{2.49}$$

Here the stopping number is given by

$$L_i(v) = \frac{1}{2} \sum_{\nu=1}^{[E_1/I_{0i}]} \frac{\Gamma(\nu-1, x_{min}) - \Gamma(\nu-1, x_{max})}{(\nu-1)!} \,, \tag{2.50}$$

where $\Gamma(x,a)$ is the incomplete gamma function [52] and the limits are given by

$$x_{min}^{max}(v) = \frac{M_1 E_1}{m_e I_{0i}} \left(1 \pm \sqrt{1 - \frac{I_{0i}}{E_1}\nu} \right)^2 \,, \tag{2.51}$$

with I_{0i} the mean excitation energy and E_1 the projectile kinetic energy.

For atomic systems, the mean excitation energy is calculated by considering Eq. (2.48) where the ground state wave-function is a function of the angular frequency ω_{0i}. A consequence of the HO model is that $f_{0i} = \delta_{i1}$ and consequently, the orbital mean excitation energy is related to the orbital electron angular frequency as

$$I_{0i} = \hbar\omega_{0i} \,. \tag{2.52}$$

The angular frequency ω_{0i} is found through the Virial theorem given as

$$\omega_{0i} = \sqrt{\frac{-2\epsilon_{0i}}{m_e \langle r_i^2 \rangle}} \, , \tag{2.53}$$

where ϵ_{0i} and $\langle r_i^2 \rangle$ are the orbital energy and mean square position of the i-th electron, respectively, and are taken from atomic data tables [54].

In the HO model, the orbital angular frequency is the only parameter that connects naturally with the mean excitation energy. Thus, to account for the chemical composition of a molecular target, we implement the Floating Spherical Gaussian Orbital (FSGO) model (see Ref. [55] and references therein). The FSGO describes a molecular electronic system with an even number of electrons $2n$, distributed in n localized orbitals represented by the function Ψ_i, with $i = 1, 2, \cdots, n$ [56]. This model only allows to consider closed shell systems. In this representation, each Gaussian orbital describes the core $(1s^2)$, bond, and lone pair (LP) orbitals of a molecule. Each one of them is represented by a Gaussian function of the form

$$\Psi_i(\mathbf{r}) = \left(\frac{2}{\pi \rho_i^2} \right)^{3/4} e^{-(\mathbf{r} - \mathbf{R}_i)^2 / \rho_i^2} \tag{2.54}$$

where ρ_i is the orbital radius and $\mathbf{R}_i$ is the position of the Gaussian center. As noticed, this wave-function is the ground state of the HO. This similarity justify the use of the FSGO wave-function within the HO approach, such that there is a direct relations between ω_{0i} and ρ_i. Using Eq. (2.54) and Eq. (2.48) we obtain

$$I_{0i} = \frac{2\hbar^2}{m_e \rho_i^2} \, . \tag{2.55}$$

These expressions let us take into account for the mean excitation energy for atomic and molecular targets as a function of fundamental properties.

2.3.1 Spherical symmetry

In Section 2.1 we found that the electronic stopping cross section, S_e, in an orbital decomposition, is given by Eqs. (2.41)–(2.43). Here, we give a further step by taking into account the spherical symmetry of the atomic system to calculate the GOS [Eq. (2.43)] by any spherical orbital. Considering that the transfered momentum is along the z direction, the stopping cross section from an initial $1s$ state using the wave-functions of Eq. (2.15) and (2.16) is given by [57]

$$S_{e,i}(v) = \frac{4\pi Z_1^2 e^4}{m_e v^2} \sum_n \int_{q_{min,i}(n)}^{q_{max,i}(n)} F_{n_i n_{0i}}^{(i)}(q) \frac{dq}{q^2} \, , \tag{2.56}$$

where the GOS are

$$F_{n_i n_{0i}}^{(i)}(q) = \frac{2}{q^2} \left(E_{n_i} - E_{n_{0i}} \right) |M_{n_i n_{0i}}(q)|^2 \, , \tag{2.57}$$

and from the initial and final wave-functions, Eq. (2.15) and (2.16), we obtain

$$M_{n_i n_{0i}}(q) = \langle \psi_{n_f}(r, \theta, \phi) | e^{-iqr \cos \theta} | \psi_{n_i}(r, \theta, \phi) \rangle \tag{2.58}$$

$$= i^l \sqrt{2l+1} \int_0^\infty j_l(qr) u_{n_i l}^*(r) u_{10}(r) dr \, , \tag{2.59}$$

is the atomic form factor, $j_l(x)$ is the spherical Bessel function of order l, and i is the imaginary number. As we observe from Eq. (2.58), the atomic form factor is a function of the initial and final radial wave-functions, $u_{10}(r)$ and $u_{n_i l}(r)$, respectively. Note that these previous properties are only function of the time-independent spectrum of the system (free or confined at extreme conditions). These wave-functions will be found within a numerical approach by a finite-differences method.

From the above results, we observe that the photo-ionization cross section [Eq. (2.24)], mean excitation energy [Eq. (2.47)], and the electronic stopping cross section [Eq. (2.41)] are dependent on the DOS and GOS, respectively. The DOS [Eq. (2.22)] and GOS [Eq. (2.43)] are a function of the eigenvalues and eigenfunctions where the information of an atomic transition is contained. Thus, to study an atomic system at free or at extreme conditions (confinement conditions), it is necessary to obtain the energy spectrum and eigenfunctions. In the following sections, I show how to calculate the energy spectrum of the hydrogen and lithium atoms.

2.4 Electronic spectrum of atomic systems

Once I have established how to calculate the physical properties considered in this thesis, I proceed to obtain the energy spectrum of the atomic systems of interest. In this section, I show the general treatment useful to study the electronic spectrum of the atomic systems under several confinements conditions. In the next section, the confinement conditions are established used in this thesis.

2.4.1 One active electron atom

The electronic spectrum of a hydrogenic atom is given by the solutions to the time-independent Schrödinger equation [45]. However, in this case, we consider a generalized case of the problem where we suppose that the active electron is subjected to a screening potential $[V_{scre}(r)]$ (e.g. a Coulombic potential due to the inner electrons) and to a confinement potential $[V_c(r)]$. These potentials have spherical symmetry and as a consequence a dependence on the radial variable. Thus, the Schrödinger equation for an active electron is given as

$$\left[-\frac{1}{2}\nabla^2 + V_{scre}(r) + V_c(r) \right] \psi_n(\mathbf{r}) = E_n \psi_n(\mathbf{r}), \tag{2.60}$$

From the spherical symmetry of the problem the wave-function is given by Eq. (2.15). Thus, using the function replacement $R_{nl} = u_{nl}/r$, the radial Schrödinger equation is reduced to

$$\left[-\frac{1}{2}\frac{d^2}{dr^2} + \frac{l(l+1)}{2r^2} + V_{scre}(r) + V_c(r) \right] u_{nl}(r) = E_n u_{nl}, \tag{2.61}$$

which results in a one-dimension equation in terms of the radial variable as a function of the $V_{scre}(r)$ and $V_c(r)$ potentials. Eq. (2.61) let us incorporate confinement effects through $V_{scre}(r)$ and $V_c(r)$ potentials (see below), e.g. screening and pressure effects. To solve Eq. (2.61) we use a numerical method described further below.

Note that, the well-known free hydrogen atom radial equation is obtained from Eq. (2.61) when $V_{scre}(r) = -Z/r$ and $V_c = 0$.

2.4.2 Lithium atom

A further case of study is a multi-electronic systems. As a first example, I consider the ground state of the lithium atom confined under several conditions, e.g. for any confinement potential. Here I implement the Hartree-Fock (HF) method considering the Restricted and Unrestricted approaches to obtain the eigenvalues and eigenfunctions of the Li atom.

General Hartree-Fock method under confinement

In this section, I review some well-known results of the Hartree-Fock (HF) method [50] considering a general approach when the electrons of the system are subject to a confinement potential $[V_c(r)]$.

A many-body stationary system is described by the Schrödinger equation as

$$\hat{H}\Phi(q_1, ..., q_N) = E\Phi(q_1, ..., q_N), \tag{2.62}$$

where the Hamiltonian is

$$\hat{H} = \sum_{i=1}^{N}\left(-\frac{1}{2}\nabla_i^2 - \frac{Z}{r_i} + V_c(r_i)\right) + \sum_{i>j}^{N}\frac{1}{r_{ij}}. \tag{2.63}$$

Here Z is the atomic number, r_i is the distance for the i-electron to the nucleus, r_{ij} is the distance between i- and j- electrons, and $V_c(r)$ is any confinement potential. Furthermore, we are neglecting relativistic effects and we are in the Born-Oppenheimer approximation (heavy nuclei). Defining the one-electron operator $\hat{f}_i = -\frac{1}{2}\nabla_i^2 - Z/r_i + V_c(r)$ and the two-electron operator $\hat{g}_{ij} = 1/r_{ij}$, Eq. (2.63) is rewrite as

$$\hat{H} = \sum_{i=1}^{N}\hat{f}_i + \sum_{i>j}^{N}\hat{g}_{ij}. \tag{2.64}$$

Eq. (2.62) has no analytical solution thus the Hartree-Fock method is implemented. This method assumes a Slater determinant, i.e. an antisymmetric wave-function given by

$$\Phi(q_1, ..., q_N) = \frac{1}{\sqrt{n!}}\begin{vmatrix} \chi(\alpha_1; q_1) & \chi(\alpha_1; q_2) & \dots & \chi(\alpha_1; q_N) \\ \chi(\alpha_2; q_1) & \chi(\alpha_2; q_2) & \dots & \chi(\alpha_2; q_N) \\ \vdots & \vdots & \ddots & \vdots \\ \chi(\alpha_N; q_1) & \chi(\alpha_N; q_2) & \dots & \chi(\alpha_N; q_N) \end{vmatrix}, \tag{2.65}$$

where $\chi(\alpha_N; q_N) = \psi(q_N)\sigma(\alpha_N)$. Here $\psi(q_N)$ and $\sigma(\alpha_N)$ are the spatial and spin contribution, respectively. Using the variational method and Eq. (2.65) to solve Eq. (2.62), we obtain the general HF equations for an open-shell atom given by the solution of the Fock operator, $f(\mathbf{x})$, as

$$f(\mathbf{x}_1)\chi_j(\mathbf{x}_1) = \epsilon_j\chi_j(\mathbf{x}_1). \tag{2.66}$$

The spatial part in the Fockian term is given by

$$f(\mathbf{r}_1) = \hat{h}_1(\mathbf{r}_1) + \sum_{b\neq a}\hat{J}_b(\mathbf{r}_1) - \hat{K}_b(\mathbf{r}_1), \tag{2.67}$$

where $\hat{h}_1(\mathbf{r}_1)$ is the one-electron operator, $\hat{J}_b$ the Coulomb interaction operator, and $\hat{K}_b$ the exchange interaction operator defined as

$$\hat{h}_1(\mathbf{r}_1) = -\frac{1}{2}\nabla_1^2 - \sum_{A}\frac{Z_A}{r_{1A}} + V_c(r_1), \tag{2.68}$$

$$J_b(\mathbf{r}_1)\chi_j(\mathbf{r}_1) = \left(\int d\mathbf{r}_2\chi_b^*(\mathbf{r}_2)\chi_b(\mathbf{r}_2)\frac{1}{r_{12}}\right)\chi_j(\mathbf{r}_1), \tag{2.69}$$

$$K_b(\mathbf{r}_1)\chi_j(\mathbf{r}_1) = \left(\int d\mathbf{r}_2\chi_b^*(\mathbf{r}_2)\chi_j(\mathbf{r}_2)\frac{1}{r_{12}}\right)\chi_b(\mathbf{r}_1). \tag{2.70}$$

Recalling that the single electron term, Eq. (2.68), includes the confinement potential $V_c(r)$[1]. This, let us to account for the effects of the confinement potential on the electron in each orbital.

The ground state HF energy is defined as

$$E_0 = \sum_j h_{jj} + \frac{1}{2} \sum_{i \neq j} J_{ij} - K_{ij}, \tag{2.71}$$

with

$$h_{jj} = \int d\mathbf{r} \chi_j(\mathbf{r}) \hat{h}(\mathbf{r}) \chi_j(\mathbf{r}), \tag{2.72}$$

$$J_{ij} = \int d\mathbf{r}_1 d\mathbf{r}_2 \chi_i(\mathbf{r}_1) \chi_i(\mathbf{r}_1) \frac{1}{r_{12}} \chi_j(\mathbf{r}_2) \chi_j(\mathbf{r}_2), \tag{2.73}$$

$$K_{ij} = \int d\mathbf{r}_1 d\mathbf{r}_2 \chi_i(\mathbf{r}_1) \chi_j(\mathbf{r}_1) \frac{1}{r_{12}} \chi_j(\mathbf{r}_2) \chi_i(\mathbf{r}_2). \tag{2.74}$$

It is important to note that Eqs. (2.66) are coupled and include the confinement by any model potential.

Unrestricted Hartree-Fock approach

The unrestricted Hartree-Fock theory is the molecular orbital method for open shell atoms/molecules where the number of electrons of each spin are different. This appraoch use single determinant total wave function in which orbitals of the same n, l, and m_l values but different m_s values are regarded as being independent [50].

Equations and ground state energy

Let us consider the lithium atom in the ground state $1s^2 2s^1$ in an arbitrary confinement potential. Thus, in agreement with Fig. 2.1a) and Eq. (2.67), the Unrestricted Hartree-Fock (UHF) equations are given as

$$\left(\hat{h}_1 + \hat{J}_2 + \hat{J}_3 - \hat{K}_3 \right) \chi_1(\mathbf{r}_1) = \epsilon_1 \chi_1(\mathbf{r}_1), \tag{2.75}$$

$$\left(\hat{h}_2 + \hat{J}_1 + \hat{J}_3 \right) \chi_2(\mathbf{r}_1) = \epsilon_2 \chi_2(\mathbf{r}_1), \tag{2.76}$$

$$\left(\hat{h}_3 + \hat{J}_1 + \hat{J}_2 - \hat{K}_1 \right) \chi_3(\mathbf{r}_1) = \epsilon_3 \chi_3(\mathbf{r}_1), \tag{2.77}$$

with $\chi_i(\mathbf{r}_i) = \psi(\mathbf{r}_1) \sigma(\omega)$, $\sigma(\omega) = \alpha(\omega)$ or $\beta(\omega)$ is the spin contribution. The subscripts $1, 2$ in the wave-function χ and energy terms corresponds to an electron in the ground state $1s^2$, and the subscript 3 corresponds to valence electron, i.e. $\chi_1 = \chi_{1s}^{\alpha}$, $\chi_2 = \chi_{1s}^{\beta}$, and χ_3 the electron that is excited. The $\hat{h}_i$, $\hat{J}_i$, and K_i were given explicitly by Eq. (2.68)–(2.70).

The ground state energy, from Eq. (2.71), is given as

$$E_0^{UHF} = \sum_{j=1}^{3} h_{jj} + \frac{1}{2} \sum_{i=1, i \neq j}^{3} \sum_{j=1}^{3} J_{ij} - K_{ij}, \tag{2.78}$$

$$= h_{11} + h_{22} + h_{33} + J_{21} + J_{31} + J_{32} - K_{13}, \tag{2.79}$$

according to the configuration shown in Fig. 2.1a) for the UHF case.

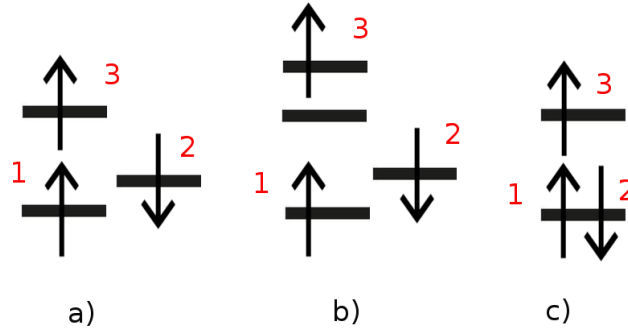[1]The free atom is obtained when $V_c = 0$.

Figure 2.1: Configurations for the lithium atom. a) Unrestricted HF for ground state. b) Unrestricted HF for an excited state. c) Restricted HF for the ground state.

Gauss-Seidel iteration method

To solve the coupled UHF equations (2.75)–(2.77), we use the Gauss-Seidel iteration method [58]. Here, we obtain the lithium ground state energies and wave-functions that are used to first step to obtain the electronic spectrum of the lithium atom under confinement conditions (see next section). Under this approach, we need to guess an initial wave function (χ_i) that allows us to calculate the Coulomb and exchange integrals involved in Eqs. (2.75)–(2.77) as a first step. Then, we solve at the same time the system of couples equations with this initial guess and we obtain new wave-functions for the ground state, $\bar{u}_i$. With this new wave-functions, we construct an improved wave function (u^{imp}) for each electron given as

$$u_i^{imp}(r) = (1 - \omega)u_i(r) + \omega\bar{u}_i(r),$$

(2.80)

where ω is a relaxation parameter that has the value of 3/4. Then, we calculate the total energy given by Eq. (2.79) and repeat this process until the total energy does not change, i.e. under a self-consistent convergence criterion. At the end, we obtain, for each electron in the ground state of lithium atom, an energy and a wave-function that includes the confinement interaction. In Appendix B, we describe the implementation of the GS into the UHF approach.

Valence electron equation

Once we obtain the radial ground state wave-functions u_1, u_2, and u_3 subjected to the V_c confinement through the Gauss-Seidel method, we obtain the energy spectrum of the lithium atom through Eq. (2.77). Now we need to obtain the bound and continuum (psuedo-continuum) states to calculate the DOS derived properties of the Li atom. As, from Eq. (2.77) the spatial part is

$$\left(\hat{h}_3 + \hat{J}_1 + \hat{J}_2 - \hat{K}_1\right)\psi_3(\mathbf{r}) = \epsilon_3\psi_3(\mathbf{r}),$$

the elements $\hat{J}_1$, $\hat{J}_2$ can be calculated using the previous results, i.e. the wave-functions found by the GS method for the ground state. However, the exchange term $\hat{K}_1$ needs a more special treatment. To include the exchange interaction of the inner core with the valence electron, we use Slater's X-α [59] approximation as a first approach. Thus the exchange interaction is approximated as

$$\hat{K}_1 = \alpha\rho_1^{1/3}(\vec{r}),$$

(2.81)

where α is a parameter. Here the term $\rho_1(\vec{r})$ is the cahrge density due to the $1s^2$ electrons, $\rho_1(\mathbf{r}_1) = \sum_i |\psi_i(\mathbf{r})|^2$, and it is defined in terms of ground state wave-functions.

Under this approach the exchange term is given by

$$\hat{K}_1\psi_3(\mathbf{r}_1) = \alpha\rho_1^{1/3}(\mathbf{r}_1)\psi_3(\mathbf{r}_1). \tag{2.82}$$

The valence electron equation (2.77) is rewritten as

$$\left(\hat{h}_3 + \hat{J}_1 + \hat{J}_2 - \alpha\rho_1^{1/3}\right)\psi_3(\mathbf{r}_1) = \epsilon_3\psi_3(\mathbf{r}_1), \tag{2.83}$$

using the spherical symmetry and making $\psi(\mathbf{r}) = (u_{nl}(r)/r)Y_{ml}(\theta,\phi)$ we obtain

$$\left(-\frac{1}{2}\frac{d^2}{dr_1^2} + \frac{l(l+1)}{2r_1^2} - \frac{Z}{r_1} + V_c(r_1) + \hat{J}_1 + \hat{J}_2 - \alpha\rho_1^{1/3}\right)u_3(r_1) = \epsilon_3 u_3(r_1). \tag{2.84}$$

A one-electron equation that allows us to solve it with a numerical approach, e.g. a finite-differences approach and obtain the excitation spectrum of the lithium atom.

Generalized and dipole oscillator strengths

In this Section, we present the theoretical approach for the GOS and DOS for the UHF case that is closely related to the theory approach reviewed in Section 2.2.

From Eq. (2.39), in atomic units, the GOS for a multi-electronic system in the UHF case is defined as [50]

$$F_{n0} = \frac{2}{q^2}\left(E_n^{UHF} - E_0^{UHF}\right)|\langle\Psi_n(\mathbf{r})|\sum_{j=1}^{N}e^{i\mathbf{q}\cdot\mathbf{r}_j}|\Psi_0(\mathbf{r})\rangle|^2, \tag{2.85}$$

where $\mathbf{q}$ is the momentum transferred, Ψ_n is the final excited state, and Ψ_0 is the initial state from where the transition occurs, and N is the number of electrons in a multi-electronic system. In the special case when $q \to 0$ in Eq. (2.85), the GOS corresponds to the DOS given by

$$f_{n0} = 2\left(E_n^{UHF} - E_0^{UHF}\right)|\langle\Psi_n(\mathbf{r})|\sum_{j=1}^{N}\mathbf{r}_j|\Psi_0(\mathbf{r})\rangle|^2. \tag{2.86}$$

From Zsabo and Ostlund [50], a one-electron operator defined as $O_1 = \sum_{j=1}^{N}h(j)$, where $h(j)$ is any operator involving only the $i-$th electron, is used to rewrite the atomic form factor for a determinant that differs by an orbital, in Eq. (2.86), as

$$\langle\Psi_n(\mathbf{r})|O_1|\Psi_0(\mathbf{r})\rangle = \langle\chi_n(\mathbf{r})|h|\chi_0(\mathbf{r})\rangle. \tag{2.87}$$

In our particular case we obtain

$$\langle\Psi_n(\mathbf{r})|\sum_{j=1}^{N}\mathbf{r}_j|\Psi_0(\mathbf{r})\rangle = \langle\chi_n(\mathbf{r})|r|\chi_0(\mathbf{r})\rangle. \tag{2.88}$$

Thus, for a multi-electronic system, the atomic form factor is rewritten in terms of the wavefunctions of the ground and excited states, χ_0 and χ_n, respectively. From Eq. (2.88), the DOS [Eq. (2.86)] is given as

$$f_{n0} = 2\left(E_n^{UHF} - E_0^{UHF}\right)|\langle\chi_n(\mathbf{r})|r|\chi_0(\mathbf{r})\rangle|^2. \tag{2.89}$$

Thus, the mean DOS under spherical symmetry is rewritten as

$$\bar{f}_{n0} = \frac{2}{3} \left(E_n^{UHF} - E_0^{UHF}\right) \frac{l_>}{2l_i + 1} |\langle u_n(r)|r|u_0(r)\rangle|^2, \tag{2.90}$$

where $u_0(r)$ and $u_n(r)$ are the initial and final radial wave-functions of the valence electron, respectively. This result is similar to Eq. (2.22) with the only difference in the energy levels, i.e. E_0^{UHF} and E_n^{UHF} is the total energy for the ground and excited state, respectively. A note of caution must be taken with this result. The 1 and 2 electrons are still frozen, so it is not really an UHF approach. When the 3rd electron is excited, the inner electrons will relax and change wave-function and energy. What we have is that 1 and 2 electron are not the same as in strictly unrestricted or restricted Hartree-Fock (see below). This is due to the X-α approximation.

Restricted Hartree-Fock approach

Equations and ground state energy

In the restricted Hartree-Fock (RHF) approach, we suppose that the two electrons in the $1s^2$ core are frozen, i.e. there is no interaction with the valence electron in $2s^1$ (or any excited state), see Fig. 2.1c). Thus, from Eqs. (2.75)-(2.77), the terms $\hat{J}_3$ and $\hat{K}_3$ are null and we obtain

$$\left(\hat{h}_1 + \hat{J}_2\right) \chi_1(\mathbf{r}_1) = \epsilon_1 \chi_1(\mathbf{r}_1), \tag{2.91}$$

$$\left(\hat{h}_3 + 2\hat{J}_1 - \hat{K}_1\right) \chi_3(\mathbf{r}_1) = \epsilon_3 \chi_3(\mathbf{r}_1), \tag{2.92}$$

where Eq. (2.91) is the same for the paired electrons 1 and 2 in the frozen core $1s^2$. The ground state energy is defined as

$$E_0^{RHF} = 2h_{11} + h_{33} + J_{12} + 2J_{31} - K_{13}, \tag{2.93}$$

according with the configuration shown in Fig. 2.1c) for the RHF case.

In this case, $E_n^{RHF} - E_0^{RHF} = \epsilon_3 - \epsilon_1$ and the system is reduced to solve Eq. (2.91) and (2.92) using the Gauss-Seidel interaction method discussed above.

Generalized and dipole oscillator strengths

Once the eigenvalues and eigenfunctions are obtained for the ground and excited states, we would determine the GOS and DOS for the RHF approach. The GOS for the RHF case is similar to Eq. (2.85) and is given as

$$F_{n0} = \frac{2}{q^2} \left(\epsilon_n - \epsilon_0\right) |\langle \chi_n(\mathbf{r})|e^{i\mathbf{q}\cdot\mathbf{r}}|\chi_0(\mathbf{r})\rangle|^2, \tag{2.94}$$

where $\mathbf{q}$ is the momentum transfer, χ_n is the final excited orbital, and χ_0 is the initial orbital from where the transition occurs. Observe that this is a result for a one-electron system. For $q \to 0$ in Eq. (2.94), the GOS reduced to the DOS. In the case of spherical symmetry, the mean DOS for one active electron atom is reduced to

$$\bar{f}_{n0} = \frac{2}{3} \left(\epsilon_n - \epsilon_0\right) \frac{l_>}{2l_i + 1} |\langle u_n(r)|r|u_0(r)\rangle|^2, \tag{2.95}$$

where $l_>$, $u_0(r)$, and $u_n(r)$ are defined as above, ϵ_0 and ϵ_n are the orbital energy for the ground and excited states, respectively, of the valences electron.

In this section, I have shown the equations that allows us to obtain the energy spectrum of the hydrogen [Eq. (2.60)] and lithium [Eq. (2.83) and (2.91)] atoms as a function of a screening, $V_{scre}(r)$,

and a confinement, $V_c(r)$, potentials. As I mentioned above, the purpose of these potentials is to generalize the eigenvalue problem, for the hydrogen and lithium atoms, and incorporate the extreme conditions to obtain the energy spectrum dependence on the confinement environments. In next sections, I establish which are the extreme conditions considered in this thesis.

2.5   Extreme conditions

In this section, we show the extreme environments consider in this thesis given by the confinement potentials $V_{scre}(r)$ and $V_c(r)$. The first extreme condition is when the atomic system is subject to an endohedral confinement. The second is when the atomic system is subjected to a plasma interaction.

2.5.1   Endohedral confinement by a fullerene cavity

To describe the electronic properties of an atom inside a fullerene cavity, we need to consider the n-carbon atoms that constitute the fullerene and their delocalized valence electrons. This is an expensive and complicated task from a purely *ab initio* approach. Thus, model potentials of quantum confinement have proven to be appropriate (see e.g. Refs. [29, 30, 15, 16, 60]). Several potentials have been proposed that model the spectral properties of a fullerene cage [22, 23, 24, 61]. For example, the Dirac δ-potential [62], the square-well potential [63], the Woods-Saxon (WS) potential [64, 25], and the power exponential potential [65, 26] have been used to model a C_n cavity. In a previous work, Dolmatov et al. [25] found that the discontinuity shown by the squared well potential is not relevant to the determination of dipole properties of the enclosed endohedral atom, particularly for the study of the photo-ionization cross section. In this thesis, we use the square-well and the Woods-Saxon potentials to model the endohedral cavity in order to address these findings. However, the question is left open for properties that depend on the GOS for the H@C_{60} system. In Paper II, we respond this question finding that the discontinuity is relevant in the determination of the GOS derived properties in comparison with the DOS derived properties.

The parameters used in this work to describe a C_n fullerene cage are used under the assumption that the fullerene cage electronic configuration is static. This assumption means that only the active electron in the H@C_{60} endohedral system is the one in the H atom. Evidently, a more realistic cavity description is required if one is to study the plasmonic behavior of the C_{60} system [66, 67], or to take into account the exchange repulsion and polarization of the electronic structure [68], but that is outside the scope of this thesis. Thus, we can consider, as a first order approximation to a more realistic approach, a model potential to describe the electronic structure of the endohedral cage. The square-well model potential is defined as

$$V_c(r) = \left\{ \begin{array}{ll} -V_0, & R_0 \leq r \leq R_0 + \Delta \\ 0, & \text{otherwise} \end{array} \right. , \tag{2.96}$$

where R_0 is the inner radius, Δ is the thickness of the spherical shell and V_0 is the potential well depth. The Woods-Saxon model potential [64] is defined as

$$V_c(r) = \frac{V_0}{1 + e^{-(r-(R_0+\Delta))/\gamma}} - \frac{V_0}{1 + e^{-(r-R_0)/\gamma}}, \tag{2.97}$$

where γ is a smoothing parameter and R_0, Δ, and V_0 are defined as before. In particular, we use two sets of parameters (inner radius, thickness of the spherical shell and well depth) found in the literature to characterize an endohedral cavity [69, 63, 31]. In Fig. 2.2 we show the square (solid line) and Woods-Saxon (dashed symbol lines) model potential observing the discontinuity at $r = R_0$ and $r = R_0 + \Delta$ for the square-well potential in comparison with the Woods-Saxon potential.

Finally, to obtain the eigenvalues and eigenfunctions of the endohedral hydrogen systems, we use Eq. (2.96) or (2.97) in Eq. (2.61), (2.84) and (2.92), respectively, with $V_{scre}(r) = -Z/r$.
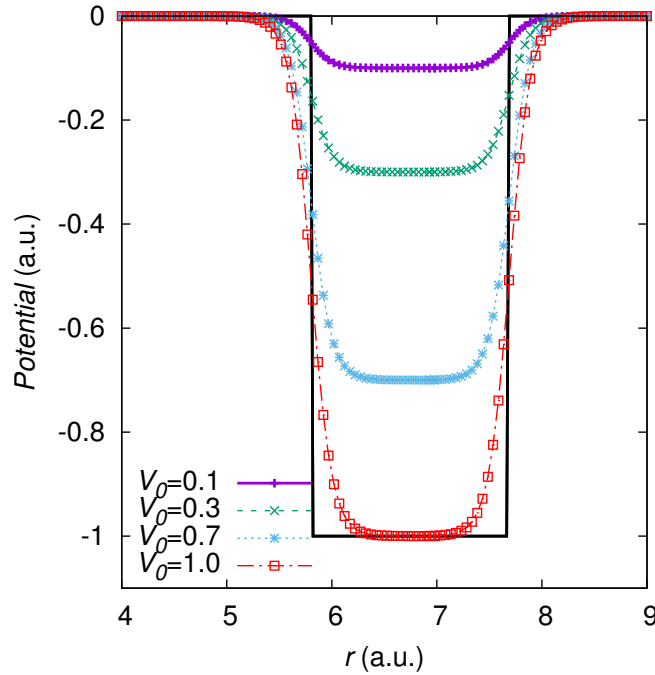
Figure 2.2: Square well (solid-line) and Woods-Saxon (dashed lines with symbols) model potential as a function of the potential well depth V_0 for the parameters $R_0 = 5.8$ a.u., $\Delta = 1.89$ a.u., and $\gamma = 0.1$. See text for details.

2.5.2 Plasma interaction

The study of atoms or ions under plasma environments has been a topic of great interest over the past decades due to the coupling strength of the plasma with the electrons of immersed atoms and the consequent modification of their electronic properties [4, 35, 3], with applications in many research areas, e.g., fusion processes [70], materials processing [71], and astrophysics environments [72]. The plasma interaction may be described by a screening potential function that incorporates the collective effects of the correlated many particles interaction processes in a plasma and has been studied exhaustively under different treatments [73, 74], e.g., by the Debye-Hückel potential [74, 75], the cosine Debye-Hückel potential [36], and recently by the Coulomb potential for finite-temperature [76, 77]. Then, to describe the influence of a weak plasma interaction on an free atomic or on a H@C$_{60}$ system, we use the Debye-Hückel screening potential that characterizes the plasma in terms of a Debye screening parameter λ_D. The Debye plasma screening potential $V_{scre}(r)$ is [73, 74]

$$V_{scre}(r) = -\frac{Z}{r}\exp(-r/\lambda_D)\,, \tag{2.98}$$

with the Debye screening length given by $\lambda_D = \left[4\pi(1+Z^*)ne^2/k_BT\right]^{-1/2}$, k_B is the Boltzmann constant, n the density of plasma electrons, T the temperature, Z^* the effective charge of the ions in the embedded plasma, and Z the hydrogenic nuclei charge. The Debye-Hückel model is valid for weak plasmas, i.e. those where $\Gamma = (Ze)^2(4\pi n/3)^{1/3}/k_BT < 1$ is fulfilled [3, 74].

In order to relate the order of magnitude of the plasma density, as a function of the Debye screening length λ_D, in Fig. 2.3, we show the electron plasma density for several temperatures as a function of λ_D in a.u.. Examples of weakly coupled plasmas (thick blue-lines) are those occurring in fusion plasma ($T \sim 6 \times 10^6 - 10^7$ K, $n \sim 10^{22} - 10^{26}$ cm^{-3}), laser-produced plasma ($T \sim 5 \times 10^5 - 3 \times 10^6$ K, $n \sim 10^{19} - 10^{21}$ cm^{-3}), and stellar atmospheres ($T \sim 6 \times 10^3 - 6 \times 10^4$ K, $n \sim 10^{15} - 10^{18}$ cm^{-3}) [3, 38, 78]. As shown in the figure, the yellow shaded region is where the weak plasma condition of
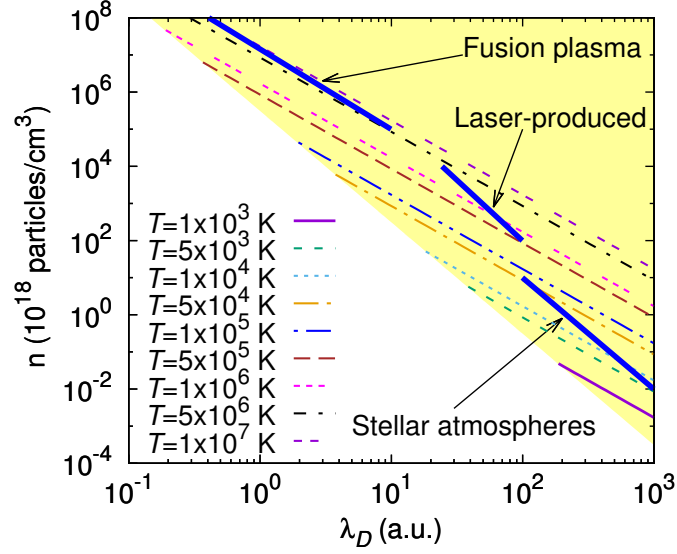
Figure 2.3: The density of plasma electrons, n (cm^{-3}), as a function of the screening length, λ_D (a.u.), for several plasma temperatures T (K). The thick lines are example regions for fusion plasma, laser-produced plasma, and stellar atmospheres where our model is applicable (yellow shaded area). See text for details.

our model is fulfilled.

Thus, the effect of a confinement environment is accounted for by Eqs. (2.96), (2.97) or (2.98), that permit us to find the DOS and GOS derived electronic properties. Then, to consider the hydrogen atom encaged by an endohedral cavity embedded in a plasma interaction we use Eq. (2.98) and (2.97) [or Eq. (2.96)] in (2.61).

2.6   Free atomic systems

The electronic spectrum of a free (without extreme conditions) atomic systems, i.e. no confinement, has been a well-known problem since many years ago. For example, for the hydrogen atom, there is an analytical solution to the time-independent Schrödinger equation to obtain the energy spectrum and the wave-functions, and as a consequence physical properties as photo-ionization, mean excitation energy, and energy deposition (energy loss) have been reported. In the case of multi-electronic systems, several approaches have been proposed to obtain the energy spectrum, e.g. Hartree-Fock methods, density functional theory, local plasma approximations among others. In this thesis, we are interested in obtaining the energy spectrum and wave-functions for free atomic systems to calculate the stopping cross section for heavy ions colliding with several atomic and molecular targets through the equations presented in Section 2.2. These results are presented in Chapter 3.

Furthermore, from Section 2.4, I recover the well-known results for free atomic systems For example, the radial hydrigenic equation, Eq. (2.61), for a free system is obtained for $V_{scre}(r) = -Z/r$ and $V_c = 0$. The general Hartree-Fock equations, Eq. (2.63), for a free system are recovered when $V_c = 0$.

Finally in this chapter, I have shown the theoretical approach to study atomic systems at free and at extreme conditions. This approach, permit us to account for the effects on the energy spectrum of the hydrogen and lithium atoms and, as a consequence, the change on DOS and GOS derived electronic properties.

In the following chapters I will show how the DOS and GOS dependent properties are modified for free atomic systems and at extreme conditions.

2.7 Finite-differences approach

Finally we are in position to find the energy spectrum and wave-functions of: the H@C$_{60}$ system [Eq. (2.61)], the H@C$_{60}$ system embedded in a weak plasma interaction, and for the Li@C$_{60}$ system in the UHF and RHF [Eq. (2.84) and (2.92) respectively] for different values of the confinement potential V_0. For this, we implement a finite-differences numerical approach. The basic idea of a finite-differences approach is to discretize the function $u(r) \to u_k$ where $r \to r_k$ is known at the k-th point on a numerical grid. Thus, $k = 0$ represents u_0 and $k = N + 1$ represents u_{N+1}, which are the boundary conditions of the system, respectively [79]. The wave function u_k is solved for N points in the grid. In Appendix A, I give a detailed derivation of a finite-differences approach that is useful for all radial equations considered in this thesis, e.g. Eqs. (2.61), (2.84), and (2.92). In short, by using the definition of derivative and integration in a discretized grid, we can write Eq. (2.61) in matrix form taking into account the boundary conditions. We use a finite-differences approach centered at the midpoint. Thus, Eq. (2.61) is rewritten as

$$\mathbf{\tilde{H}}\vec{\phi} = E\vec{\phi}. \tag{2.99}$$

where the matrix elements are give by

$$\tilde{H}_{i,i} = \frac{1}{2}\left[\frac{1}{r_i - r_{i-1}} + \frac{1}{r_{i+1} - r_i}\right]\frac{1}{r_{i+1/2} - r_{i-1/2}} + V_i, \tag{2.100}$$

$$\tilde{H}_{i,i+1} = -\frac{1}{2(r_{i+1} - r_i)}\frac{1}{\sqrt{(r_{i+1/2} - r_{i-1/2})(r_{i+3/2} - r_{i+1/2})}}, \tag{2.101}$$

$$\tilde{H}_{i,i-1} = -\frac{1}{2(r_i - r_{i-1})}\frac{1}{\sqrt{(r_{i+1/2} - r_{i-1/2})(r_{i-1/2} - r_{i-3/2})}}. \tag{2.102}$$

The latter equations permit us to solve the eigenvalue problem as a linear algebra problem.

2.8 Numerical implementation details

The results that are presented in the following chapters have been obtained considering a numerical grid box that extends from $r = 0$ to $r = 500$ a.u., with a total number of $N = 2000$ points spaced logarithmically in this range. The logarithmic grid allow us to have a better description of the wave-function cusp at the origin and around the endohedral cage to guarantee the fulfillment of the numerical procedure. We have calculated the GOS for values of the momentum transfer q up to 30 a.u., in steps of $\Delta q = 0.1$ a.u., and we have found that a value of l up to $l_{max} = 100$ fulfills the Bethe sum rule. This means that we have a total of 200 000 excited states to describe the electronic properties of the endohedral cavity for each well depth. For the DOS, we have a total of $2,000$ excited states for $l = 1$ to describe the electronic properties of the endohedral cavity for each well depth. The accuracy of our finite-differences approach is controlled by the number of points in the grid and their spacing. We have found that $N = 2000$ points spaced logarithmically between $r = 0$ and $r = 500$ a.u., produces eigenvalues with a precision, for the free atomic systems considered in this thesis, up to the 4th decimal place. Increasing the number of points would increase the precision, but at a higher computational cost. Thus, these set of grid parameters are a compromise between precision and computing cost.

For the endohedral cage, two sets of parameters have been proposed to characterize properly the cavity: a) $R_0 = 5.8$ a.u., $\Delta = 1.89$ a.u., and $V_0 = 0.302$ a.u. [80, 31] and b) $R_0 = 6.01$ a.u., $\Delta = 1.25$ a.u., and $V_0 = 0.422$ a.u. [25]. For the system H@C$_{60}$, we use both sets of parameters to describe the DOS and GOS electronic properties. We report the DOS and GOS derived electronic properties of interest as a function of V_0 for values going from the free case ($V_0 = 0$) to $V_0 = 2.0$ a.u., in steps of 0.1 a.u., to represent different electronic configurations of an endohedral H and Li atom.

For the H@C$_{60}$ system and subjected to a weak plasma interaction, we describe the endohedral cage by $R_0 = 5.8$ a.u., $\Delta = 1.89$ a.u., $V_0 = 0.302$ a.u., and $\gamma = 0.1$ [81]. Furthermore, we report

the electronic properties of interest for other selected well depths values of $V_0 = 0$, 0.7, and 1.0 a.u., that represent different electronic configurations of a C_{60} endohedral cage. The choice of these values corresponds to no cavity ($V_0 = 0$), $V_0 = 0.7$ corresponds to the cavity depth for the first avoiding crossing between the $2s$ and the $1s$ state [30], and $V_0 = 1.0$ is when the $2s$ hydrogen state emulates the $1s$ state [30]. For each potential well depth, we present our results as a function of selected screening length λ_D values ranging from $\lambda_D = 0.01$ to $\lambda_D = 100,000$ a.u.. This last value is used to emulate no plasma influence on the C_{60} cavity, i.e. $\lambda_D \to \infty$. Thus, our values represent different plasma environments and confinement conditions.

The method has been implemented in a *FORTRAN 95* code that calculates the eigenvalues, eigenfunctions, and physical properties.

In this chapter, I presented the theoretical approach use to obtain the results show in this thesis for free and confined atomic and molecular systems. Thus, in the next chapters, we only show results for free and confined systems and the reader would be referred to this chapter for the theoretical details and numerical implementation in each case.

3

Energy deposition for free atomic and molecular systems

As a first step towards the understanding of energy deposition of heavy ions when penetrating a material, in this chapter I present results for atomic and molecular systems considering no confinement environments (free systems). This chapter is based on the research **Paper I** and **III**.

The energy deposition of heavy ions is of crucial importance in determining the damage to materials with implications in areas such as material science, plasma physics, radiotherapy, and dosimetry [55]. In the fisrt part of the chapter, I show that there is an universal scaling when the electronic stopping cross sections and projectile kinetic energy are scaled properly in terms of the target mean excitation energy, I_0, for all projectile-target combinations considered within Bethe's tehory. The scaling law expresses a systematic and universal behavior among complex projectile-target systems in the energy deposition, characterized by the minimum momentum transfer during the slowing down process. I provide an analytic expression for the universal scaling law for the stopping cross section of any projectile-target combination valid at high collision energies. We compare our universal scaling with atomic and molecular experimental data available in the literature observing a good agreement.

In the second part of this chapter, I study the effects of the initial s- and p-orbital target symmetry on the generalized oscillator strength (GOS) and its consequences on the stopping cross-section. This study is within Bethe's theory of energy deposition by implementing the harmonic oscillator (HO) approach to describe the target's electron interactions. We report explicit expressions for the GOS as a function of the initial target's symmetry for angular momentum $l = 0$ and 1, making evident the role of the targets symmetry contribution to the electronic stopping cross-section. The parameter that characterizes the absorption of energy from the projectile to the target is the mean excitation energy, I_0. Here, I use the I_0 reported by Oddershede and Sabin [At. Data Nucl. Data Tables (1984), **31**, 275] in an orbital decomposition. We show results for the electronic stopping cross-section for protons colliding with He, Li, B, C, Ne, and Ar atomic gases. Here I include the behavior of s- and p-orbital target symmetry, showing excellent agreement with the available experimental data. Thus, I explore the role that the symmetries of the initial state plays to account for the GOS and as a consequence the electronic stopping cross section.

3.1 Heavy ions colliding with several targets

This section is based on the research **Paper I** contribution as a Ph.D. student.

3.1.1 Energy deposition and mean excitation energy

As we have mentioned previously, the energy deposition of swift, heavy particles when penetrating matter is described solely by the target mean excitation energy, I_0, at intermediate to high collision energies. This mean excitation energy characterizes how the target absorbs energy from the incoming projectile through the dipole oscillator strength, f_{0n} (DOS). Thus, if I_0 characterizes the way that a target absorbs energy when colliding with an atom or molecule, it ponders the question if there is an

universal behavior or scaling of the electronic stopping cross section based on this target property. The idea of determining a scaling law is to express a systematic and universal behavior among complex projectile-target systems in the energy deposition, regardless of the detailed mechanism for slowing down. The mean excitation energy is accounted for by Eqs. (2.52) and (2.55) for atomic and molecular targets, respectively.

Let us note that Eq. (2.49) assumes a fixed projectile charge. However, experimental evidence points to the fact that the projectile has an "effective charge", Z_p^*, dependent on the projectile velocity. Here, we use Betz expression for the effective charge, namely $Z_p^* = Z_p \left(1 - e^{-v/v_0 Z_p^{2/3}}\right)$ [82] where v and v_0 are the projectile and Bohr velocities, respectively.

3.1.2 Results

The scaling law for the electronic stopping cross section can be obtained by making $\epsilon = m_e E_p / M_p I_{0i}$ in Eqs. (2.49)–(2.51). By doing so, we obtain a general, single –universal– curve within the first Born approximation that only depends on the target properties as

$$\frac{I_{0i}}{4\pi e^4 Z_p^{*2}} S_{e,i}(\epsilon) = f(\epsilon) , \qquad (3.1)$$

where

$$f(\epsilon) = 2\frac{L_i(\epsilon)}{\epsilon} , \qquad (3.2)$$

and $L_i(\epsilon)$ is given by Eq. (2.50). The left-hand side of Eq. (3.1) depends only on the projectile-target properties and the right-hand side is the universal curve, $f(\epsilon)$ as a function of the scaled projectile energy. Thus, $f(\epsilon)$ is a scaled electronic stopping number given in terms of the target excitation spectrum.

Once we obtain a single –universal– curve, Eq. (3.1), to account for the electronic stopping cross section as a function of target properties, we are ready to test it on atomic and molecular targets.

The use of Eq. (2.50), and consequently Eq. (3.1), is umpractical due to the large sum that involves the evaluation of the incomplete Gamma function. We have adjusted the $f(\epsilon)$ curve to an expression given as

$$f(\epsilon) = \frac{\ln\left(1 + 16\epsilon^2\right)}{c + \epsilon} , \qquad (3.3)$$

where $c = 2/\pi$ given an error of less than 2% respect to the numerical evaluation of Eq. (2.50) for $\epsilon > 1$ which is the region of validity of the first Born approximation.

Atomic targets

In Fig. 3.1a), I show the scaled S_e curve for H, He, Li, Be, C, N, O, Ne, Al, Si, Ar, Ca, Kr, Xe, Au, Pb, and Bi heavy ion projectiles colliding with He, Be, B, C, Ne, Al, Si, and Ar atomic targets given by Eq. (3.1) using the mean excitation energy reported for the atomic case by Eq. (2.52) [11]. The symbols are the experimental data as given in Refs. [83, 84, 85, 86, 87, 88, 89, 90, 91, 92, 93, 94, 95, 96, 97, 98, 99, 100, 101, 102, 103]. From the figure, one observes an excellent agreement for high energy collisions ($\epsilon > 10$) values in comparison with the available experimental data.

Molecular targets

In Fig. 3.1, we show the scaled stopping cross section [Eq. (3.1)] for H, He, Li, C, O, Ne, Si, Ar, and Kr heavy ion projectiles colliding with H_2 , CH_4 , H_2O, CO_2 , Mylar, and Kapton molecular targets in comparison with the available experimental data. As we observe, for high energies, the scaling law
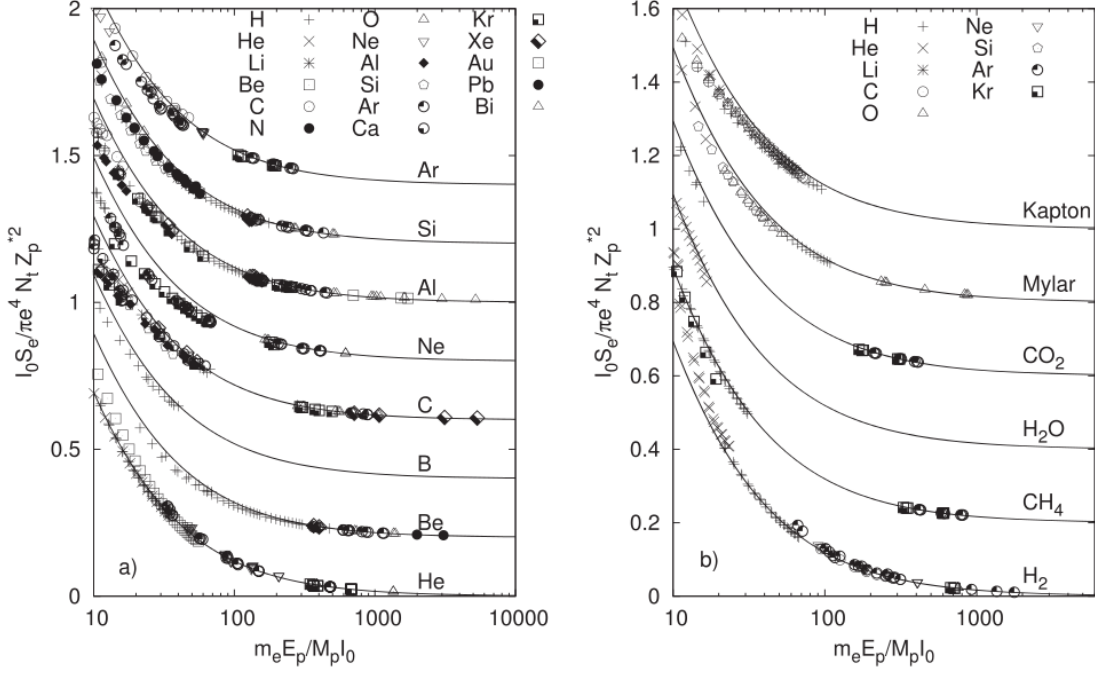
Figure 3.1: (a) Electronic stopping cross section scaling rule for H, He, Li, Be, C, N, O, Ne, Al, Si, Ar, Ca, Kr, Xe, Au, Pb, and Bi heavy ion projectiles colliding with He, Be, B, C, Ne, Al, Si, and Ar atomic targets. The experimental data (symbols) are taken from Refs. [83, 84, 85, 86, 87, 88, 89, 90, 91, 92, 93, 94, 95, 96, 97, 98, 99, 100, 101, 102, 103]. (b) The same as (a), but for several heavy ion projectiles colliding with several molecular targets. The symbols are the experimental data as given in Refs. [87, 98, 104, 88, 90, 95, 105, 106, 107, 108, 109, 110, 111]. Note that each target curve is shifted by 0.2 on the vertical axis to avoid data cluttering.

is in excellent agreement for all the projectiles colliding on all targets. The mean excitation energy is obtained from the FSGO approach, Eq. (2.55), in a core ($1s^2$), bond, and lone pair (LP) orbital decomposition by the Bragg rule [11, 51, 55] [see Eq. (2.47)].

In Fig. 3.2a), I show the theoretical result for $f(\epsilon)$, Eq. (3.2), which shows a very close agreement with the experimental data. In Fig. 3.2a), I show the numerical evaluation of Eq. (3.2) for $M_p = m_p$, the proton mass (H ions, open triangle symbols), $M_p = 4m_p$ (He ions, cross symbol), $M_p = 7m_p$ (Li ions, open square symbols), and $M_p = 16m_p$ (O ions, open circle symbols). From Fig. 3.2a), we observe that the curve is universal for for all projectiles regardless of the explicit dependence of the projectile mass, M_p. These results confirm the universal scaling law for any projectile–target combination at high projectile energies within the first Born approximation.

In Fig. 3.2b), we show the universal scaling by means of Eq. (3.3) for all heavy ion projectiles colliding with all atomic and molecular targets. From 3.2b), for values of $m_e E_p / M_p I_0 > 10$ the universal behavior is fulfilled by all the projectile–target combinations.

3.2 Initial orbital symmetry effects on the stopping power

This section is based on the research **Paper III** contribution as a Ph.D. student.
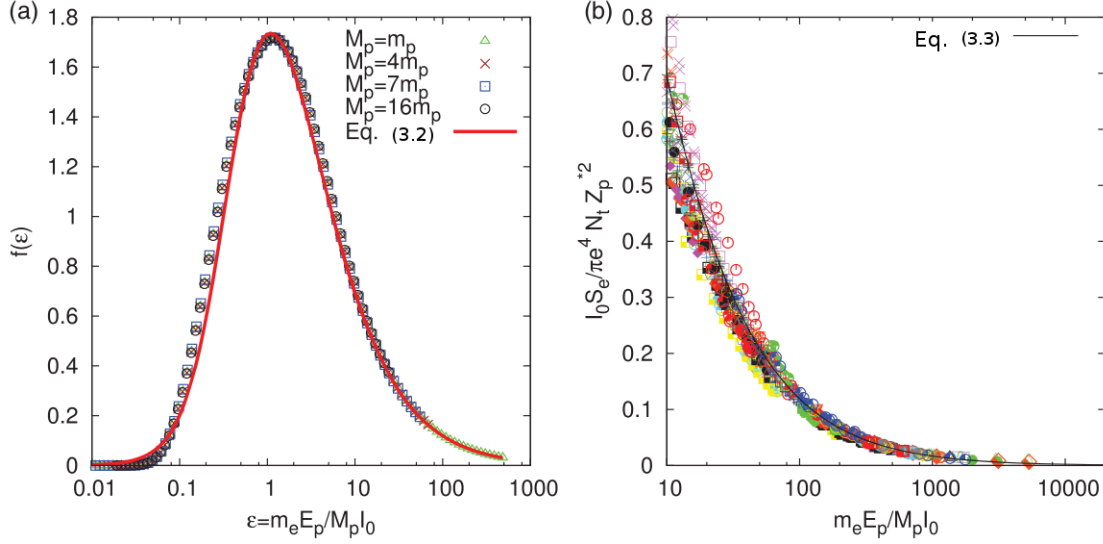
Figure 3.2: (a) Numerical evaluation of Eq. (3.2), $f(\epsilon)$, for proton projectiles $M_p = m_p$ (open triangle symbols), He projectiles $M_p = 4m_p$ ($\times$ symbols), Li projectiles $M_p = 7m_p$ (open square symbols) and O projectiles $M_p = 16m_p$ (open circle symbols). (b) Universal scaling law for all projectiles and all atomic/molecular targets. The symbols are the same experimental data shown in Fig. 3.1. See text for discussion.

3.2.1 Orbital symmetry

An important issue present in the previous description is the initial target symmetry state and the role it plays in the DOS, GOS, and consequently on the stopping cross-section. The orbital symmetry dependence is important when one considers selection rules for electronic transitions, i.e. an electron in an *s*-state would be excited to *p*-state orbitals, a *p*-state electron would be excited to *s*- or *d*-state orbitals for dipole transitions. Thus, the role of the initial state symmetry in the generalized oscillator strengths and, as a consequence changes in the stopping cross-section when accounting for the initial target symmetry should be considered.

3.2.2 Results

From Bethe's theory of energy deposition, the electronic stopping cross section for an ion moving with velocity v, mass M_1, and nuclear charge $Z_1 e$ that collides with a target with mass M_2 and N_2 bound electrons in some initial stationary state is describe by Eqs. (2.41)–(2.43), given explicitly in Chapter 2. The electronic stopping cross section is a function of the GOS given by Eq. (2.43) for a given transferred momentum, q, in an orbital decomposition by the Bragg rule [11, 51, 55]. Then, to take into account for the target electronic structure, we implement the HO approach by considering that every electron of the target is bound harmonically to the nucleus [11]. We assume that the targets electrons position is described by the wave-function of a three-dimensional isotropic harmonic oscillator in Cartesian coordinates [Eq. (2.48)]. The transfer momentum is in the z-direction due to the spherical symmetry of the target. Thus, the GOS that incorporates the initial symmetry is given as

$$F_{n_j n_{0j}}(q) = \frac{2m_e(E_{n_j} - E_{n_0})}{\hbar^2} \left(\frac{n_{0z}!}{n_{jz}!}\right) \left(\frac{1}{q^2}\right) \left(\frac{q^2}{2\alpha_j^2}\right)^{n_{jz}-n_{0z}} \left[L_{n_{0z}}^{n_{jz}-n_{0z}}\left(\frac{q^2}{2\alpha_j^2}\right)\right]^2 e^{-q^2/2\alpha_j^2}, \quad (3.4)$$

with the term $L_n^{m-n}(q)$ is the associated Laguerre polynomial [53]. This is the generalized expression for the GOS for any initial state n_{0j} state to a final state n_j within the HO approach.

Initial s-orbital target symmetry

As a first result of the generalized oscillator strength relation, Eq. (3.4), the s-orbital initial symmetry is given when $n_{0j} = 0$

$$F_{n_j 0}(q) = \frac{1}{(n_j - 1)!} \left(\frac{q^2}{2\alpha_j^2} \right)^{n_j - 1} e^{-q^2/2\alpha_j^2}. \tag{3.5}$$

This result is in complete agreement to the one reported in Ref. [11], which corroborates that our generalized expression for the GOS is correct. The evaluation of the electronic stopping cross section is obtained by direct integration of Eq. (2.42) within the limits given by Eq. (2.37) as

$$S_e(v) = \sum_{i=1}^{N_2} S_{e,i}(v), \qquad S_{e,i}(v) = \frac{4\pi e^4 Z_p^2}{m_e v^2} L_s(v), \tag{3.6}$$

where $L_s(v)$ is the s-symmetry stopping number given as

$$L_s(v) = \sum_{n_j}^{[E_p/I_{0i}]} \frac{1}{2(n_j - 1)!} \left[\Gamma(n_j - 1, x_{min}) - \Gamma(n_j - 1, x_{max}) \right], \tag{3.7}$$

with $\Gamma(n_j - 1, x_{min}^{max})$ being the incomplete gamma function [53] and it is evaluated in the limits

$$x_{min}^{max} = \frac{M_1^2 v^2}{2 m_e \hbar \omega_{0i}} \left(1 \pm \sqrt{1 - \frac{2\hbar \omega_{0i} n_j}{M_1 v^2}} \right)^2. \tag{3.8}$$

Initial p-orbital target symmetry

Now, let us consider the electronic transition from an initial state with p-orbital target symmetry, i.e. $n_{0j} = 1$, to a final excited state. From Eq. (3.4) the GOS are given as

$$F_{n_j 1}(q) = \frac{n_j - 1}{n_j!} e^{-q^2/2\alpha_j^2} \left[n_j - \left(\frac{q^2}{2\alpha_j^2} \right) \right]^2 \left(\frac{q^2}{2\alpha_j^2} \right)^{n_j - 2}, \tag{3.9}$$

where the electronic stopping cross-section is given by Eqs. (2.41)–(2.43) as

$$S_e(v) = \sum_{i=1}^{N_e} S_{e,i}(v), \qquad S_{e,i}(v) = \frac{4\pi e^4 Z_p^2}{m_e v^2} L_p(v). \tag{3.10}$$

Here the stopping number $L_p(v)$ for an initial state with p-symmetry is

$$L_p(v) = \sum_{n_j > 1}^{[E_p/I_{0i}]} \frac{n_j - 1}{2 \, n_j!} \left[-\Gamma(n_j, x) + 2 n_j \Gamma(n_j - 1, x) - n_j^2 \Gamma(n_j - 2, x) \right] \Big|_{x_{min}}^{x_{max}}, \tag{3.11}$$

evaluated in the corresponding limits

$$x_{min}^{max} = \frac{M_1^2 v^2}{2 m_e \hbar \omega_{0i}} \left(1 \pm \sqrt{1 - \frac{2\hbar \omega_{0i}(n_j - 1)}{M_1 v^2}} \right)^2. \tag{3.12}$$

Note the difference on Eqs. (3.8), and (3.12) as the initial orbital symmetry is included also in the limits of the momentum transfer.
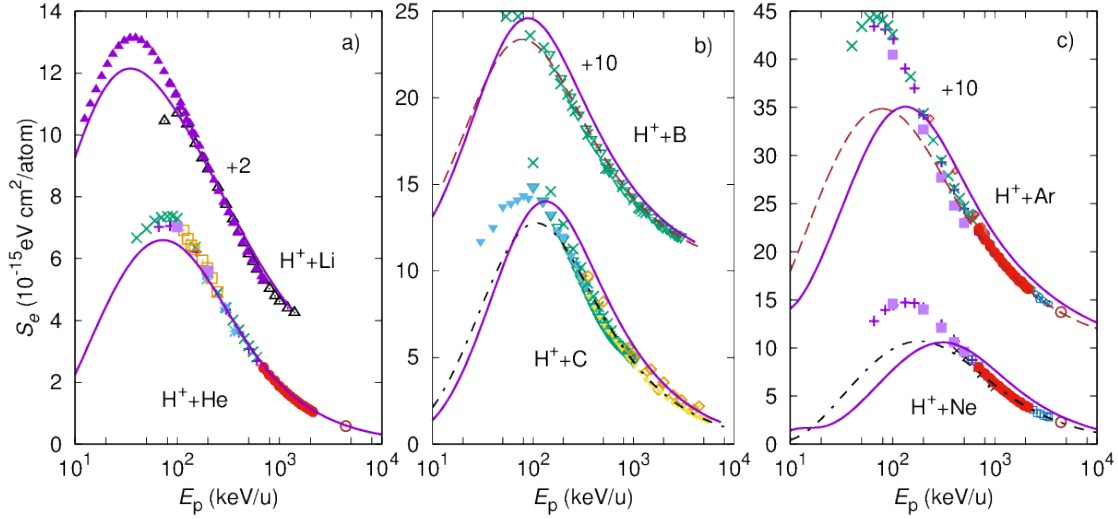
Figure 3.3: Electronic stopping cross-section for protons colliding with several atoms using the target orbital symmetry contribution. In a) we show the results for He and Li, b) for B and C, and c) for Ne and Ar. The solid line is the combination of the $s-$ [Eq. (3.5)] and $p-$ [Eq. (3.9)] target symmetry results and the dashed-line is the contribution by considering all the electrons only in a s-symmetry [Eq. (3.5)] as done originally in Ref. [11]. The symbols are the experimental data from Ref. [113, 104, 114, 115, 116, 117, 98, 118, 119, 120, 121, 122, 123, 124, 125, 126].

Electronic stopping cross section

In Fig. 3.3, we show preliminary results for the total electronic SCS for protons colliding with He, Li, B, C, Ne, and Ar atoms as a function of projectile initial kinetic energy and we compare with available experimental data. I use the mean excitation energy as reported by Oddershede and Sabin [112] and the proper s- and p-symmetry combination of the orbital contribution, Eqs. (3.6) and (3.10). In Fig. 3.3a), I show the results for He and Li atoms (lines) using the HO results for the $s-$symmetry observing a good agreement when comparison is made to the experimental data for large values of projectile kinetic energy. In Fig. 3.3b), I show the results for B and C atoms which have open p valence electrons. We have used the effective charge approach from Betz (solid lines) and compare our results with the available experimental data. In the same figure, I show the electronic stopping cross-section, as obtained by assuming that all the electrons are in an initial s-orbital symmetry, i.e. by using only the $n_{0j} = 0$ assumption originally reported in Ref. [11] (dashed line). From Fig. 3.3b), the inclusion of the p-state symmetry modifies the slope when compared to the experimental data. In Fig. 3.3c), I show the results for Ne and Ar targets. For noble gas targets I use the bare projectile charge. The solid line is the stopping cross-section with the inclusion of the p-orbital symmetry and the dashed-line is the result of only using the s-orbital assumption on all the electrons. From our results one observes the relevance of including the initial state target symmetry in the stopping cross section.

3.3   Conclusions and perspectives

In Section 3.1, I have shown that an universal scaling behavior of the electronic stopping cross section occurs for all projectile–target systems when one considers the initial s-orbital target symmetry. This expression was obtained within the harmonic oscillator approach, neglecting charge exchange effects processes, however the scaling dependence is universal, as shown by the experimental evidence. The results show the relevance of the mean excitation energy to account for the electronic stopping cross

section. The scaling law expresses a systematic and universal behavior among complex projectile–target systems in the energy deposition, regardless of the detailed mechanism for slowing down in the intermediate-to-high collision energies.

In Section 3.2, I have shown that by accounting for the initial orbital symmetry of the target, new expressions for the electronic stopping cross section are derived. These results are obtained within the assumption that the electron can be described within an Harmonic Oscillator approach and shows the effects on the initial target's electron symmetry when comparing to the experimental data, confirming our initial assumptions. Bethe's theory includes the target orbital symmetry through the mean excitation energy, however in this work, I have shown that the target symmetry is required to be take into account in the Generalized Oscillator Strength, to evaluate the stopping cross-section properly.

As I observe from the results, the initial target symmetry is relevant in the calculation of the electronic stopping cross section. As a future work, a more realistic approach is to consider the spherical symmetry of the problem by means of a Coulomb attraction for the target electrons and an initial orbital target symmetry (s, p, d etc.) for the GOS. This work is in progress.

4

Endohedral hydrogen atom

In this chapter, I explore the hydrogen (H) atom electronic properties at extreme conditions, where I mainly follow the results reported in **Paper II**. In the first part of this chapter, I consider a hydrogen atom encaged by an endohedral cavity, e.g. inside a fullerene molecule $A@C_n$. Firstly, I obtain the eigenvalues and eigenfunctions for the $H@C_{60}$ system by solving the time-independent Schrödinger equation within a finite-differences approach as given in Chapter 2. The C_{60} fullerene cage is accounted for by two model potentials: a) the square-well and b) the Woods-Saxon. We propose to use the Woods-Saxon potential to study the role of a smooth cavity on the hydrogen atom Generalized and Dipolar oscillator strength distribution (GOS and DOS). Both models characterize the cavity by an inner radius R_0, thickness Δ, and a well depth V_0. Furthermore, the Wood-Saxon model potential is characterized by a smooth parameter γ. The electronic properties of the confined hydrogen atom are reported as a function of the well depth V_0, emulating different electronic configurations of the endohedral cavity. We report results for the photo-ionization cross section, the mean excitation energy, and the electronic stopping cross section (energy loss).

4.1   Endohedral confinement

Atoms encaged by an endohedral cavity $A@C_{60}$ have received much attention in recent years because of the change of their electronic properties when subjected to spatial confinement [60]. An immediate consequence of the confinement on the encaged atom is the energy level shift and the modification of the wave function with a consequently change in the Dipole and Generalized Oscillator Strength (DOS and GOS, respectively), and therefore a change in the properties related to them. Some previous studies of DOS dependent properties for the $A@C_n$ system can be found in the literature. For example, there have been theoretical investigation efforts to determine the photo-ionization cross section for endohedral confinement since giant resonances have been predicted [22, 23, 24, 25, 26, 127, 128, 129]. These huge resonances are the result of the trapping of incoming and outgoing waves in the endohedral cavity and recently have been confirmed experimentally for a Xenon atom under endohedral confinement [130]. For the $H@C_{60}$ system, the work of Dolmatov et al. [25] shows theoretical results for the photo-ionization cross section using a numerical approach. Dolmatov et al. [25] find the presence of energy resonances in the photo-ionization cross section as a function of the potential well depth. Lin and Ho [26] report results for the photo-ionization cross section of $H@C_{60}$ implementing finite-element methods finding a significant influence of cage thickness and smooth shell boundary on the photo-ionization resonances. In the field of material damage induced by collisions, relevant in material science, the quantum mechanical study of the energy loss by a bare ion colliding with a target is carried out by means of Bethe's theory [131]. In Bethe's approach, the projectile's linear momentum transferred to the bound target electrons during the collision is the main process for energy loss into electronic excitations and ionization. Thus, in Bethe's theory, only the electronic structure of the target atom is required to account for the energy loss process. This approach is valid for high projectile velocities where charge-exchange effects are negligible. For large projectile velocities, the energy deposition is characterized by the mean excitation energy, I_0, a parameter that accounts for how much the target absorbs energy from the projectile. Some studies report the mean excitation
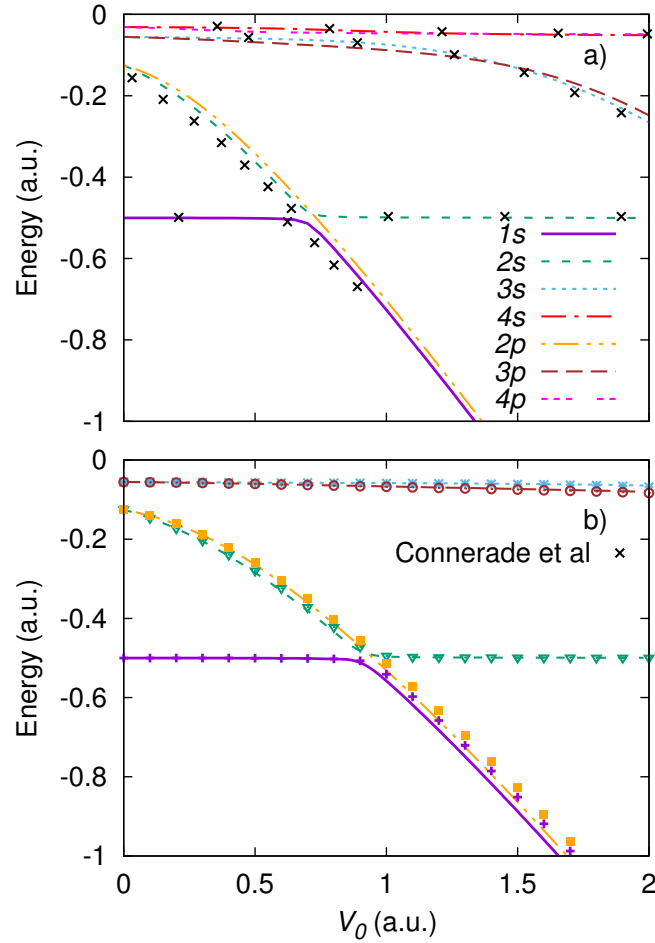
Figure 4.1: Energy levels of the hydrogen atom encaged by an endohedral cavity as a function of the well depth V_0 for the $1s - 4s$ and $2p - 4p$ states. a) Results obtained by means of the square-well potential (color lines) for the case of the first set of parameters $R_0 = 5.8$ a.u., and $\Delta = 1.89$ a.u.. The results are compared to those of Connerade et al. [23] ($\times$). b) Results for the square-well (color lines) and the Wood-Saxon (symbols with same color-line) potentials for the case of the second set of parameters $R_0 = 6.01$ a.u., and $\Delta = 1.25$ a.u.. Note the shift of the avoided crossings towards larger V_0. See text for details.

energy for a hydrogen atom under pressure by a penetrable or impenetrable spherical cavity [132, 133], but to the authors knowledge, none is reported for endohedral atoms. Outside Bethe's approximation, the GOS account for the target energy absorption, due to the projectile momentum transfer [131]. In the case of a free hydrogen atom, the analytic expressions for the GOS have been available in the literature [134, 49, 135]. However, for endohedral systems, this is not the case, and a numerical approach for the calculation of the GOS is need. For fullerene targets, there are several studies that report theoretical and experimental stopping cross section (SCS). For example, Moretto-Capelle et al. [136] (and references therein) report the theoretical energy deposited by protons colliding with C_{60} molecules finding that the fullerene molecules behave as a carbon foil. For a confined system, the stopping power for protons colliding with atomic hydrogen under pressure by a spherical cavity is reported by Cabrera-Trujillo and Cruz [133] finding that, as pressure increases, the stopping power is reduced.

4.1.1 Results

In this section, we present the study of the hydrogen atom encaged by a C_{60} fullerene molecule (H@C_{60}) using two parameter sets to describe the cavity. The first set is $R_0 = 5.8$, $\Delta = 1.89$, $\gamma = 0.1$ and the second set is $R_0 = 6.01$, $\Delta = 1.25$, $\gamma = 0.1$. We report the energy spectrum and wave-function results by solving the time-independent Schrödinger equation by means of a finite-differences approach. Then, we calculate the DOS and GOS derived dependent electronic properties, e.g. photo-ionization [Eq. (2.24)], mean excitation energy [Eq. (2.46)], and the electronic stopping cross section [Eqs. (2.56)–(2.58)]. Here, the GOS are given by Eq. (2.57) that take into account the s-initial orbital symmetry. The numerical details were given in Section 2.8.

Energy levels and wave-functions

To obtain a proper description of the electronic properties given by our theoretical approach, we need to obtain the appropriate energy levels and wave-functions for the H@C_{60} system. In Fig. 4.1, we show the energy levels of the hydrogen atom encapsulated by an endohedral cage. The energies of the $1s$ to $4s$ and $2p$ to $4p$ states are shown as a function of the well depth V_0. In Fig. 4.1a), we show the results for the square-well potential with the first set of parameters that model the C_{60} endohedral cavity, i.e. $R_0 = 5.89$ a.u., and $\Delta = 1.89$ a.u.. In the same figure, we compare with the results reported by Connerade et al. [23] ($\times$), observing a good agreement. As the well depth V_0 becomes deeper, we observe an avoided crossing region between the ns and the $(n+1)s$ states for near degenerate states at around $V = 0.7$ a.u. for several energy levels of the square-well potential. This avoided crossing is a characteristic that shows the migration of the lower energy state, from being in the atom to being in the endohedral cage. From Fig. 4.1a), we observe that for values of well depths $V_0 > 0.7$ a.u., the $1s$ state migrates to the endohedral cage. In Fig. 4.1b), we show the results for the case of an endohedral cavity modeled by the square-well potential with the second set of parameters $R_0 = 6.01$ a.u. and $\Delta = 1.25$ a.u. (color lines), as the ones used by Dolmatov [25], which is a cavity slightly larger than the case shown in Fig. 4.1a). Here, for the same potential well depth values, the avoided crossings have shifted towards larger values of V_0 consequence of the larger endohedral cavity. In Fig. 4.1b), we compare to the results obtained by using a Woods-Saxon potential with the same parameter values and $\gamma = 0.1$ a.u. represented with symbols with the same color-line. The Woods-Saxon results for the eigenvalues are almost identical to the case of the square well potential for shallow cavities. Thus, the discontinuity of the square-well potential plays a small role in the energy-spectrum of the endohedral confined H system for small V_0 in agreement to Dolmatov's findings [81]. Furthermore, for large values of V_0, some discrepancies start to be observed and become important in the calculation of the GOS dependent properties. For example, for a well depth of $V_0 = 1.7$ a.u., we note a discrepancy of around 5% in the $2p$ energy level state. This is due to the increase of the confinement effect by the endohedral cavity on the $2p$ state such that the tunneling of the wave-function is different for both potentials (see below). This discrepancy is increased as V_0 increases.

In Figs. 4.2(a-d), we show the eigenfunctions for the $1s$, $2s$, $2p$, and $3p$ states of the endohedral H system for the square-well potential with the first set of parameters, $R_0 = 5.8$ and $\Delta = 1.89$ a.u., for values of the well depth $V_0 = 0.0, 0.302, 0.7$, and 1.0 a.u.. For the case of the free atom, $V_0 = 0.0$ a.u., we observe an excellent agreement with the analytic solutions shown by ($\circ$) symbols. As the well depth increases to $V_0 = 0.302$ a.u., we observe, in Figs. 4.2b) and 4.2c), that the $2p$ and $2s$ wave-functions are modified significantly in comparison with the $1s$ and $3p$ states shown in Figs. 4.2a) and 4.2d), respectively. Note that the values $R_0 = 5.8$, $\Delta = 1.89$ a.u., and $V_0 = 0.302$ a.u. are the characteristic parameters that describe a C_{60} fullerene molecule under this model potential approach, as reported by Xu et al. [69, 63]. For a well depth near the first avoided crossing, $V_0 = 0.7$ a.u., we observe in Fig. 4.2b), that the $2p$ wave-function is completely confined in the cage region between $6 < r < 8$ a.u.. Furthermore, the $1s$ [Fig. 4.2a)] and $2s$ [Fig. 4.2c)] wave-functions are split partially between the C_{60} cage region and the hydrogen atom nuclear position. In Figs. 4.2a) and 4.2c), we compare our results for the $1s$ and $2s$ wave-functions with those given by Connerade [23] ($\triangle$) for a well depth $V_0 = 0.7$ a.u. observing an excellent agreement. For a well depth of $V_0 = 1$ a.u. in Fig. 4.2a) and
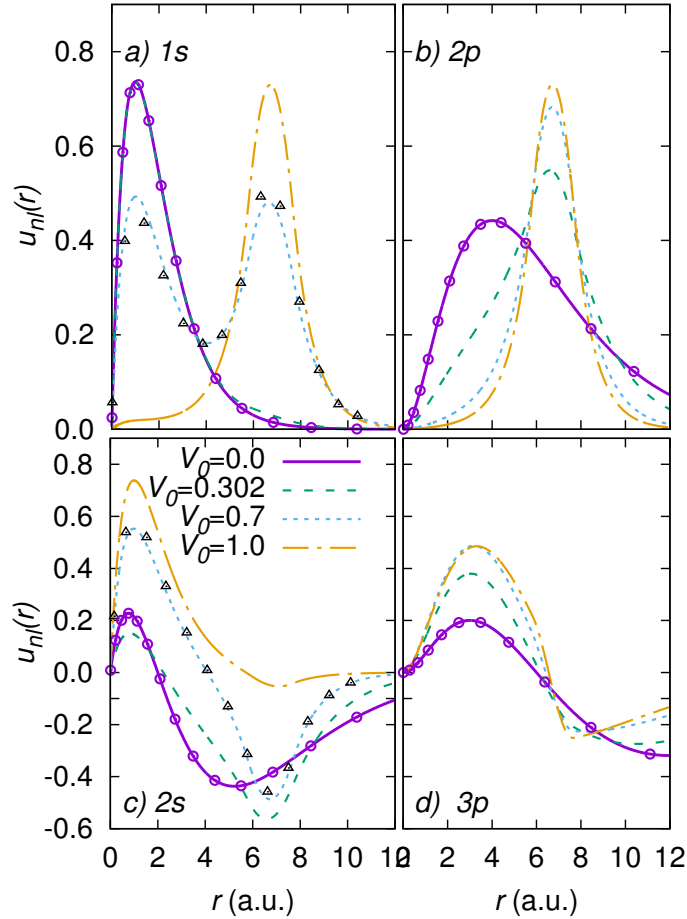
Figure 4.2: Radial wave function, $u_n(r)$, for the $1s$, $2s$, $2p$, and $3p$ states of the hydrogen atom encaged by an endohedral cage (color lines) for selected well depths, V_0, for the case of the square-well potential with the first set of parameters $R_0 = 5.8$ a.u. and $\Delta = 1.89$ a.u.. Our results are compared to those of Connerade et al. ($\triangle$) [23] for the $1s$ and $2s$ states at $V_0 = 0.7$ a.u.. The ($\circ$) symbols are the analytic results for the free case. See text for details.

4.2b), the wave-functions for the $1s$ and $2p$ states are bound in the cavity region with no contribution at the hydrogen atom position. Here the electron is completely bound by the cage with the lowest energy state being at the endohedral cavity. Furthermore, the $2s$ wave function is now bound by the Coulombic potential, as observed in Fig. 4.2c), and takes the characteristics of the unconfined $1s$ function, a result in agreement with Connerade et al. [23]. Thus, the wave functions are modified by the presence of the endohedral cage producing a trapping of the electron within the endohedral cavity as the well depth increases.

Dipole oscillator strength

Once we have calculated the eigenvalues and eigenfunctions, we are ready to obtain the DOS and as a consequence the photo-ionization cross section for the H@C$_{60}$ system. In Fig. 4.3, we show the $1s \rightarrow 2p$ transition as a function of the well depth V_0 for the case of the first set of parameters, $R_0 = 5.8$ and $\Delta = 1.89$ a.u. (solid line) as well as for the second set of parameters, $R_0 = 6.01$ and $\Delta = 1.25$ a.u. for both the square-well (long dashed line) and the Woods-Saxon (short-dashed line) potentials. The ($\blacksquare$) symbol corresponds to the exact free value, $f_{1s \rightarrow 2p} = 0.41619$ in agreement to that
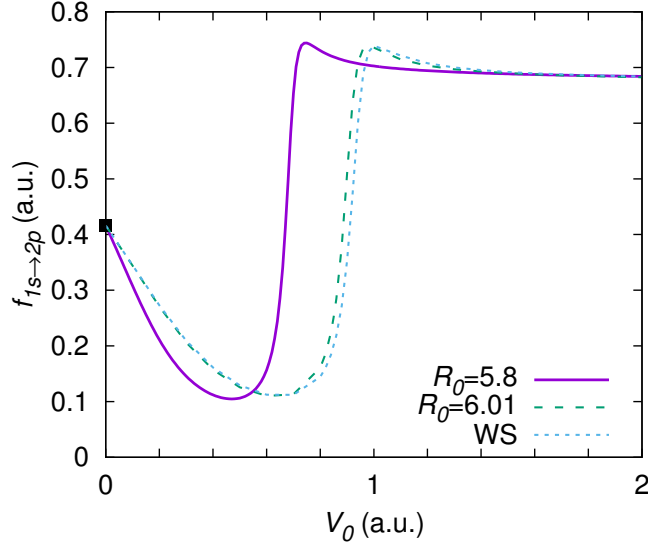
Figure 4.3: Dipole oscillator strength for the $1s \to 2p$ transition of a hydrogen atom confined by a endohedral cavity as a function of the well depth V_0. Solid line represents the results for the square-well potential for the case of the first parameter set, $R_0 = 5.8$ and $\Delta = 1.89$ a.u.. The dashed and short-dashed lines are the results for the case when the parameter set is $R_0 = 6.01$ and $\Delta = 1.25$ a.u., for the square-well (long dashed line) and Woods-Saxon (short dashed line) potentials with $\gamma = 0.1$ a.u., respectively. The ($\blacksquare$) symbol corresponds to the exact free case, $f_{1s \to 2p} = 0.4162$ a.u. i agreemen to Wiese et al. [137]. See text for details.

reported by Wiese et al. [137]. From the figure, we observe that around the near degeneracy, the DOS suffer a significantly change at $V_0 = 0.7$ a.u. for the square-well and for the first parameter set with $R_0 = 5.8$ a.u.. For the first parameter set, the DOS decay from 0.4161 (free case), until a minimum value of 0.1063 at $V_0 = 0.5$ a.u., then, it reaches a maximum value around $V_0 = 0.8$ a.u. and then reaches a value of 0.68 for large V_0. Observe that, this behavior is completely related to the change of the $1s$ eigenfunction between being at the hydrogen atom and then localizing the $1s$ electron in the endohedral cavity as the potential well depth increases. For the second parameter case, $R_0 = 6.01$ and $\Delta = 1.25$ a.u., where the avoided crossing appears, the square-well and Woods-Saxon potentials presents a similar behavior as before with the drastic change shifted to around $V_0 = 0.9$ a.u.. For the second parameter set, there exist a slightly difference for $0.6 < V_0 < 1.2$ a.u. between the square-well and Woods-Saxon potentials results due to the effect of the discontinuity of the square-well potential at the borders of the endohedral cavity. This difference can reach up to a 30 %, as observed in Fig. 4.3.

Photo-ionization cross section

The first DOS derived property that we have calculated is the photo-ionization cross section (PCS) for an endohedral H atom for several well depths V_0 as a function of the photo-electron energy due to the relevance in material damage. In Fig. 4.4a), we show the results for the square-well potential with parameter set $R_0 = 5.8$ and $\Delta = 1.89$ a.u.. In Fig. 4.4b), we show the results for the square-well (dashed color lines) and Woods-Saxon (symbols with same color-line) potential with parameter set $R_0 = 6.01$ a.u., $\Delta = 1.25$ a.u., and $\gamma = 0.1$ a.u.. As the photo-ionization cross section has been calculated previously for the second parameter set and the Woods-Saxon potential by Dolmatov et al. [25], we will use these results to establish the validity of our numerical method and to asses the proper description of the photo-ionization cross section. In Fig. 4.4b), we show the results of Dolmatov et
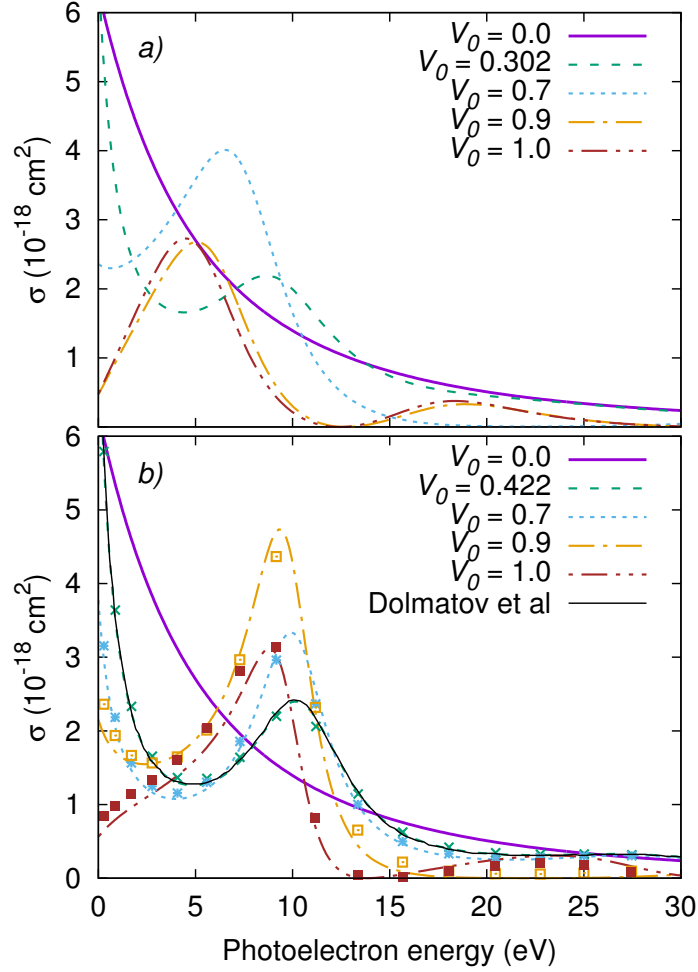
Figure 4.4: Photo-ionization cross section for an endohedral H atom as a function of the photo-electron energy (eV) for different well depths V_0. a) Results for the case of the square-well potential (color lines) with first parameter set $R_0 = 5.8$ a.u. and $\Delta = 1.89$ a.u.. b) Results for the case of the square-well (color lines) and Woods-Saxon potentials (symbols with same color-line) with second parameter set $R_0 = 6.01$ a.u., $\Delta = 1.25$ a.u., and $\gamma = 0.1$ a.u.. In b) we show the results of Dolmatov et al. [25] (thin solid black line) for a potential well depth of $V_0 = 0.422$ a.u. for comparison purposes. See text for discussion.

al. [25] (thin solid black line) for the case of $V_0 = 0.422$ a.u. showing an excellent agreement with our calculations. In Fig. 4.4a) and 4.4b), we observe the confinement resonances (Cooper resonances) that occur due to the constructive interference of the photo-electron waves scattered off by the endohedral cage and the outgoing photo-electron wave [138, 25]. From both parameter set, we find that the position of the Cooper resonances are strongly dependent on the endohedral cavity parameters. For the parameters that describe a C_{60} cavity, $R_0 = 5.8$, $\Delta = 1.89$, and $V_0 = 0.302$ a.u., shown in Fig. 4.4a), we find that the first Cooper resonance appears at 8 eV and the second at around 25 eV. For the second set of parameters, $R_0 = 6.01$, $\Delta = 1.25$, and $V_0 = 0.422$ a.u., shown in Fig. 4.4b), the first resonance appears at a photo-electron energy around 10 eV and the second one at around 28 eV. As we observe from Fig. 4.4, the PCS is sensitive to the parameters used to model the endohedral cavity. A clear discrepancy between the two sets of parameters is present for $V_0 = 0.9$ a.u.. There is an increase of the cross section at a photo-electron energy around 10 eV for the results with $R_0 = 6.01$
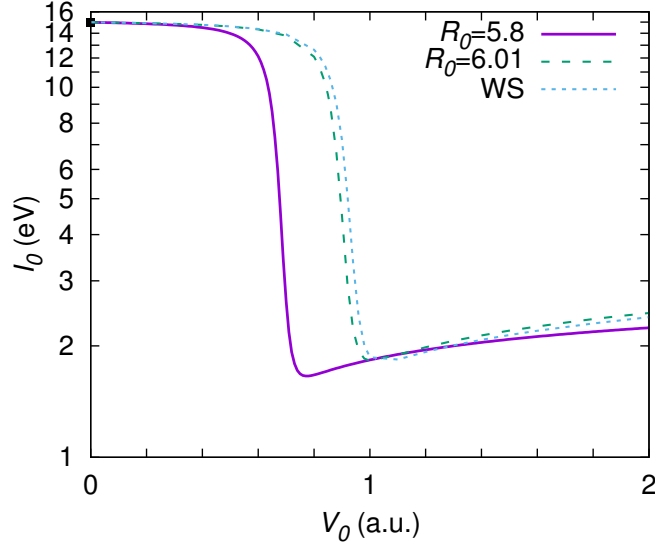
Figure 4.5: The same as Fig. 4.3, but for the mean excitation energy, I_0. In this case, the (■) symbol corresponds to the free case as reported by Cabrera-Trujillo and Cruz [133] with $I_0 = 14.9930$ eV. See text for details.

a.u. rather than those with $R_0 = 5.8$ a.u.. As we observe from the difference of the results in Fig. 4.4, the photo-ionization cross section experimental data can be used to adjust the set of parameters that properly describe the endohedral cavity [69]. In Fig. 5.6b), we observe a slight change between the square-well and Woods-Saxon potential results for the PCS for a photo-electron energy around the first Cooper resonance that is near the first avoided crossing ($V_0 = 0.9$ a.u.). The differences are more evident for photo-electron energies lower than 10 eV.

Mean excitation energy

As we mentioned in the Introduction of this chapter, the mean excitation energy, I_0, is related to the stopping cross section (energy loss) by means of Eq. (2.46) under the Bethe approach [131]. In Fig. 4.5, we show the mean excitation energy as a function of the well depth, V_0. The solid line is the result for the squared well potential with cavity size $R_0 = 5.8$ a.u. and $\Delta = 1.89$ a.u.. The dashed and short-dashed lines are the results for a cavity size with $R_0 = 6.01$ a.u. and $\Delta = 1.25$ a.u., for the square-well and Woods-Saxon potential, respectively. In the free case [$V_0 = 0.0$ a.u.], we reproduce the result of $I_0 = 14.9930$ eV (■) from Cabrera-Trujillo and Cruz [133]. As we observe from the figure, I_0 decreases from $I_0 = 12.1300$ eV at $V_0 = 0.6$ to $I_0 = 1.6590$ eV at $V_0 = 0.77$ a.u., then increase until $I_0 = 2.4330$ eV at $V_0 = 3.0$ a.u. for the cavity size $R_0 = 5.8$ a.u.. For the cavity size with $R_0 = 6.01$ a.u. we observe the same behavior but shifted towards the first avoided crossing for well depth $V_0 = 0.9$ a.u.. The drastic change in I_0 is related to the change of the $1s$ and np wave-functions as the well depth increases, see Fig. 4.2, and the DOS $1s \rightarrow 2p$ transition which is the principal intensity contribution. The stopping cross section will be modified as the well depth is increased.

Generalized oscillator strength

In Fig. 4.6, we show the GOS for the $1s \rightarrow 2s$ [F_{2s}, Figs. 4.6a) and 4.6c)] and $1s \rightarrow 3s$ [F_{3s}, Figs. 4.6b) and 4.6d)] transitions as a function of the transferred momentum, q, for a selected set of well depths. In Figs. 4.6a) and 4.6b), we show the results for the square-well potential (lines) for the cavity size with $R_0 = 5.8$ a.u. and $\Delta = 1.89$ a.u.. In Figs. 4.6c) and 4.6d) we show the results for the
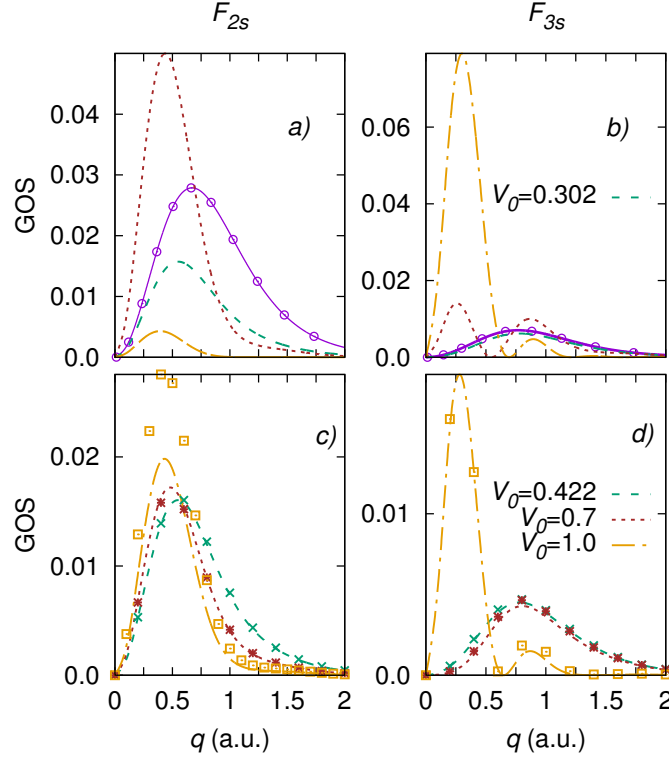
Figure 4.6: Generalized oscillator strength for the F_{2s} and F_{3s}, transitions for atomic hydrogen in an endohedral cavity, as a function of the momentum transfer, q, for several confinement well depths. In Figs. 4.6a) and 4.6b), we show the results for the square-well potential with cavity size $R_0 = 5.8$ and $\Delta = 1.89$ a.u.. The ($\circ$) symbols are the analytic results for the free case and we show the characteristic value of the well depth $V_0 = 0.302$ a.u.. In Figs. 4.6c) and 4.6d), we show the results for the square-well (color lines) and Woods-Saxon (symbols with same color-lines) potentials with cavity size $R_0 = 6.01$ and $\Delta = 1.25$ a.u. for the same set of confinement well depths, as well the characteristic value of the well depth $V_0 = 0.422$ a.u. for this endohedral cavity size. See text for details.

square-well (lines) and Woods-Saxon potentials (symbols with same color-line) for a cavity size with $R_0 = 6.01$ a.u., $\Delta = 1.25$ a.u., and $\gamma = 0.1$ a.u.. For comparison, the analytic GOS results for the free atom [57] ($V_0 = 0$ a.u., open circles) are reported showing an excellent agreement to our numerical calculations for the squared well potential with $R_0 = 5.89$ a.u.. In Fig. 4.6a), for values of V_0 below the avoided crossing, we observe a reduction of the F_{2s} curve. At $V_0 = 0.7$ a.u., the F_{2s} curve increases significantly and reduces its width in comparison with the free case. For V_0 larger that the avoiding crossing, the GOS curve diminishes again. In Fig. 4.6b), we observe a similar behavior for the F_{3s} only that the increase is given for a well depth of $V_0 = 1.0$. Fig. 4.6c) shows the results for F_{2s} but for a cavity size of $R_0 = 6.01$ a.u., observing a different behavior in comparison with the cavity size of $R_0 = 5.89$ a.u.. Here, the F_{2s} curves remain very similar for values below $V_0 = 0.9$ a.u. and then there is an increase for $V_0 = 1.0$ a.u.. From Fig. 4.6c), we observe a large difference between the square-well and Woods-Saxon model potentials results for $V_0 = 1.0$ a.u. that is evient near the maximum of F_{2s}, consequence of the smoothness of the shell cavity. In Fig. 4.6d), it is observed a notorious decrease by a factor of 3 for F_{3s} in the case of the well depth $V_0 = 1.0$ a.u. in comparison with those found in Fig. 4.6b). As we observe from Fig. 4.6, we find some differences for the two cavity potential models that depend on the momentum transfer.

In Fig. 4.7, we show the GOS for the $1s \rightarrow 2p$ [F_{2p}, Figs. 4.7a) and 4.7c)] and $1s \rightarrow 3p$ [F_{3p}, Figs. 4.7b) and 4.7d)] for a selected set of potential well depths, as a function of q. In Figs. 4.7a) and 4.7b),
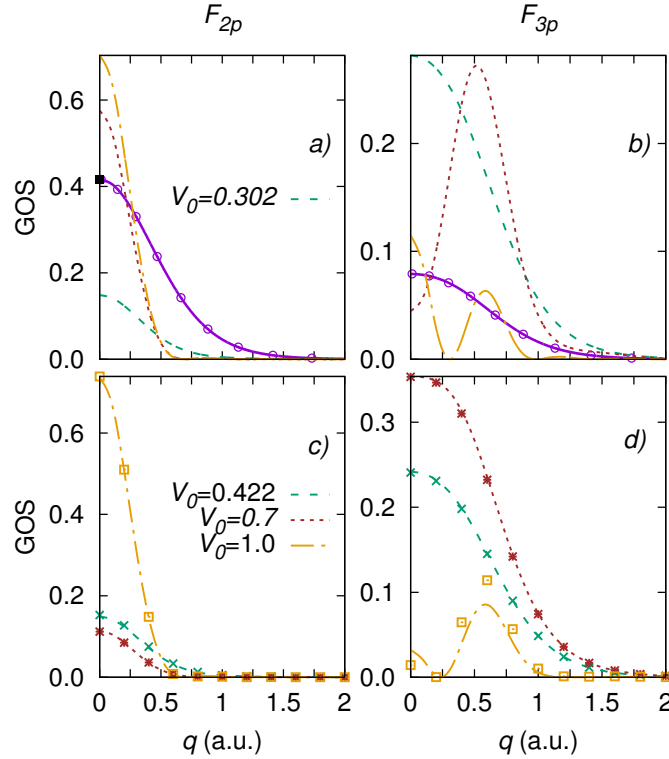
Figure 4.7: (Color on-line). The same as in Fig. 4.6, but for the F_{2p} and F_{3p} transitions. The ($\blacksquare$) symbol is the results for $q = 0$ where the F_{2p} is reduced to the DOS transition $f_{1s \to 2p} = 0.4161$.

we show the results for the square-well potential (lines) for a cavity size $R_0 = 5.8$ a.u. and $\Delta = 1.89$ a.u.. In Figs. 4.7c) and 4.7d), we show results for the square-well potential (lines) and Woods-Saxon potentials (symbols with same color-lines) for a cavity size $R_0 = 6.01$ a.u., $\Delta = 1.25$ a.u., and $\gamma = 0.1$ a.u.. The ($\blacksquare$) symbol corresponds to the case when $q \to 0$ in F_{2p}, i.e. $f_{1s \to 2p} = 0.41619$. From Fig. 4.7a), we observe a decrease in F_{2p} for $V_0 = 0.302$ a.u. (green-dashed line) and an increase for larger values of the well depth. Meanwhile in Fig. 4.7c), we observe that F_{2p} remains very similar for $V_0 = 0.422$ when $R_0 = 6.01$ a.u. than for the case when $R_0 = 5.89$ a.u. and $V_0 = 0.302$ a.u. [see Fig. 4.7a)]. The case of $V_0 = 0.7$ is smaller in this case in comparison with the result given in Fig. 4.7a). The F_{2p} for the potential well depth of $V_0 = 1.0$ a.u., remains very similar for both well cavity sizes. Furthermore, the square-well and Woods-Saxon potential results are very similar, implying that for this case the effects of the discontinuity in the potential are negligible. In Fig. 4.7b), for the F_{3p}, we observe an increase for $V_0 = 0.302$ a.u. and then we observe a maximum at the avoiding crossing $V_0 = 0.7$ a.u. for $q \sim 0.5$ a.u. followed by a double maximum for $V_0 = 1.0$ a.u.. In comparison, in Fig. 4.7d), for the larger cavity size $R_0 = 6.01$, we observe a larger increase in F_{3p} for $V_0 = 0.7$ a.u. as compared to those obtained in Fig. 4.7b). Besides, a large difference is found between the square-well potential results for F_{3p} shown in Fig. 4.7b) and those shown in Fig. 4.7d) at $V_0 = 1.0$ a.u.. Additionally, a difference is observed between the square-well and Woods-Saxon potentials for $V_0 = 1.0$ a.u. (just above the avoiding crossing), which confirms that the discontinuity in the square-well is relevant in the determination of GOS and is strongly dependent on the momentum transfer.

Electronic stopping cross section

In Fig. 4.8, we show the electronic SCS for protons colliding with atomic hydrogen encaged for the two confining sizes of the endohedral cavity. We show the change of the SCS at different well depth values
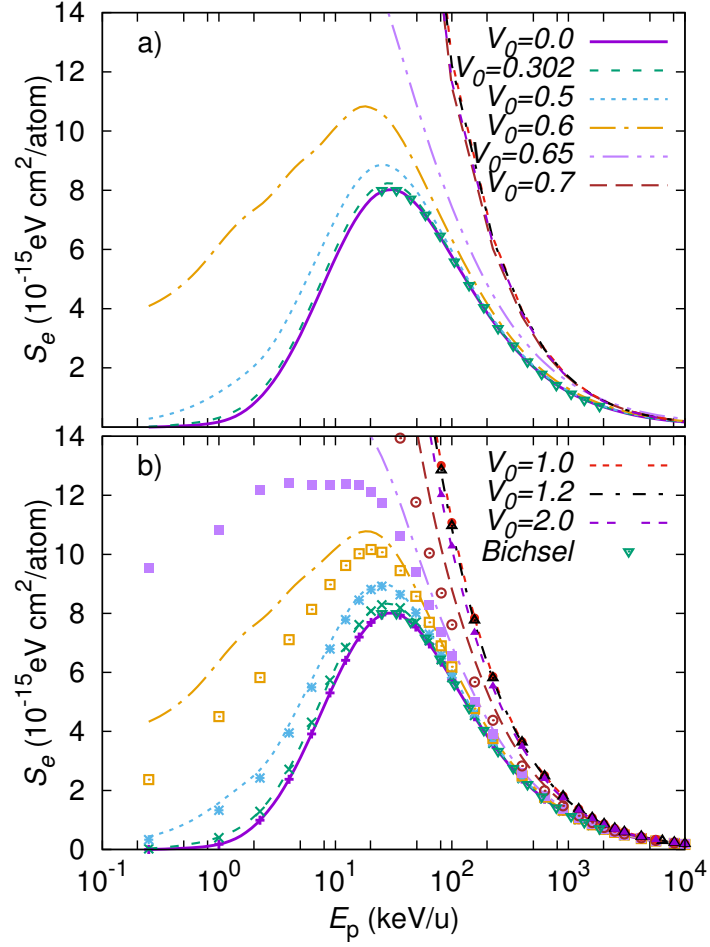
Figure 4.8: Electronic stopping cross section for protons colliding with atomic hydrogen encaged by an endohedral cavity as a function of projectile initial kinetic energy for several confinement well depths V_0. a) shows the results for the case of the square-well potential with cavity size $R_0 = 5.8$ a.u. and $\Delta = 1.89$ a.u.. b) shows the results for the case of the square-well potential (lines) and Woods-Saxon potentials (symbols with the same color-lines) for a cavity size with $R_0 = 6.01$ a.u., $\Delta = 1.25$ a.u., and $\gamma = 0.1$ a.u.. The (∇) symbols are the free atomic hydrogen results of Bichsel [139]. See text for details.

as a function of the projectile initial kinetic energy. We compare our results for the free case with those given by Bichsel [139] based in the first Born approximation (∇) observing an excellent agreement to our $V_0 = 0.0$ case. In Fig. 4.8a), we show the results for the square-well potential with cavity size $R_0 = 5.8$ a.u. and $\Delta = 1.89$ a.u. As we observe from the figure, the largest effect of the endohedral cavity on the GOS dependent electronic properties is in the low energy collision where an increase in the stopping cross section is found. As the well depth increases, the stopping cross section increases too, observing a fastest change near the first avoided crossing, i.e. $V_0 = 0.7$ a.u.. At high projectile energies, the endohedral cavity is not discernible by the projectile. In Fig. 4.8b), we show the results for the square-well (color lines) and Woods-Saxon potentials (symbols with the same line-color) for a cavity size $R_0 = 6.01$ a.u. and $\Delta = 1.25$ a.u.. Although the behavior is similar to the previous case, we observe some differences at the same well depth. For example, near the degeneracy ($V_0 = 0.9$ a.u. in this case) the discrepancy between the square-well and Woods-Saxon potential is evident. This means

that there is a strong effect on the GOS dependent properties due to the discontinuity of the potential that models the endohedral cavity.

4.1.2   Conclusions and perspectives

In this chapter, I have analyzed the role of spatial confinement on the dipole and generalized oscillator strength physical properties of a hydrogen atom enclosed by an endohedral cavity by means of two model potentials: the square-well and Woods-Saxon potentials as a function of the well depth V_0. Furthermore, I have used two sets of parameters, as found in the literature, to describe a C_{60} endohedral cage. It was found that the physical properties depend strongly on these values. Even more, with the increase of the well depth, the GOS intensities are modified for the two sets of parameters, representing different electronic configurations of the endohedral cavity. A slight difference was observed when I compare the DOS for the square-well and Woods-Saxon potential, as a result of the discontinuity at the borders of the first model. Particularly, the drastic changes are predominant near the first avoided crossing of the energy levels for both set of parameters considered, due to the drastic change of the $1s$ wave-function as it is confined by the endohedral cavity. We found that, for the photo-ionization cross section and mean excitation energy, the differences between the two model potential approaches is up to 30% for values of V_0 near the first avoided crossing.

Some interesting aspects of the results presented here can be considered for a further study. For example, the use of square well and the Wood-Saxon model potential could be improved by adding a repulsive contribution on the model potentials or by considering the dynamic of the $H@C_{60}$ system by implementing a time-dependent method to account for the C_{60} atoms interacting with the hydrogen atom.

In the following chapter, I consider some another confinement environment given by a plasma medium. In this approach, I study an enhdohedral hydrogen atom system embedded in a plasma environment. This novelty system has been confirmed recently in interstellar plasmas, leaving an interesting system to study.

5

Endohedral hydrogen atom in a plasma environment

In this chapter, I study a hydrogen atom under extreme conditions, e.g. a hydrogen atom encaged by an endohedral cavity under the influence of a weak plasma interaction, following mainly the results reported in **Paper IV**. The study is based on the implementation of a finite-differences approach, applied to a hydrogen atom in an endohedral cavity which is modeled by the Woods-Saxon potential as defined before. The plasma interaction is described by a Debye-Hückel screening potential that characterizes the plasma in terms of a Debye screening parameter λ_D. The electronic properties of the endohedral hydrogen atom are reported for selected endohedral cavity well depths V_0 and screening lengths λ_D that emulate different confinement and plasma conditions for the system. Here, I assess and report the photo-ionization cross section, mean excitation energy, and the electronic stopping cross section. I find that for low screening lengths, the endohedral cavity interaction dominates over the plasma interaction such that the electron is confined within the cavity and as a consequence, the energy levels, wave-functions, dipole and generalized oscillator strengths are modified. For large screening lengths, a competence between both interactions is observed. Our results compare well to available theoretical and experimental data.

5.1 Plasma screening

The study of atoms or ions under plasma environments has been a topic of great interest over the past decades due to the coupling strength of the plasma with the electrons of immersed atoms and the consequent modification of their electronic properties [4, 35]. These properties are the subject of interest in many research areas, for example, fusion processes, laser produced plasmas, and astrophysics environments. The Coulombic screening interaction between charged particles in a plasma environment has been studied exhaustively under different treatments [73, 74]. The plasma interaction has been described by the Debye-Hückel potential [75, 74], the cosine Debye-Hückel potential [36], and recently by the Coulomb potential for finite-temperature [76, 77]. One of the electronic properties that has been studied previously is the photo-ionization cross section of atoms embedded in a plasma interaction (for a review see Janev et al. [35]). Particularly, the study of the photo-ionization of the hydrogen atom has been a topic of interest due to the appearance of several structures consequence of the plasma conditions. For example, Qi et al. [37] have studied the photo-ionization processes of the hydrogen-like ions embedded in a weakly plasma finding that the effects of the screening potential on the photo-ionization produces multiple shape and virtual-state resonances for continuum states. Furthermore, Chang et al. [38] found the same photo-ionization structure resonances but for one and two electrons processes. Another property of interest is the static dipole polarizability for several atomic systems under plasma influence [78, 140, 141, 142]. In this field, Qi et al. [78] calculate the static polarizability of the hydrogen atom embedded in a Debye-Hückel plasma by means of a numerical approach finding that the static polarizability suffers a dramatic increase when the plasma screening length decreases. These results are confirmed by the work of Das [140], where he uses a numerical integration method

to perform the calculations.

As mentioned previously, the case of an atom encaged by a fullerene molecule ($A@C_n$), as an external confinement on an atomic system is of great relevance due to many applications [14]. To describe how the electronic properties of atoms encaged in a fullerene cavity change, we use the well-known model potential approach for quantum confinement. Here, we use again the Woods-Saxon model potential [143, 81] which assumes a static fullerene electronic structure for the atoms that form the cavity and it has no discontinuities at the inner and outer radii of the fullerene, (see Section 2.5). In this chapter we combine the Debye-Hückel potential to model the screening effects in a weak plasma with the addition of an endohedral confinement in order to study the energy levels and wave functions, with a consequently change in the Dipole Oscillator Strength (DOS) and related hydrogenic electronic properties. Here, I present results for the photo-ionization cross section, the mean excitation energy, and the electronic stopping cross section.

5.1.1 Results

In this section, I present the results of the study of the $H@C_{60}$ system embedded in a Debye-Hückel plasma interaction. I show the energy spectrum and wave-function results by solving the time-independent Schrödinger equation, Section 2.4.1, by means of a finite-differences approach. Then, I calculate the DOS and GOS derived dependent electronic properties, e.g. photo-ionization [Eq. (2.24)], mean excitation energy [Eq. (2.46)], and the electronic stopping cross section [Eqs. (2.56)–(2.58)]. Here, the GOS are given by Eq. (2.57) that take into account the s-initial orbital symmetry. Note that I use the Wood-Saxon potential to describe the endohedral cavity with $R_0 = 5.8$ and $\Delta = 1.89$ a.u. [69, 63]. The numerical details were given in Section 2.8.

Energy levels

In Figs. 5.1(a-d), I show the energy levels of the hydrogen atom embedded in a Debye-Hückel plasma interaction encaged by a C_{60}. The energies of the $1s$ to $4s$ and $2p$ to $4p$ are shown as a function of screening length λ_D for several potential well depths V_0. The results for $V_0 = 0.0$ a.u. (the interaction is only through a Debye-Hückel plasma) are shown in Fig. 5.1a). From the figure, for large values of the screening length, $\lambda_D = \infty$ a.u., I obtain the well-known values of the hydrogen atom for the lowest energy levels. An interesting characteristic occurs for values of $\lambda_D < 0.84428$ a.u.. Here the $1s$ state is not bound anymore, i.e. it is delocalized in the continuum due to the strong plasma interaction. For the rest of the energy states, there is a delocalization of the excited states for different screening lengths, as observed in Fig. 5.1a) in agreement with previous findings [78, 144, 145]. In the same figure, I show the results of Kang et al. [144] ($\times$), Lumb et al. [146] ($\diamond$), and Lumb et al. [147] ($\square$), obtaining an excellent agreement when compared to the $1s$ state results (solid line).

By adding the endohedral cavity, a new and novel system is obtained. In Fig. 5.1b), I show the results for a well depth of $V_0 = 0.302$ a.u., i.e, the parameter that emulates the $H@C_{60}$ system. From the figure, one observes that the $1s$ and $2p$ states remain bound to the cage for $0.1 < \lambda_D < 1$ a.u. values with almost a constant energy, thus breaking the delocalization of the $1s$ state [see Fig. 5.1a)]. The $1s$ and $2p$ states are confined in the endohedral cage due to the weak effects of the plasma environment when one compares to the endohedral cavity [see below]. In the same figure, one observes that the $2s$ state is bound for values of the screening length larger than $\lambda_D > 1.09899$ a.u., in contrast with the results shown in Fig. 5.1a) for the same state which is bound for $\lambda_D > 3.26010$ a.u.. As one notices, higher excited states are affected by the presence of the endohedral cavity and remain bound for different values of the screening length in comparison with no endohedral cavity, as observed in Fig. 5.1b). For higher values of $\lambda_D > 1000$ a.u., the plasma screening effect on the energy levels is negligible and only the endohedral cavity potential produces an effect.

In Fig. 5.1c), we observe a significant change in the $1s$, $2s$ and $2p$ energy levels when the well depth of the endohedral cavity is increased to $V_0 = 0.7$ a.u., where the first avoiding crossing occurs. The $1s$ state is bound by the endohedral cage for all screening length values λ_D and the $2s$ state
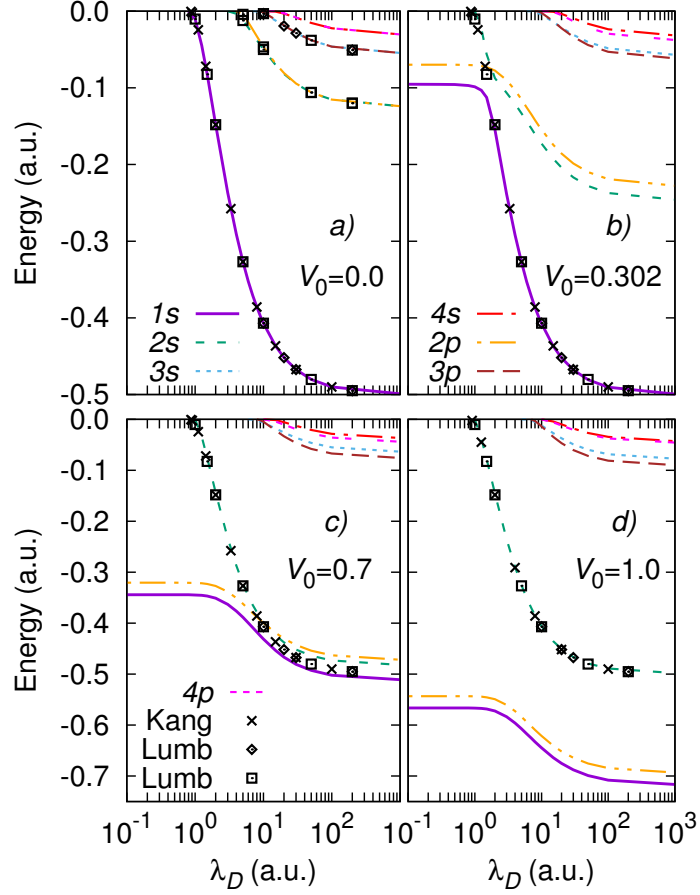
Figure 5.1: Hydrogen atom energy levels as a function of the screening length, λ_D, for the $1s$ to $4s$ and $2p$ to $4p$ states when encaged by a C_{60} cavity embedded in a Debye-Hückel plasma potential for selected well depths V_0. The well depths considered are: a) $V_0 = 0.0$, b) $V_0 = 0.302$, c) $V_0 = 0.7$, and d) $V_0 = 1.0$ a.u.. The results are compared to those of Kang et al. ($\times$) [144], Lumb et al. ($\Diamond$) [146], and Lumb et al. ($\Box$) [147] without endohedral cavity ($V_0 = 0$). See text for details.

is bound within the hydrogen atom and takes the characteristics of the unconfined $1s$ energy state without endohedral cavity for large screening length values, in agreement to Connerade findings [30] as reported in Section 4.1.1, [see Figs. 4.1 and 4.2c)]. However, the $2s$ state starts to be delocalized as the screening length is decreased. From Fig. 5.1c), we observe that the $2s$ energy level behaves as the $1s$ energy results when there is no cavity for $\lambda_D < 7$ a.u. [Fig. 5.1a)] and our results match those of Kang et al. [144]. In the same figure, we observe that the $1s$ and $2p$ energy states become constant for a screening length lower than $\lambda < 1.0$ a.u., similar to the case of $V_0 = 0.302$ a.u.. Both states are confined in the endohedral cavity due to the weakening effect of the plasma interaction in comparison to the endohedral cavity.

In Fig. 5.1d), we show the results for a well depth of $V_0 = 1.0$ a.u.. For values of the screening length $\lambda_D < 1$ a.u., the $1s$ and $2p$ states are constant and bound to the endohedral cavity. The $2s$ state is localized at the H nucleus, mimicking completely a $1s$ hydrogen state, where we observe an excellent agreement between Kang et al. [144] results for no cavity and the $2s$ energy states [see Fig. 5.1d)]. The $1s$ energy state is completely bound by the cage for large values of λ_D, due to the strong confinement effects of the endohedral potential. As the well depth is increased, the $1s$ and $2p$ energy states are modified significantly for large values of λ_D reaching $E_{2s} = -0.71761$ a.u. and $E_{2p} = -0.69407$ a.u.,

Table 5.1: Energy values for the $1s$ and $2p$ states, as well as the corresponding DOS (f_{2p}) for a hydrogen atom in an endohedral cavity embedded in a Debye-Hückel plasma for several selected values of the well depths, V_0, and plasma screening length, λ_D, as obtained with our FD approach. The results in parenthesis correspond to those reported by Lin and Ho [148].

λ_D	$V_0 = 0.0$			$V_0 = 0.302$		
	E_{1s}	E_{2p}	f_{2p}	E_{1s}	E_{2p}	f_{2p}
0.1	—	—	—	-0.09528	-0.06988	0.80914
0.3	—	—	—	-0.09540	-0.06989	0.81148
0.5	—	—	—	-0.09572	-0.06991	0.81717
0.8	—	—	—	-0.09696	-0.07014	0.83451
1.0	-0.01029	—	—	-0.09874	-0.07056	0.85312
2.0	-0.14812	—	—	-0.15468	-0.07754	0.40545
	(-0.148117)	—	—	—	—	—
3.0	-0.23683	—	—	-0.23840	-0.08992	0.18145
	(-0.236833)	—	—	—	—	—
4.0	-0.29092	—	—	-0.29181	-0.10308	0.15037
	(-0.290920)	—	—	—	—	—
5.0	-0.32681	-0.00410	0.19334	-0.32748	-0.11510	0.14303
	(-0.326809)	(-0.004102)	—	—	—	—
8.0	-0.38588	-0.03277	0.33444	-0.38635	-0.14217	0.14226
	(-0.385879)	(-0.032768)	—	—	—	—
10	-0.40706	-0.04653	0.36301	-0.40749	-0.15447	0.14380
20	-0.45182	-0.08074	0.40182	-0.45219	-0.18578	0.14779
50	-0.48030	-0.10596	0.41370	-0.48066	-0.20987	0.14962
100	-0.49008	-0.11525	0.41555	-0.49043	-0.21897	0.14994
∞	-0.49999	-0.12499	0.41619	-0.50035	-0.22865	0.15005
	$V_0 = 0.7$			$V_0 = 1.0$		
0.1	-0.34414	-0.32063	0.71632	-0.56632	-0.54331	0.69922
0.3	-0.34414	-0.32064	0.71644	-0.56632	-0.54331	0.69924
0.5	-0.34416	-0.32064	0.71671	-0.56632	-0.54331	0.69927
0.8	-0.34429	-0.32073	0.71754	-0.56639	-0.54338	0.69938
1.0	-0.34459	-0.32099	0.71838	-0.56662	-0.54359	0.69950
2.0	-0.35096	-0.32693	0.72557	-0.57232	-0.54921	0.70044
3.0	-0.36303	-0.33835	0.73564	-0.58357	-0.56037	0.70140
4.0	-0.37618	-0.35069	0.74578	-0.59581	-0.57253	0.70216
5.0	-0.38845	-0.36204	0.75295	-0.60710	-0.58376	0.70273
8.0	-0.41736	-0.38786	0.73967	-0.63281	-0.60939	0.70370
10	-0.43112	-0.39972	0.70901	-0.64465	-0.62119	0.70403
15	-0.45355	-0.41892	0.63689	-0.66382	-0.64031	0.70443
20	-0.46655	-0.43023	0.59624	-0.67511	-0.65159	0.70460
50	-0.49268	-0.45403	0.54145	-0.69890	-0.67536	0.70480
100	-0.50213	-0.46308	0.53249	-0.70795	-0.68441	0.70483
∞	-0.51193	-0.47274	0.52937	-0.71761	-0.69407	0.70485

respectively. Thus, due to the combined effects of the endohedral potential and the plasma screening, the $1s$ and $2p$ energy levels are confined within the endohedral cage with almost constant energies for low screening length and high V_0 values.

In Table 5.1, we report the values of the $1s$ and $2p$ energy states and the DOS for several well depths and selected values of the screening length, λ_D, for reference purposes. We compare our results with those given by Lin and Ho [148] for no endohedral cavity showing an excellent agreement.
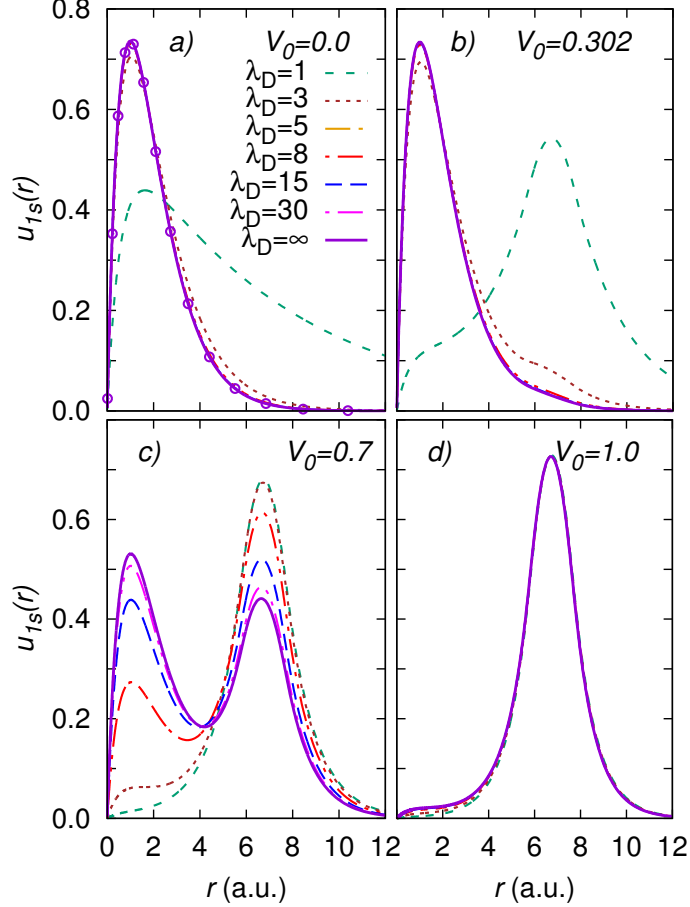
Figure 5.2: Radial wave function for the 1s-state of the H@C$_{60}$ system embedded in a Debye-Hückel plasma (color lines) for selected potential well depths: a) $V_0 = 0.0$, b) $V_0 = 0.302$, c) $V_0 = 0.7$, and d) $V_0 = 1.0$ a.u., for several screening lengths λ_D. The ($\circ$) symbols are the analytic results for the free hydrogen atom. See text for details.

Wave-functions

To understand better the energy-level results, I analyze the behavior of the wave-functions. In Fig. 5.2, I show the 1s wave-function for the H@C$_{60}$ system embedded in a Debye-Hückel interaction for several well depths, V_0, and screening length λ_D, as a function of the radial coordinate. In Fig. 5.2a) the analytic wave-function results are represented by ($\circ$) symbols for $V_0 = 0.0$ a.u. and $\lambda_D = \infty$, i.e. the free hydrogen atom results, observing an excellent agreement with our numerical findings. The plasma interaction becomes weak as λ_D decreases, then, the wave-function width is increased and the amplitude is decreased, i.e. the wave-function is becoming delocalized. For $\lambda_D < 0.84428$ a.u., the 1s electron is completely delocalized. In Fig. 5.2b), we show the case of the endohedral cavity for $V_0 = 0.302$ a.u.. Here, the wave-function starts to change for screening lengths lower than $\lambda_D = 3$ a.u. and it presents a bump around $6 < r < 8$ a.u., which is the region of the endohedral cavity. Thus, the electron becomes localized within the endohedral cavity as is observed in Figs. 5.1b) for the energy and 5.2b) for the wave-function with $\lambda_D < 3$. For a well depth of $V_0 = 0.7$ a.u., in Fig. 5.2c), near the first avoided crossing for the H@C$_{60}$ system without plasma interaction, we observe that the wave-function is shared between the hydrogen atom and the endohedral cavity and the electron becomes completely bound in the endohedral cavity region between $6 < r < 8$ a.u. for $\lambda_D < 1$ a.u.. Finally, in Fig. 5.2d), we show the results for $V_0 = 1.0$ a.u. finding that the Debye-Hückel plasma influence is almost
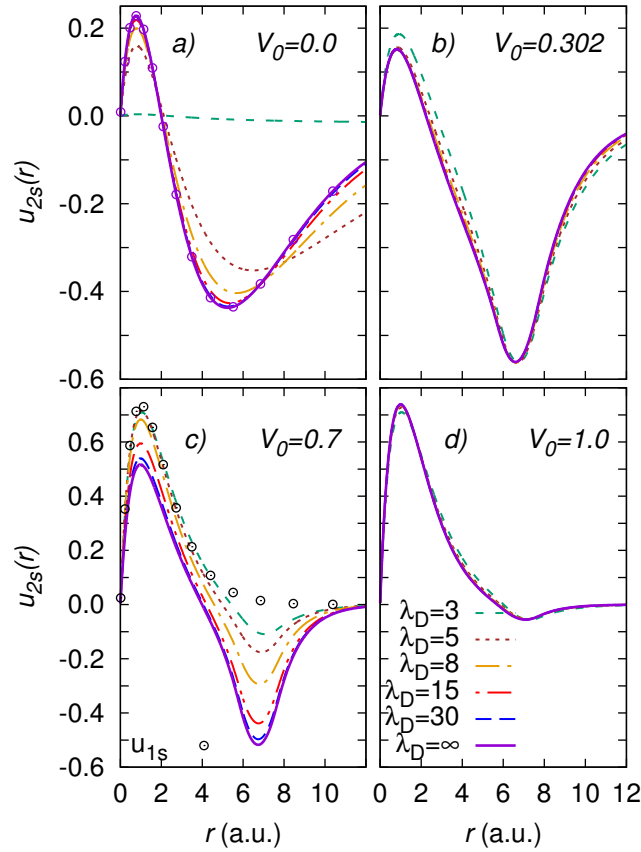
49

Figure 5.3: The same as Fig. 5.2, but for the 2s radial wave-function.

negligible on the $1s$ wave-function for all values of λ_D due to the strong effect of the endohedral cavity.

In Fig. 5.3, I show the wave-function for the $2s$-state of the H@C$_{60}$ system under a Debye-Hückel plasma. For a well depth of $V_0 = 0$ a.u. and $\lambda_D = \infty$ a.u., i.e. free hydrogen atom, we obtain an excellent agreement with the analytic results as shown in Fig. 5.3a) by (○) symbols. As the screening length is decreased, the wave-function becomes more diffuse and diminishes its amplitude until the electron becomes delocalized. In Fig. 5.3b), I show a cavity with $V_0 = 0.302$ a.u., where there is a significant change in the $2s$ wave-function in comparison with the free case shown in Fig. 5.3a). We observe that, the $2s$ wave-function shows a strong confinement within the endohedral cavity for $6 < r < 8$ a.u. with a minimal effect from the plasma interaction. In the case of a well depth with $V_0 = 0.7$ a.u., near the avoiding crossing for a pure endohedral confinement, we observe an interesting and unreported behavior for the confined electron wave-function as shown in Fig. 5.3c). In the same figure, for small λ_D, the $2s$ state is found bound to the H nuclei and resembles the $1s$ free hydrogen wave-function, as seen by the good comparison to the $1s$ wave-functions for the free case, (○) symbols. While λ_D increases, the wave-function is split partially between the C$_{60}$ cage and the hydrogen atom nuclear position due to the strong influence of the endohedral potential well as observed in Fig. 5.3c). Due to the strong influence of the endohedral potential, for $V_0 = 1.0$ a.u., in Fig. 5.3d), we observe that the influence of the Debye-Hückel plasma on the $2s$ state is negligible. Thus, the $2s$ wave-function exhibits the characteristics of the $1s$ wave function, as observed in Fig. 5.2a).

In Fig. 5.4, I show the $2p$ wave-function of the H@C$_{60}$ system in a Debye-Hückel plasma. For a well depth of $V_0 = 0$ a.u. and $\lambda_D = \infty$ a.u. (free hydrogen atom), in Fig. 5.4a), I find an excellent agreement between our numerical results and the analytic results shown by (○) symbols. Similar to the $1s$ wave-function, I find that as λ_D decreases, the $2p$ wave-function becomes more delocalized.
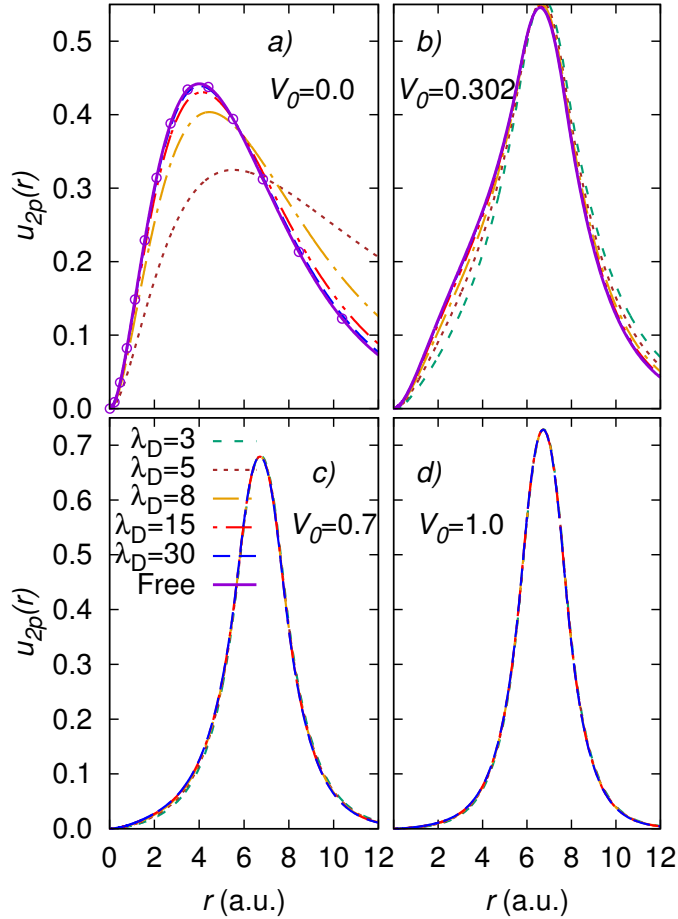
Figure 5.4: (Color on-line). The same as in Fig. 5.2, but for the 2*p* radial wave-function.

When the endohedral cavity is present with $V_0 = 0.302$ a.u., Fig. 5.4b) shows that the wave-function is confined within the endohedral cage and the screening length has a minimal effect in the 2*p* state. In Figs. 5.4c) and 5.4d) I show the wave-function for well depths with $V_0 = 0.7$ and $V_0 = 1.0$ a.u., respectively, finding that the effect of the Debye-Hückel plasma environment on the 2*p* wave-function is negligible and is completely dominated by the endohedral cavity.

One partially concludes that the electron is localized in different regions of the cavity depending of the strength of the Debye-Hückel potential or the endohedral cavity well depth. In consequence, the electronic properties will be different due to the competition between both interactions.

Dipole oscillator strength

With the eigenvalues and eigenfunctions calculated in the last section, we proceed to obtain the dipole oscillator strength of the H@C$_{60}$ under a plasma confinement. In Fig. 5.5, we show the DOS for the $1s \rightarrow 2p$ transition, f_{2p}, for several well depths V_0, as a function of the screening length λ_D. In the same figure, we compare with the Debye-Hückel results of Saha et al. [145] ($\triangle$) for no cavity, Qi et al. [78] ($\square$), Kang et al. [144] ($\times$), and and Lumb et al. [146] ($\diamond$) where there is an excellent agreement with our numerical results (solid line). For results with no cavity and for $\lambda_D = \infty$ a.u., we recover the well-known free hydrogen atom value of $f_{1s \rightarrow 2p} = 0.41619$. As the screening length decreases, the f_{2p} decreases until $\lambda_D = 4.54257$ a.u., where there is no anymore a bound $f_{1s \rightarrow 2p}$ transition, here the 2*p* state becomes delocalized. In the case of a well depth of $V_0 = 0.302$ a.u., when the endohedral cavity
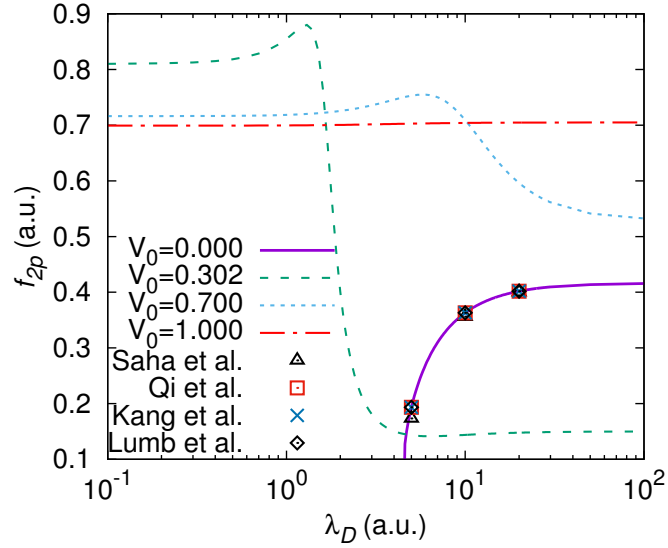
Figure 5.5: Dipole oscillator strengths for the $1s \rightarrow 2p$ transition, f_{2p}, of the endohedral H atom encaged by a C_{60} in a Debye-Hückel plasma potential for selected well depths V_0, as a function the screening length λ_D. The ($\triangle$) symbols are from Saha et al. [145], the ($\square$) symbols are from Qi et al. [78], the ($\times$) symbols are from Kang et al. [144], and the ($\diamond$) are from Lumb et al. [146] for the case of no cavity ($V_0 = 0$). See text for details.

is present, we observe a significant change in the $1s \rightarrow 2p$ transition for large screening lengths where the f_{2p} takes a value of 0.15 and increases for $1 < \lambda_D < 3$ a.u., reaching a value of $f_{1s \rightarrow 2p} = 0.81$ for $\lambda_D < 1$ a.u., as one observes from Fig. 5.5. The constant value is explained by the behavior exhibited by the $1s$ and $2p$ energy levels (Fig. 5.1) and wave-functions (Figs 5.2 and 5.4) for $\lambda_D < 1$ a.u.. For a well depth of $V_0 = 0.7$ a.u., one observes a similar but less prominent behavior as in the previous case. For $\lambda_D < 1.5$ a.u., we obtain an average value of $f_{1s \rightarrow 2p} = 0.71$ which is consequence of the confinement of the $1s$ and $2p$ states in the endohedral cavity by the potential well and strong plasma interactions. The largest change in the f_{2p} is given for screening lengths between $5 < \lambda_D < 30$ a.u. where the influence of the plasma decreases and the endohedral potential becomes stronger. The abrupt change is consequence of the $1s$ wave-function being partially confined in the C_{60} and the $2p$ is completely confined in the endohedral region [see Figs. 5.1c), 5.2c), and 5.4c)]. In Fig. 5.5, for a well depth of $V_0 = 1$ a.u., the f_{2p} is almost constant for all the screening lengths between $0.1 < \lambda_D < \infty$ a.u. with a value of around 0.7. For this case, the wave-functions for the $1s$ and $2p$ states are completely bound by the cage, where the lower states are confined in the fullerene cavity, as observed in Figs. 5.2d) and 5.4d). Thus, the effect of the plasma is to weaken the $1s \rightarrow 2p$ transition as λ_D decreases. When we add the endohedral cavity the transition emission becomes stronger as λ_D decreases.

Photo-ionization cross section

The first DOS derived property result obtained in this work is the photo-ionization cross section (PCS) shown in Figs. 5.6(a-d), for the H@C_{60} system embedded in a Debye-Hückel plasma for selected well depths V_0 and screening lengths λ_D as a function of the photo-electron energy. In the figure, we show the results for well depths $V_0 = 0.0$, 0.302, 0.7, and 1 a.u., as well as for values of the screening length λ_D 3, 5, 8, 15, 30, and ∞ a.u.. In Fig. 5.6a), we show the case for no endohedral cavity ($V_0 = 0$ a.u.) by solid line, where we observe an increase of the PCS as the screening length is decreased for low-to-intermediate photo-electron energy. In the same figure, we observe the appearance of resonant structures as λ_D decreases until the $2p$ state becomes unbound [78]. It resembles the well-known
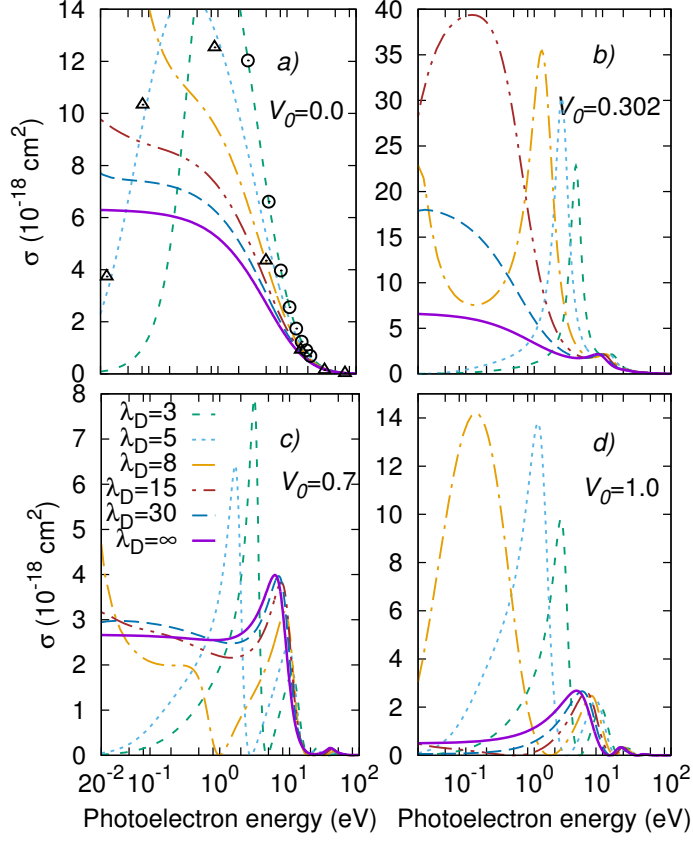
Figure 5.6: Photo-ionization cross section for the H@C_{60} system embedded in a Debye-Hückel plasma environment for selected well depths V_0 and for several screening lengths, λ_D, as a function of the photo-electron energy. The ($\circ$) symbols are the theoretical results of Lin and Ho [148] for $\lambda_D = 3$ a.u. and the ($\triangle$) symbols are the theoretical results of Qi et al. [37] for $\lambda_D = 5$ a.u.. See text for details.

analytic result of Bethe [34] for $\lambda_D = \infty$ a.u.. The ($\circ$) symbols are the results given by Lin and Ho [148] for $\lambda_D = 3$ a.u. and the ($\triangle$) symbols are the theoretical results of Qi et al. [37] for $\lambda_D = 5$ a.u for a pure hydrogen plasma ($V_0 = 0$ no cavity) finding an excellent agreement with our results. In Figs. 5.6(b-d), for a given screening length, we observe the appearance of multiple structures in the PCS when the endohedral cavity is present. These structures are confinement resonances, known as Cooper resonances that occur due to constructive interference of the photo-electron waves scattered-off by the C_{60} cage and the outgoing photo-electron wave [149]. We find that the Cooper resonances are sensitive on the screening length and on the endohedral cavity well depth, as observed in Figs. 5.6(b-d). In Fig. 5.6b), for $V_0 = 0.302$ a.u., we observe the increase of the PCS for large values of λ_D for a given photo-electron energy and the emergence of Cooper resonances. Furthermore, the resonance position moves towards high photo-ionization energies as λ_D is decreased. From Fig. 5.6c), for $V_0 = 0.7$ a.u., the Cooper resonances decrease and are shifted to larger values of photo-electron energies as the screening length is increased. In Fig. 5.6d), we show the results for $V_0 = 1.0$ a.u., were the PCS curve increases for low values of screening length. The latter effect is due to the combined effects of the plasma and the cavity. When the C_{60} is present, we observe that the Cooper resonances decrease and shift towards low values of photo-electron energy as the plasma screening length is increased. As one observes, the PCS of a H atom is modified drastically due to the endohedral cavity and the plasma screening.
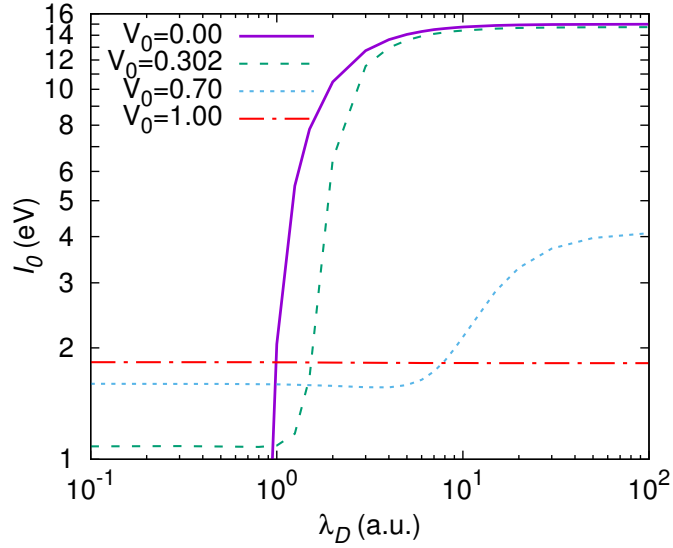
Figure 5.7: Mean excitation energy, I_0, for a H@C$_{60}$ confinement system in a Debye-Hückel plasma as a function of screening length, λ_D, for several well depths V_0.

Mean excitation energy

The second DOS derived property is the mean excitation energy, I_0, shown in Fig. 5.7, as a function of the screening length λ_D for several well depths V_0. For no endohedral cavity ($V_0 = 0$ a.u.) and for large values of $\lambda_D = \infty$ a.u., we obtain the free hydrogen result of $I_0 = 14.993$ eV in agreement with the results of Cabrera-Trujillo and Cruz [150]. As the plasma interaction decreases (diminishing of λ_D), the mean excitation energy decreases from $I_0 = 14.73608$ eV at $\lambda_D = 10$ a.u. to $I_0 = 2.04646$ eV at $\lambda_D = 1$ a.u.. For lower values of $\lambda_D < 0.84428$, the $1s$ is delocalized and there is no more meaning for I_0 as we observe from the figure. When one considers the cavity with $V_0 = 0.302$ a.u. (that emulates the H@C$_{60}$ system), one observes a constant value of $I_0 = 1.08$ eV for $\lambda_D < 1$ a.u.. As observed from the figure, the abrupt change is given for $1 < \lambda_D < 10$ a.u. where the confinement effects of the H@C$_{60}$ are more relevant that the weak plasma interaction for large λ_D. This sudden change is consequence of the transition from a strong plasma interaction to a weak plasma influence. For a well depth of $V_0 = 0.7$ a.u., the mean excitation energy is constant around $I_0 = 1.59$ eV for values of screening length lower than $\lambda_D < 1.25$ a.u.. In this case, we have that the $1s$ and $2p$ states are partially and completely confined, respectively, in the endohedral cage [see Figs. (5.2) and (5.4)]. When the screening influence becomes weak (low λ_D values), the $1s$ and $2p$ energy levels are confined completely by the endohedral cage and we observe a constant value for the mean excitation energy. For no plasma interaction, at $\lambda_D = \infty$ a.u., we find a value of $I_0 = 4.12728$ eV. As a consequence of the DOS behavior, for $V_0 = 1$ a.u., the mean excitation energy is almost constant with a value of $I_0 = 1.830169$ a.u. at $\lambda_D = 0.1$ a.u. and $I_0 = 1.81943$ a.u. at $\lambda_D = \infty$ a.u.. The almost constant value of I_0 is attributed to the fact that the electron is strongly confined by the endohedral cavity [see Figs. (5.2) and (5.4)] with a minimal influence from the plasma interaction. An immediate consequence for low λ_D values, is that the electronic stopping cross section will increase for high collision energies.

Generalized oscillator strength

In Fig. 5.8, I show the GOS results for the $1s \rightarrow 2s$, F_{2s}, transition as a function of the transferred momentum, q, for several well depths and selected screening lengths. The ($\circ$) symbols are the analytic GOS results for the free hydrogen atom [54, 32] (i.e. $V_0 = 0$ and $\lambda_D \rightarrow \infty$ a.u.) showing an excellent
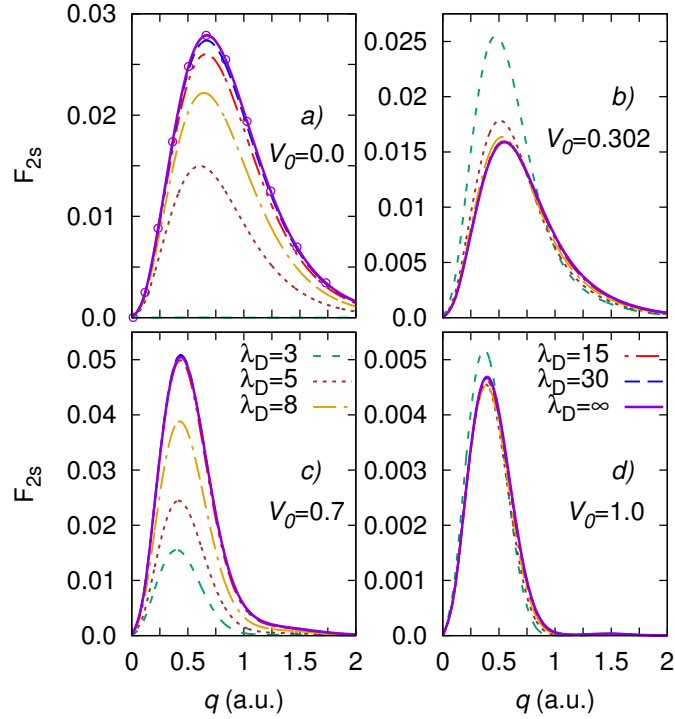
Figure 5.8: Generalized oscillator strength for the $1s \rightarrow 2s$ transition, $F_{2s}(q)$, for atomic hydrogen confined by an endohedral cavity embedded in a Debye-Hückel plasma, as a function of the momentum transfer, q, for several well depths V_0 and screening lengths λ_D. We show the results for well depths: a) $V_0 = 0.0$, b) 0.302, c) 0.7, and d) 1.0 a.u. and selected screening lengths $\lambda_D = 3, 5, 8, 15, 30$, and ∞ a.u.. The ($\circ$) symbols are the analytic results for the free hydrogen atom.

agreement with our numerical calculation. In Fig. 5.8a), one observes a decrease of the F_{2s} curve when the screening length is reduced, for $V_0 = 0.0$ a.u.. From the figure, there is no F_{2s} contribution for screening lengths lower than $\lambda_D = 3.2601$ a.u., because of the delocalization of the $2s$ level, as reported in Fig. 5.1a). For $\lambda_D > 15$ a.u., the curve is similar to the free case, i.e. there is a weak plasma influence on the hydrogen atom that modifies slightly the GOS. In Fig. 5.8b), when the cavity is present with $V_0 = 0.302$ a.u., the effect of the plasma interaction is to increase F_{2s} as the plasma screening length decreases, contrary to the absence of the cage ($V_0 = 0$ a.u.). For a well depth of $V_0 = 0.7$ a.u., corresponding to the first avoided crossing of the pure endohedral hydrogen atom, the F_{2s} decreases smoothly with the decrease of the screening length. However, in this case, there exist a contribution for a screening length of $\lambda_D = 3$ a.u. contrary to the results for $V_0 = 0$ a.u.. Fig. 5.8d) shows the results for $V_0 = 1.0$ a.u., where the F_{2s} increases as the plasma screening length decreases. Here, the $1s$ and $2s$ energy levels are confined in the endohedral cavity.

In Fig. 5.9, I show the GOS for the $1s \rightarrow 3s$, F_{3s}, transition for selected potential well depths and screening lengths as a function of q. In Fig. 5.9a), I show the F_{3s} results for a well depth of $V_0 = 0.0$ a.u., as the $3s$-excited state becomes delocalized [see Fig. 5.1a)], observing that there is no contribution to the GOS for $\lambda_D < 8$ a.u.. For larger values of $\lambda_D > 8$ a.u., the F_{3s} curve increases softly until reaching the value of the free case. The ($\circ$) symbols are the analytic results for the free hydrogen atom [54] in excellent agreement with our numerical calculations. In Fig. 5.9b), I show the effects of the plasma in the presence of an endohedral cavity with $V_0 = 0.302$ a.u., observing an increase of F_{3s} for $\lambda_D > 7$ a.u.. In Fig. 5.9c), one observes the appearance of a minimum around $q = 0.5$ a.u., for $V_0 = 0.7$ a.u.. The F_{3s} intensity is reduced as the screening length is decreased, observing a slightly contribution for $\lambda_D = 6$ a.u. as a consequence of the $3s$-state starts to be delocalized. When the well
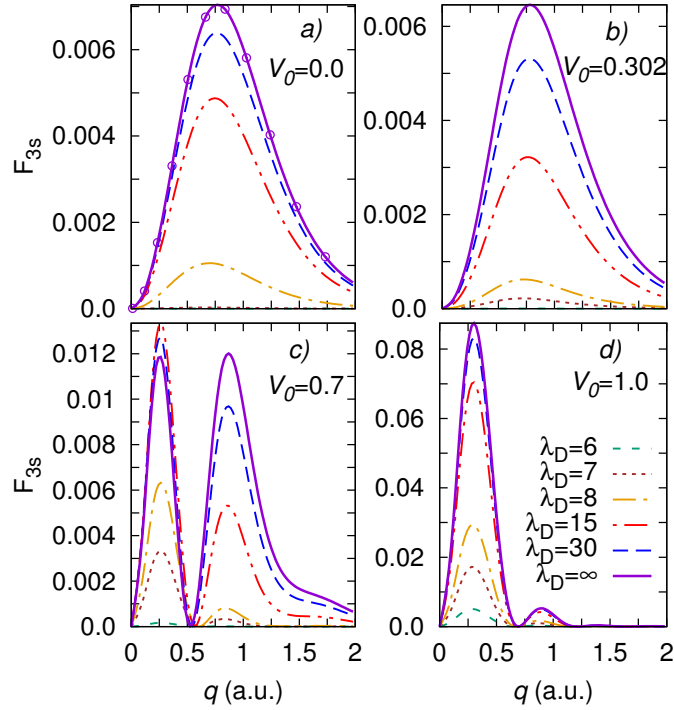
Figure 5.9: (Color on-line). The same as in Fig. 5.8, but for the $1s \to 3s$ transition, $F_{3s}(q)$.

depth is increased to $V_0 = 1.0$ a.u., we observe, in Fig. 5.9d), that the second maximum has decreased in intensity, where this transition has a large intensity as the endohedral cavity deepens. Once again, the F_{3s} curve decreases as the plasma screening length is decreased.

In Fig. 5.10, I show the GOS for the $1s \to 2p$, F_{2p}, transition for selected potential well depths and screening lengths as a function of transferred momentum q. In Fig. 5.10a), for $V_0 = 0.0$ a.u., one observes a smooth decrease of the F_{2p} curve as the screening length is decreased, observing that F_{2p} is negligible for $\lambda_D < 4.54257$ a.u. due to the delocalization of the $2p$ state. Once again, the (○) symbols are the analytic results for the free hydrogen atom [54] in excellent agreement with our numerical calculations. The (■) symbol at $q = 0$ for F_{2p} and $V_0 = 0$ a.u. corresponds to the free H atom case at $f_{2p} = 0.4161$. When the well depth is increased to $V_0 = 0.302$ a.u., there is a small effect of the plasma interaction in comparison with the free case. Furthermore, we observe a notorious amplitude decrease of the F_{2p} intensity as compared to the free hydrogen case due to the fact that the $2p$ state is almost confined by the endohedral potential, independently of the screening length. In Fig. 5.10c), F_{2p} increases slightly as the screening length decreases. In Fig. 5.10d), we observe that the plasma influence on the F_{2p} is negligible and the F_{2p} intensity remains the same for all values of the screening length. This is due to the fact that the electron is strongly bound in the cavity region and the plasma screening environment effects are negligible. However, the intensity line is stronger than in the previous free case ($V_0 = 0$ a.u.).

In Fig. 5.11, I show the GOS for the $1s \to 3p$ transition, F_{3p}, for selected potential well depths and screening lengths as a function of the transferred momentum q. In Fig. 5.11a) ($V_0 = 0$ a.u.), one observes a decrease of the F_{3p} intensity as the plasma screening length is decreased. Notice that F_{3p} becomes null for screening length $\lambda_D = 8$ a.u.. The latter is attributed to the delocalization of the $3p$ energy level for values lower than $\lambda_D < 8.84610$ a.u.. As before, the (○) symbols are the analytic results for the free case. In Fig. 5.11b), for a well depth of $V_0 = 0.302$ a.u., one observes a significant increase of the F_{3p} curve by a factor of 3 in comparison with Fig. 5.11a). In Fig. 5.11c), near the first avoided crossing of a H atom for a pure endohedral cavity, one observes a maximum at around $q = 0.5$

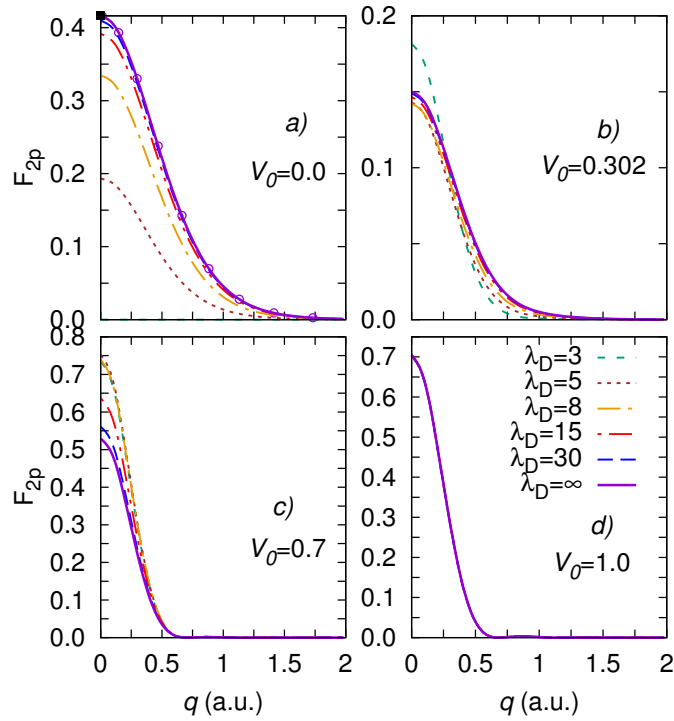**Figure 5.10:** The same as in Fig. 5.8, but for the $F_{2p}(q)$ transition. The (■) symbol is the result for a free hydrogen atom at $q = 0$ a.u. ($f_{2p} = 0.4161$).
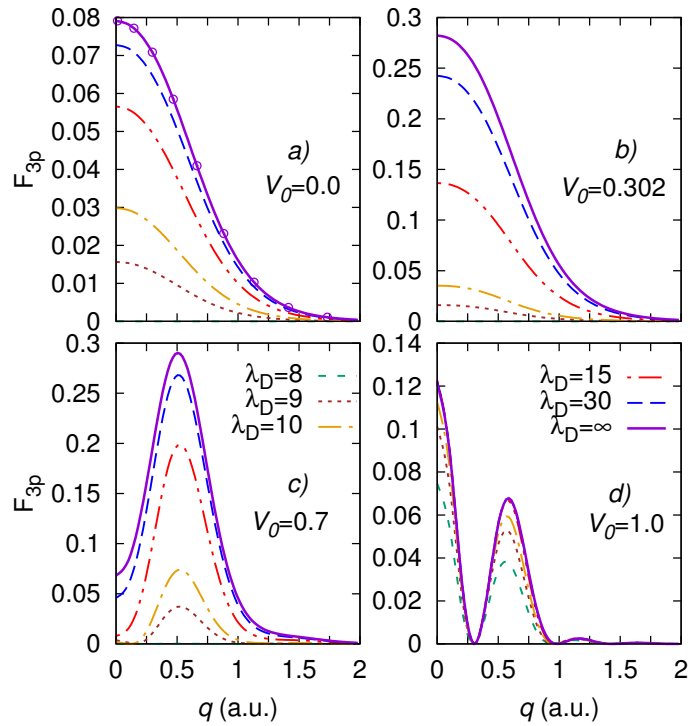

Figure 5.11: The same as in Fig. 5.8, but for the $F_{3p}(q)$ transition.
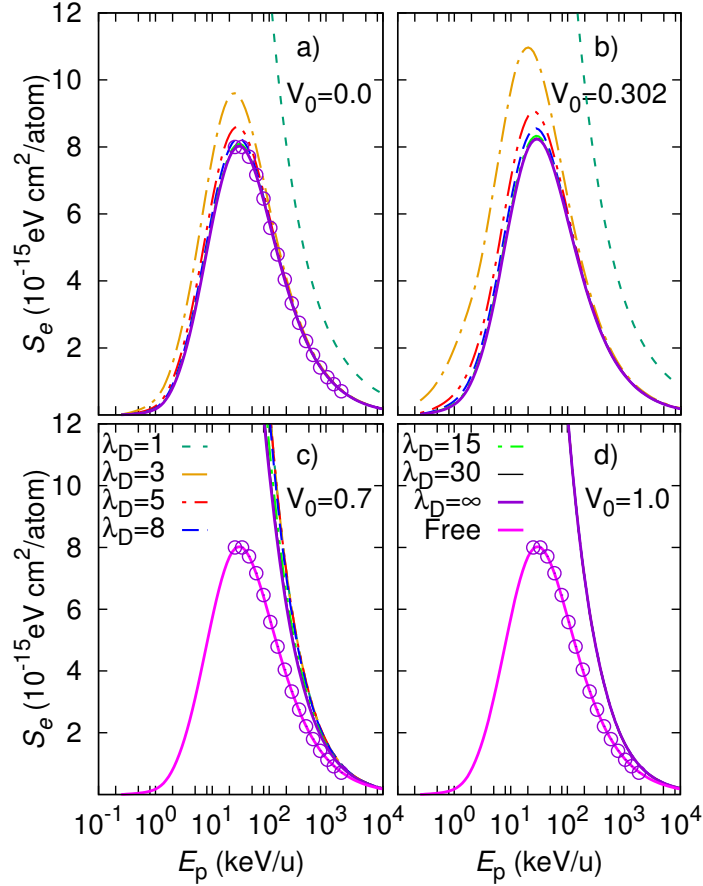
Figure 5.12: Electronic stopping cross section for protons colliding with atomic hydrogen encaged by an endohedral cavity and embedded in Debye-Hückel plasma as a function of the projectile initial kinetic energy for several selected confinement well depths V_0 and plasma screening lengths λ_D. In a) $V_0 = 0.0$, b) $V_0 = 0.302$, c) $V_0 = 0.7$, and d) $V_0 = 1.0$ a.u.. The ($\circ$) symbols are the free atomic hydrogen theoretical results of Bichsel [139].

a.u.. The F_{3p} curve decreases for the decrease of the screening length. In Fig. 5.11d), one observes the appearance of an oscillatory behavior in the F_{3p} curve as a function of q. The influence of the Debye-Hückel plasma on the endohedral H atom is negligible for screening lengths $\lambda_D > 10$ a.u..

Consequently, the GOS distributions are modified by the presence of the plasma environment producing a decrease of the F_{ns} curves as the screening length decreased meanwhile the F_{np} increases. This effect will be relevant in the behavior of the electronic stopping cross-section and GOS dependent properties.

Electronic stopping cross section

In Fig. 5.12, I show the electronic stopping cross section (SCS) for protons colliding with atomic hydrogen encaged by an endohedral cavity and embedded in a Debye-Hückel plasma. In this case the assumption in the model is that the projectile momentum transfer goes only into the active electron in the hydrogen target and not into the endohedral cavity (static model potential).

In Fig. 5.12a), I show the results for $V_0 = 0.0$ a.u. where the hydrogen atom is subjected only to the Debye-Hückel plasma interaction. In the low-to-intermediate energy collision, the largest effect of the plasma environment occurs as well as for small screening length values. As the plasma

interaction is decreased, the energy deposited by the ions into the hydrogen system increases slightly. For high collision energy, the plasma interaction affects the SCS for values of $\lambda_D < 3$ a.u.. This is because for low values of the screening length the bound states are near the delocalization threshold meaning a higher absorption of the projectile energy. I compare the results to those of a free hydrogen as reported by Bichsel [151] based in the same first Born approximation [($\circ$) symbols] observing an excellent agreement to the free case results, $V_0 = 0.0$ a.u. and $\lambda_D \to \infty$ (solid line). In Fig. 5.12b), I show the results for $V_0 = 0.302$ a.u., for $\lambda_D < 3$ a.u. where one observes a significant change in the SCS for low-to-intermediate collision energy. In Fig. 5.12c), I show the results for $V_0 = 0.7$ a.u. (a well depth near the first avoided crossing for a H atom confined by an endohedral cavity without plasma interaction) observing an increase of the SCS for $\lambda_D \to \infty$ (solid line) in comparison with the previous results of Figs. 5.12(a-b) for intermediate-to-high projectile energies. I show the free case result (solid thin line) in Figs. 5.12(c-d) for comparison purposes. From Fig. 5.12c), we observe a slight effect of the plasma interaction on the H atom stopping cross section for all projectile energies. In Fig. 5.12d), we show the results for $V_0 = 1.0$ a.u., where one observes that the effect of the plasma influence on the electronic SCS is negligible. As the endohedral cavity potential well increases, more bound states appear below the delocalization threshold with the dominant transition becoming the $1s \to 2p$. Thus, the stronger effect of the plasma is for shallow cavities, in contrast, for deep cavities, the effect of the plasma is negligible with a predominant contribution only from the endohedral cavity.

5.2   Conclusions and perspectives

In this chapter, I have reported the effects of spatial confinement by a fullerene cavity on a hydrogen atom with a plasma interaction on properties dependent on the dipole and generalized oscillator strength. I have used the Wood-Saxon model potential to describe the electronic static behavior of the endohedral cage as a function of the well depth V_0. The plasma interaction is described by the Debye-Hückel screening potential. It is found that the energy levels and wave-functions are modified drastically under the plasma interaction. With the increase of the endohedral well depth and the decrease of the plasma screening length, the electron in the hydrogen atom is bound into the cavity region. Particularly, this effect is reflected in the delocalization of the $1s$ and $2p$ energy levels for screening lengths lower than $\lambda_D < 1$ a.u., for low values of V_0. Consequently, the DOSs and GOSs are modified due to the screening of the plasma potential. I find the appearance of new structures in the photo-ionization cross section, as well as a drastic change on the static dipole polarizability and mean excitation energy due to the change in the energy levels as a function of the screening length. Furthermore, for large values of the endohedral well depth, the effects of the plasma interaction on physical properties is negligible. Thus, I find a strong competition between the effects of the plasma interaction and those of the static endohedral cavity which modify accordingly the electronic properties of the system.

From the results, it would be interesting to implement a temperature-dependent model to describe the plasma environment and obtain the DOS and GOS derived electronic dependent properties. Finally, the study reported here could be extended to multi-electronic systems.

In the following chapter, I present the result obtain for the lithium atom encaged by a fullerene molecule considering the Hartree-Fock approach.

6

Lithium atom at extreme conditions

In this chapter, I study the dipole oscillator strength dependent properties of a lithium atom encaged by a fullerene molecule Li@C$_{60}$ by solving the Restricted and Unrestricted Hartree-Fock equations within the Slater's X$-\alpha$ approach by means of a Gauss-Seidel iterative method and a finite-differences approach. This chapter is based on the research **Paper V** that is in preparation. I use the Woods-Saxon potential to describe the endohedral confinement due to the relevance of the smoothness at the cavity edges. The dipole dependent electronic properties reported are the photo-ionization cross section (PCS) and the mean excitation energy. The content of this chapter is reported in **Paper V** under preparation for submission.

6.1   Endohedral confinement

Photo-ionization of multi-electronic systems encapsulated inside an endohedral cage has received much attention in recent years due to the change of their spatial confinement properties. In the case of the Li@C$_{60}$ system, I use the quantum confinement model potential, as discussed in Section 2.5, to describe the C$_{60}$ fullerene molecule. In this work, I use the Wood-Saxon potential to describe the C$_n$ cavity.

To describe the electronic structure and interactions of the multi-electronic atom inside the C$_{60}$ cage, different theoretical approaches have been developed. One approach is to considered a pseudo-potential that describes the inner or frozen electronic structure of the atom. The pseudo-potential has been applied to different problems in atomic physics with successful results [42, 43, 152, 44, 153]. The basic idea of pseudo-potentials is to take into account the multi-electronic core interaction with the single valence electron by a modification of the Coulomb potential.

The Restricted and Unrestricted Hartree-Fock (RHF and UHF, respectively) approaches have been previously used to describe the electronic properties of the lithium atom without confinement environment, e.g. [154, 155, 156, 157, 158]. For the Li atom encaged by a fullerene molecule, several theoretical approximations have been implemented to study the photo-ionization process, e.g. [159, 160, 161, 162, 163, 164, 165, 166]. For example, Li and Ho [26, 164] use a psuedo-potential for the lithium atom to simulate the core interaction with the single valence electron with optimized parameters. Here, Li and Ho calculate the PCS of the 2s shell under a confinement given by a power exponential potential, finding the emergence of multiple Copper resonances due to the endohedral confinement. In a recent, paper Hasoğlu et al. [31] studied the correlation energies of the ground state of alkali-earth-metal atoms for an endohedral system A@C$_{60}$ through a multiconfiguration Hartree-Fock method. Hasoğlu et al. do not consider the specific case of photo-ionization problem, however they found that the valence electrons diffuse outward in the presence of the confining potential as a function of the well depth, as consequence the electrons to be further apart and the correlation energy decreases. With the increase of well depth, the valence electrons become trapped in the confining well and, as a consequence, the correlation energy increases.

In this chapter, I analyze the endohedral lithium atom using the Wood-Saxon model potential to describe the endohedral cavity in order to study the energy levels and wave functions, with a consequently change in the Dipole Oscillator Strength (DOS) and related electronic properties.
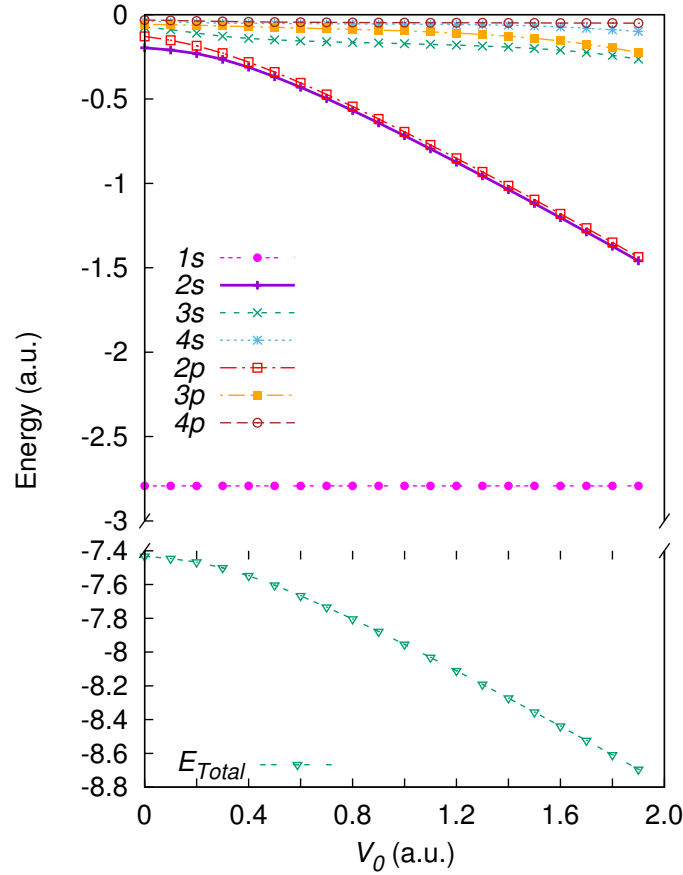
Figure 6.1: Lithium atom energy levels for the $1s$ to $4s$, $2p$ to $4p$, and the total energy E_{Total} encaged by an endohedral cavity as a function of the potential well depth V_0. The symbol lines are the results for the RHF approach. See text for discussion.

6.1.1 Results

In this chapter, I show the energy levels and wave-functions results by implementing the Gauss-Seidel method and a finite-differences approach to solved the time-independent Schrödinger equation (see Section 2.4.2). Then, I calculate the dipole oscillator strength (DOS) derived dependent electronic properties e.g. photo-ionization [Eq. (2.24)] and mean excitation energy [Eq. (2.46)], within the RHF and UHF approaches. Note that I use the Wood-Saxon potential to describe the endohedral cavity with $R_0 = 5.8$ and $\Delta = 1.89$ a.u. [69, 63]. The numerical implementation as given in Section 2.8.

Energy levels and wave-functions

In Fig. 6.1, I show the energy levels for the ground state of the endohedral lithium atom as obtained by the RHF case. The energies of the $1s$ to $4s$, $2p$ to $4p$, and the total energy are shown as a function of the well depth V_0. Within the Slater's X-α approach, I report an α parameter value of 0.26. From the figure, for a well depth of $V_0 = 0.0$ a.u. (no endohedral cavity), I find that the energy levels are $E_{1s} = -2.79231$, $E_{2s} = -0.19639$, $E_{2p} = -0.12866$ a.u., for the ground and excited states, respectively, and the total energy is $E_{Total} = -7.43268$ a.u., in excellent agreement with well known result [167, 168]. In Fig. 6.1, one observes that the $1s$ energy level is not affected by the endohedal
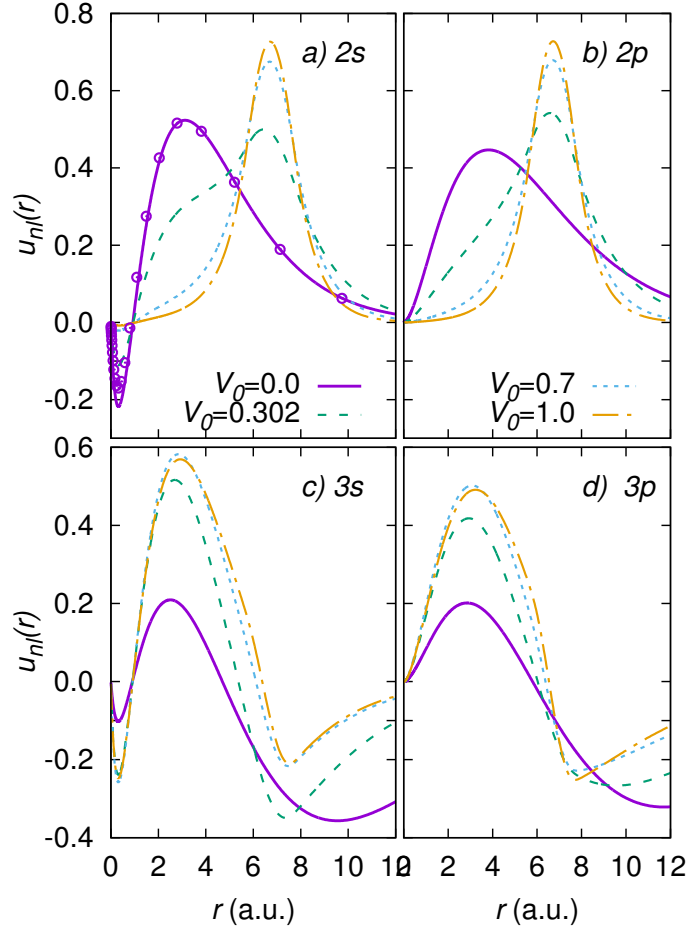
Figure 6.2: Radial wave-functions for the $2s$, $3s$, $2p$ and $3p$ states of the Lithium atom in an endohedral cavity for selected potential well depths V_0 in the RHF case. The ($\circ$) symbols are the theoretical results from Ref. [167]. See text for discussion.

cavity and remains constant for all well depths V_0, as we expect, due to we are considering a frozen core by means of the RHF approach. As the well depth V_0 becomes deeper, the valence energy level migrates from being in the atom to being in the endohedral cage as one observes from Figs. 6.1 and 6.2 (see below). This behavior would be relevant in the determination of the DOS derived properties described in the following sections.

In Figs. 6.2(a-d), I show the eigenfunctions for the $2s$, $3s$, $2p$ and $3p$ states of the Lithium atom in an endohedral cavity for selected potential well depths V_0 in the RHF case. For the case of the free atom, $V_0 = 0.0$ a.u., one observes a good agreement of the results in comparison with the Hartree-Fock solutions shown by ($\circ$) symbols from Ref. [167]. When the endohedral cavity is added, for a well depth of $V_0 = 0.302$ a.u., one observes, in Figs. 6.2(a-d), that the $2s$, $2p$, $3s$, and $3p$ wave-functions are modified significantly in comparison with the unconfined results for $V_0 = 0$ a.u.. Here, it is evident from Figs. 6.2(a-b) that the $2s$ and $2p$ wave-functions are shifted to the endohedral region, however, for $3s$ and $3p$ wave-functions there is a competition between the Coulomb and well depth attraction. For a well depth of $V_0 = 0.7$ a.u., one observes, in Figs. 6.2(a-b), that the $2s$ and $2p$ wave-functions are almost confined in the cage region between $6 < r < 8$ a.u.. For the same well depth, the $3s$ [Fig. 6.2c)] and $3p$ [Fig. 6.2d)] wave-functions are split partially between the C_{60} cage region and the lithium atom nuclear position. When the well depth is increased to $V_0 = 1$ a.u., from Figs. 6.2a) and 6.2b), the $1s$ and $2p$ wave-functions are bound in the cavity region with no contribution at the
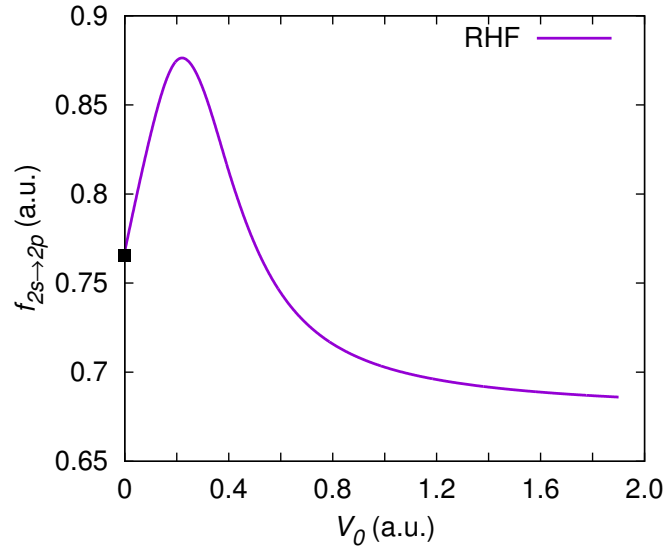
Figure 6.3: Dipole oscillator strength for the transition $2s \rightarrow 2p$ of the Li atom encaged by an endohedral cavity for selected well depths V_0 for the RHF case. The (■) symbol corresponds to the free value ($V_0 = 0$ a.u.), $f_{2s \rightarrow 2p} = 0.76789$ a.u., in good agreement with previously reported values [156, 167]. See text for discussion.

hydrogen atom position. For this well depth, the valence electron is completely bound by the cage. As one observes from Figs. 6.2(c-d), the increase of the well depth makes slight changes to the $3s$ and $3p$ wave-functions. From Fig. 6.1, we note that the $1s$ energy state is not altered by the presence of the endohedral cavity being only the valence state the affected one. Thus, the $1s$ wave-function is not modified by the presence of the endohedral cavity. The increase of the well depth produces a trapping of the valence electrons within the endohedral cavity.

Dipole oscillator strength

From the calculated eigenvalues and eigenfunctions, I proceed to obtain the DOS for the Li@C$_{60}$ system. In Fig. 6.3, I show the $2s \rightarrow 2p$ transition as a function of the well depth V_0. The (■) symbol corresponds to the free result, $f_{2s \rightarrow 2p} = 0.76789$ in good agreement with $f_{2s \rightarrow 2p} = 0.76568$ from Ref. [167] and $f_{2s \rightarrow 2p} = 0.76710$ from Ref. [156]. From the figure, as the well depth is increased, the DOS is increased too, where the significantly change is for $V_0 = 0.2$ a.u., reaching a value of $f_{2s \rightarrow 2p} = 0.87491$. Then, the DOS decays smoothly until $f_{2s \rightarrow 2p} = 0.68603$ for $V_0 = 2.0$ a.u.. This behavior is related to the change of the $2s$ [Fig. 6.2a)], $2p$ eigenfunctions [Fig. 6.2b)], and energy levels [Fig. 6.1]. As the potential well depth is increased, the eigenfunction is between being in the lithium atom and then localized in the endohedral cavity. A comparison must be made with the endohedral hydrogen atom results presented in Chapter 4. From the endohedral hydrogenic results, we observed the decreased of the DOS as the well depth is increased reaching a minimum and then an increase followed by a constant value. In comparison, the Li@C$_{60}$ presents a maximum and then a decrease of the DOS.

Photo-ionization cross section

The photo-ionization cross section is calculated for the $2s$ shell of the endohedral lithium atom for several well depths and as a function of the photo-electron energy in the RHF approach. In Fig. 6.4a), I show the results of the PCS for the free case (color solid line), i.e. no endohedral cavity ($V_0 = 0$ a.u.). In the same figure, I compare with the theoretical results of Peach (red solid line) [163], Lin and Ho
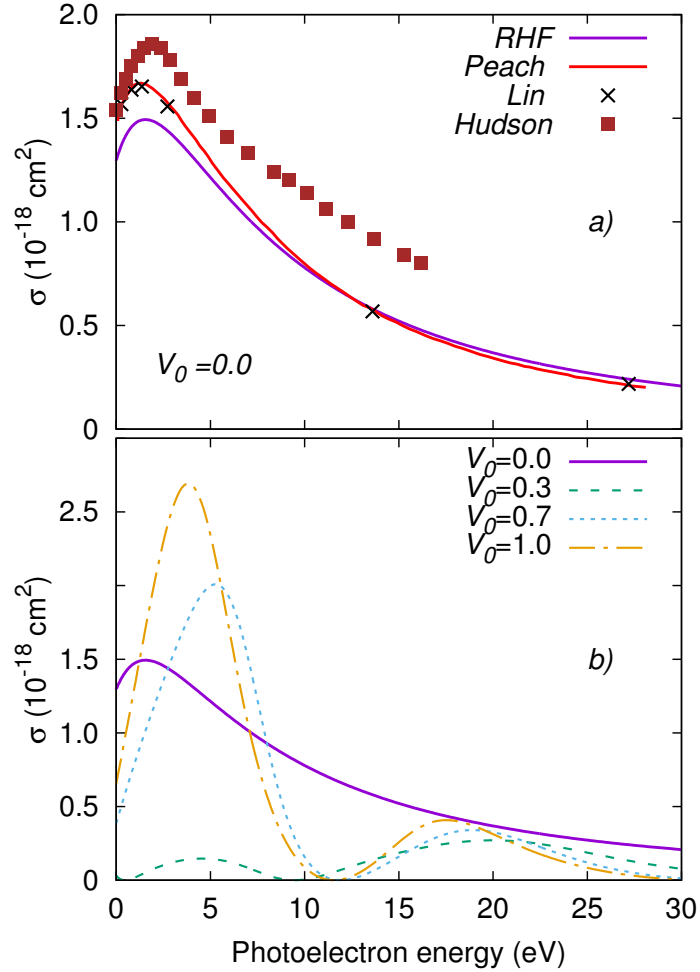
Figure 6.4: The same as Fig. 6.3 but for the Photo-ionization cross section as a function of the photo-electron energy (eV). a) we show our results (solid line) for the free case ($V_0 = 0$ a.u.) in comparison with the theoretical result of Ref. [163] [red solid line], the theoretical results of Ref. [26] [($\times$) symbols], and the experimental results from Ref. [159] [($\blacksquare$) symbols]. b) the photo-ionization cross section for several potential well depth as a function of the photo-electron energy. See text for discussion.

[($\times$) symbols] [26], and the experimental results of Hudson and Carter ($\blacksquare$) [159]. Here, one observes a correspondence between our results and those reported by Peach and Lin and Ho for photo-electron energies larger that 10 eV of photo-electron energy. For lower values of the photo-electron energy, near 2.5 eV, we observe a discrepancy between our results and those reported by Refs. [26, 163]. Within the Slater's X-α approximation, I use one adjustable parameter to obtain the energy spectrum. The pseudo-potential used in Ref. [163] and Ref. [26] uses optimized parameters that are derived by least-square fit to either experimental or theoretical results, leading a proper description of the photo-ionization at low photo-electron energies.

In Fig. 6.4b), I show the PCS results for the encaged lithium atom for several well depths V_0 as a function of the photo-electron energy. Here, the solid line is the free result, as I have described previously in Fig. 6.4a). When the endohedral cavity is present, $V_0 = 0.3$ a.u., one observes a drastic decrease of the PCS for lower values of photo-electron energies and the appearance of Cooper resonances around the photo-electron energies at 4 eV and 21 eV. These energy resonances occur due
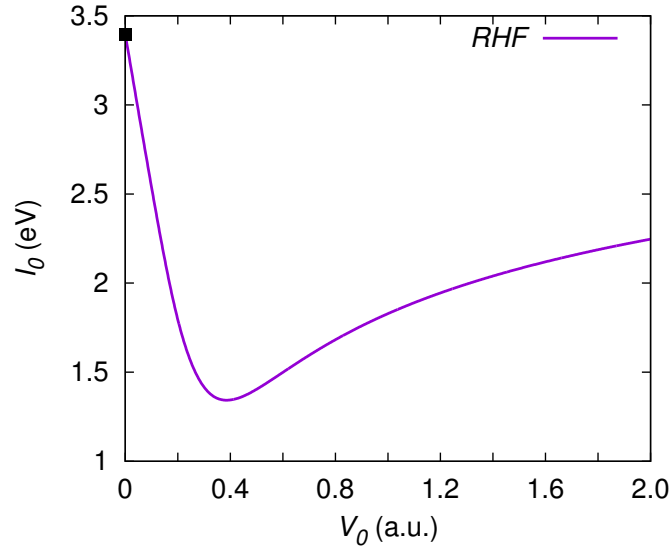
Figure 6.5: The same as Fig. 6.3 but for the mean excitation energy, I_0. In this case, the (■) symbol corresponds to the unconfined result with $I_0 = 3.39698$ eV. See text for details.

to the constructive interference of the photo-electron waves scattered off by the endohedral cage and the outgoing photo-electron wave as in Chapter 4. From Fig. 6.4b), for a well depth of $V_0 = 0.7$ a.u., the PCS is increased for a photo-electron energy of 4 eV. When the well depth is $V_0 = 1.0$ a.u., the PCS is increased for lower values of photo-electron energy and one observes that the resonance position moves towards lower photo-ionization energies. We find that the Cooper resonances are sensitive to the endohedral well depth, as observed in Fig. 6.4b).

Mean excitation energy

In Fig. 6.5, we show the results for the mean excitation energy, I_0, as a function of the well depth V_0. For no endohedral cavity ($V_0 = 0$ a.u.), one finds that the mean excitation energy, for the $2s$ orbital, is $I_0 = 3.39698$ eV in agreement to the results reported by Oddershede and Sabin with $I_0 = 3.29$ eV [169]. As the well depth is increased, the mean excitation energy is decreased reaching a minimum of $I_0 = 1.34428$ eV for $V_0 = 0.4$ a.u.. For larger values of the well depth, the mean excitation energy is increased smoothly reaching a value of $I_0 = 2.24666$ eV for $V_0 = 2$ a.u. The sudden change observed in I_0 is consequence of the change of the $2s \rightarrow 2p$ DOS transition, which is the principal intensity contribution.

6.2   Conclusions and perspectives

In this chapter, I have analyzed the role of the spatial confinement on the dipole oscillator strength derived properties of the lithium atom encaged by an endohedral cavity by means of the Wood-Saxon model potential and the restricted Hartree-Fock approach. It was found that the inner electrons are not modified by the presence of the endohedral cavity due to the strong binding energy from the nucleus. Here, the $2s$ valence electron have suffered a drastic change, as the well depth V_0 is increased and consequently the wave-functions are modified with implications on the photo-ionization and mean excitation energy. For the photo-ionization cross section, it was found the appearance of Cooper resonances as the well depth is increased.

7

General conclusions

In this work, I have shown the relevance of accounting for the dipole and generalized oscillator strength and the implications on the derived electronic properties with consequences on material damage, e.g. photo-ionization cross section, mean excitation energy and stopping cross section (energy loss), for atoms at free and at extreme conditions.

In the free case, I asses the universal character of the stopping cross section in terms of the mean excitation energy target property, under the Bethe approach, for heavy ions colliding with atoms and molecules. Among the complex projectile–target systems in the energy deposition considered here, the scaling law expresses a systematic and universal behavior, regardless of the detailed mechanism for slowing down in the intermediate-to-high collision energies. The scaling law results are in excellent agreement with the available experimental data for high energy regimen within Bethe's theory. From these results, the mean excitation energy is a decisive parameter to account correctly for the stopping cross section. Thus, the determination of the mean excitation energy is crucial, because among other things, it has been established that this parameter has a dependence on the target orbital orientation.

In spite of the target orientation has been studied previously [12, 13], it has only been assessed for the mean excitation energy and not for the generalized oscillator strength and consequently in the stopping cross section. In this thesis, I have studied the effects of taking into account the initial orbital target symmetry and new analytic expressions for the generalized oscillator strength and stopping cross section were derived. These expressions are obtained assuming that the electrons in the target are bound harmonically and the results are within Bethe's theory. These results for the electronic stopping cross section dependence of the initial target symmetry show good agreement in comparison with the experimental data. However, the question is open for a more realistic approach considering the initial target orbital symmetry in spherical coordinates. Nowadays, this is one of my investigation lines.

For atomic systems encaged by an endohedral cavity, I presented a study of how the dipole and generalized oscillator strength are modified and, as a consequence, the dependent electronic properties. I found that the dipole oscillator strength is modified drastically around the first avoided crossing of the ns and $(n+1)s$ energy levels. For H@C$_{60}$ system, the endohedral confinement leads the trapping of the ground state in the cage as the potential well depth is increased. Thus, the photo-ionization cross section and the mean excitation energy are modified, finding the appearance of Cooper resonances for the photo-ionization and a diminishing of the mean excitation energy. With the increase of the well depth, in the case of a hydrogen atom, I calculate the generalized oscillator strength as a function of the confinement conditions, finding that their intensities are modified in comparison with the available free expressions. Thus, the stopping cross section is modified. For low energy collisions, the endohedral cavity effect is reflected in the increase of the stopping cross section, and at high projectile energies, the endohedral cavity is not discernible by the projectile. It was found that the physical properties depend strongly on the two model potential used to describe the endohedral cavity. Although I present new results for the generalized oscillator strength for atomic systems encaged by an endohedral cavity, there are open questions to answer. For example, I assumed through this thesis, that the model potentials that describe the endohedral cavity are static and as a consequence, the carbons that conform the fullerene molecule do not react properly to the interactions of the atomic system. A more realistic approach would be to propose a potential consisting of repulsive and attractive components that

take into account the internal forces between electrons and carbon atoms of the endohedral cage. Furthermore, I have assumed that the atomic systems are at the geometrical center of the endohedral cavity, however, recent research in the field of hydrogen storage points out that, maybe, it is not completely correct. These intriguing aspects of the endohedral cavity are part of my new investigation lines nowadays.

When I consider the $H@C_{60}$ system embedded in a weak plasma interaction, interesting and new features arise from the confinement effects. The hydrogen energy levels and wave-functions are modified and, as a consequence, the dipole and generalized oscillator strength too. It is found that, with the increase of the endohedral well depth and the decrease of the plasma screening length, the electron in the hydrogen atom is bound into the cavity region. This effect is reflected in the delocalization of the energy levels for lower screening lengths for low values of the potential well depth and a change in the wave-functions. For dipole oscillator strength properties, I find the appearance of new structures in the photo-ionization (energy resonances), as well as a drastic change on the mean excitation energy due to the change in the energy levels as a function of the screening length. Furthermore, I compute the generalized oscillator strength for this system finding a strong dependence at low screening lengths. For the electronic stopping cross section, the stronger effect of the plasma is for shallow cavities, in contrast, for deep cavities, the effect of the plasma is negligible with a predominant contribution only from the endohedral cavity.

I hope these findings motivates further study on these system and a guide to perform experimental work. Several improvements for this *ab initio* approach can be done. For example, as I mentioned previously, the model potential cavity could be modified by adding a repulsive term. Furthermore, I could consider a more realistic plasma interaction by proposing a temperature-dependent model potential [76, 77]. Thus, these topics are part of my actual lines of investigation.

Appendix

A

Finite-differences approach

The numerical method of finite-differences in the midpoint grid is described below. If you multiply Eq. (2.61) by $u^*(r)$ on the left and integrates over the entire space, i.e. $0 \leq r \leq \infty$, we have

$$-\frac{1}{2}u^*\frac{d^2u}{dr^2} + V(r)u^*u = Eu^*u, \tag{A.1}$$

$$-\frac{1}{2}\int u^*u''dr + V(r)\int u^*udr = E\int u^*udr, \tag{A.2}$$

where $V(r) = l(l+1)/2r^2 + V_{scre}(r) + V_c(r)$ and the explicit dependence of r on the wave functions has been removed. From Eq. (A.2), the energy is

$$E = \frac{-\frac{1}{2}\int u^*u''dr + V(r)\int u^*udr}{\int u^*udr}. \tag{A.3}$$

Integrating the first integral by parts we obtain

$$E = \frac{\int \left(\frac{1}{2}\frac{\partial u^*}{\partial r}\frac{\partial u}{\partial r} + V(r)u^*u\right)dr}{\int u^*udr}. \tag{A.4}$$

Under the finite-differences approach, the integral and the derivative are defined in terms of the midpoint grid as

$$\int u(r)dr = \sum_{i=1}^{N} u_i(r_{i+1/2} - r_{i-1/2}), \qquad \frac{\partial u}{\partial r} = \frac{u_{i+1/2} - u_{i-1/2}}{r_{i+1/2} - r_{i-1/2}}. \tag{A.5}$$

Introducing Eq. (A.5) in (A.4) and after a little algebra we obtain the Schrödinger equation as

$$\frac{1}{2}\left[\frac{u_j - u_{j-1}}{r_j - r_{j-1}} - \frac{u_{j+1} - u_j}{r_{j+1} - r_j}\right] + V_j u_j(r_{j+1/2} - r_{j-1/2}) = Eu_j(r_{j+1/2} - r_{j-1/2}), \tag{A.6}$$

where the frontier conditions are given by

$$u_0(r_{min}) = 0, \qquad u_N(r_{max}) = 0. \tag{A.7}$$

Eq. (A.6) can be written as a generalized eigenvalue problem as

$$\mathbf{H}\vec{u} = E\mathbf{S}\vec{u}, \tag{A.8}$$

Diagonalizing this equation system by making $\mathbf{S} = \mathbf{L}\mathbf{L}^T$ such that $\vec{\phi} = \mathbf{L}^T\vec{u}$ and $\mathbf{L} = \mathbf{S}^{1/2}$ we obtain

$$\tilde{\mathbf{H}}\vec{\phi} = E\vec{\phi}. \tag{A.9}$$

Where the matrix elements are given as

$$\tilde{H}_{i,i} = \frac{1}{2}\left[\frac{1}{r_i - r_{i-1}} + \frac{1}{r_{i+1} - r_i}\right]\frac{1}{r_{i+1/2} - r_{i-1/2}} + V_i, \tag{A.10}$$

$$\tilde{H}_{i,i+1} = -\frac{1}{2(r_{i+1} - r_i)}\frac{1}{\sqrt{(r_{i+1/2} - r_{i-1/2})(r_{i+3/2} - r_{i+1/2})}}, \tag{A.11}$$

$$\tilde{H}_{i,i-1} = -\frac{1}{2(r_i - r_{i-1})}\frac{1}{\sqrt{(r_{i+1/2} - r_{i-1/2})(r_{i-1/2} - r_{i-3/2})}}. \tag{A.12}$$

Eqs. (A.9)-(A.12) permit us to find the eigenvalues and eigenfunctions of the H@C$_{60}$ system [Eq. (2.61)], the H@C$_{60}$ system embedded in a weak plasma interaction, and for the Li@C$_{60}$ system in the UHF and RHF [Eqs. (2.84) and (2.92) respectively] for different values of the confinement potential V_0 As a consequence we can calculate the DOS and GOS derived electronic properties for free and at extreme conditions.

B

Gauss-Seidel Method

To show the implemetation of the Gauss-Seidel method, we consider the spatial part of the UHF Eqs. (2.75)-(2.77) as

$$\left(\hat{h}_1 + \hat{J}_2 + \hat{J}_3 - \hat{K}_3\right)\psi_1(\mathbf{r}) = \epsilon_1\psi_1(\mathbf{r}), \tag{B.1}$$

$$\left(\hat{h}_2 + \hat{J}_1 + \hat{J}_3\right)\psi_2(\mathbf{r}) = \epsilon_2\psi_2(\mathbf{r}), \tag{B.2}$$

$$\left(\hat{h}_3 + \hat{J}_1 + \hat{J}_2 - \hat{K}_1\right)\psi_3(\mathbf{r}) = \epsilon_3\psi_3(\mathbf{r}), \tag{B.3}$$

where the equations need to be solved simultaneously. For example, Eq. (B.1) is given in terms of their radial part due to the spherical symmetry as

$$\left(\hat{h}_1 + \hat{J}_2 + \hat{J}_3 - \hat{K}_3\right)u_1(r) = \epsilon_1 u_1(r). \tag{B.4}$$

Here we assume that $\psi_1(r) = (u_1(r)/r)Y_{lm}(\theta, \phi)$. The kinetic term from Eq. (2.68) is given as

$$\hat{h}_1 = -\frac{1}{2}\nabla^2 + V(r), \tag{B.5}$$

$$= -\frac{1}{2}\frac{d^2}{dr^2} + V(r), \quad \text{with} \quad V(r) = -\frac{Z}{r} + V_c(r), \tag{B.6}$$

using the latter kinetic term in Eq. (B.4) we re-write it in terms of the finite-differences approach as

$$-\frac{1}{2}\frac{d^2 u_1}{dr^2} = \frac{1}{2}\left[\frac{u_{1,j} - u_{1,j-1}}{r_j - r_{j-1}} - \frac{u_{1,j+1} - u_{1,j}}{r_{j+1} - r_j}\right]\frac{1}{r_{j+1/2} - r_{j-1/2}}, \tag{B.7}$$

$$= h_{1,j-1}u_{1,j-1} + h_{1,j}u_{1,j} + h_{1,j+1}u_{1,j+1}, \tag{B.8}$$

where we define

$$h_{1,j-1} = -\frac{1}{2}\frac{1}{r_j - r_{j-1}}\frac{1}{r_{j+1/2} - r_{j-1/2}}, \tag{B.9}$$

$$h_{1,j} = \frac{1}{2}\left[\frac{1}{r_j - r_{j-1}} + \frac{1}{r_{j+1} - r_j}\right]\frac{1}{r_{j+1/2} - r_{j-1/2}}, \tag{B.10}$$

$$h_{1,j-1} = -\frac{1}{2}\frac{1}{r_{j+1} - r_j}\frac{1}{r_{j+1/2} - r_{j-1/2}}. \tag{B.11}$$

Then, Eq. (B.4) into the finite-differences approach is

$$(h_{1,j-1}u_{1,j-1} + h_{1,j}u_{1,j} + h_{1,j+1}u_{1,j+1} + V_j u_{1,j} + J_{2,j}u_{1,j} + J_{3,j}u_{1,j} - K_{3,j}u_{1,j}) = \epsilon_1 u_{1,j}, \tag{B.12}$$

$$(h_{1,j} + V_j + J_{2,j} + J_{3,j} - K_{3,j} - \epsilon_1)u_{1,j} = -(h_{1,j-1}u_{1,j-1} + h_{1,j+1}u_{1,j+1}), \tag{B.13}$$

here the new wave-function $\bar{u}_{1,j}$ is

$$\bar{u}_{1,j} = -\frac{h_{1,j-1}u_{1,j-1} + h_{1,j+1}u_{1,j+1}}{h_{3,j} + V_j + J_{2,j} + J_{3,j} - K_{3,j} - \epsilon_1} \tag{B.14}$$

where

$$\epsilon_1 = \int dr u_1^*(r) \left(\hat{h}_1 + \hat{J}_2 + \hat{J}_3 - \hat{K}_3\right) u_1(r). \tag{B.15}$$

The improved wave-function is given as

$$u_{1,j}^{new}(r) = (1-\omega)u_{1,j}(r) + \omega\bar{u}_{1,j}(r), \tag{B.16}$$

here $u_{1,j}(r)$ is the initial guess wave-function. In a similar way, for Eqs. (B.2) and (B.3), the new wave-functions $\bar{u}_j$ are

$$\bar{u}_{2,j} = -\frac{h_{2,j-1}u_{2,j-1} + h_{2,j+1}u_{2,j+1}}{h_{2,j} + V_j + J_{1,j} + J_{3,j} - \epsilon_2}, \tag{B.17}$$

$$\bar{u}_{3,j} = -\frac{h_{3,j-1}u_{3,j-1} + h_{3,j+1}u_{3,j+1}}{h_{3,j} + V_j + J_{1,j} + J_{2,j} - K_{1,j} - \epsilon_2}, \tag{B.18}$$

and the improved wave-functions u_j^{new} are

$$u_{2,j}^{new}(r) = (1-\omega)u_{2,j}(r) + \omega\bar{u}_{2,j}(r), \tag{B.19}$$

$$u_{3,j}^{new}(r) = (1-\omega)u_{3,j}(r) + \omega\bar{u}_{3,j}(r), \tag{B.20}$$

with the respective values of ϵ_2 and ϵ_3, as in Eq. (B.15).

Where the Coulumb and Exchange terms are given as

$$\hat{J}_b(\mathbf{r}_1) = \langle\psi_b(\mathbf{r}_2)|\frac{1}{r_{12}}|\psi_b(\mathbf{r}_2)\rangle, \tag{B.21}$$

$$= \int dr_2 \frac{1}{r_{12}}u_b^*(r_2)u_b(r_2), \tag{B.22}$$

$$= \int_0^{r_1} \frac{1}{r_1}u_b^*(r_2)u_b(r_2)dr_2 + \int_{r_1}^\infty \frac{1}{r_2}u_b^*(r_2)u_b(r_2)dr_2, \tag{B.23}$$

$$\hat{K}_b(\mathbf{r}_1) = \langle\psi_b(\mathbf{r}_2)|\frac{1}{r_{12}}|\psi_j(\mathbf{r}_2)\rangle, \tag{B.24}$$

$$= \int dr_2 \frac{1}{r_{12}}u_b(r_2)u_j(r_2), \tag{B.25}$$

$$= \int_0^{r_1} \frac{1}{r_1}u_b^*(r_2)u_j(r_2)dr_2 + \int_{r_1}^\infty \frac{1}{r_2}u_b^*(r_2)u_j(r_2)dr_2. \tag{B.26}$$

Bibliography

[1] Ana María Cetto. *La luz.* Fondo de Cultura Económica, México, 1997.

[2] Gordon W.F. Drake. *Handbook of atomic, molecular, and optical physics.* Springer, 2 edition, 2006.

[3] Plasma Science Committee, editor. *Plasma Science : From Fundamental Research to Technological Applications.* National Academies Press, Washington, D.C., 1 edition, January 1995.

[4] D. Salzmann, editor. *Atomic Physics in Hot Plasmas.* Oxford University Press, Oxford, 1998.

[5] Makoto Kitabatake Kiyotaka Wasa and Hideaki Adachi. *Thin Films Material Technology: Sputtering of Compound Materials.* Springer-Verlag Berlin Heidelberg, Springer-Verlag Berlin Heidelberg, 1 edition, 2004.

[6] Hertz, H. M., Berglund, M., Hansson, B. A.M., Hemberg, O., and Johansson, G. J. Liquid-jet laser-plasma x-ray sources for microscopy and lithography. *J. Phys. IV France*, 11:Pr2–389–Pr2–396, 2001.

[7] A G Michette, R Fedosejevs, S J Pfauntsch, and R Bobkowski. A scanned source x-ray microscope. *Measurement Science and Technology*, 5(5):555, 1994.

[8] H. Bethe. Zur theorie des durchgangs schneller korpuskularstrahlen durch materie. *Annalen der Physik*, 397(3):325–400, 1930.

[9] Biersack J.P. Ziegler J.F. and Littmark U. The stopping and range of ions in solids. *Pergamon Press, New York*, 1985.

[10] E.C. Montenegro, S.A. Cruz, and C. Vargas-Aburto. A universal equation for the electronic stopping of ions in solids. *Physics Letters A*, 92(4):195 – 202, 1982.

[11] R. Cabrera-Trujillo. Stopping power in the independent-particle model: Harmonic oscillator results. *Phys. Rev. A*, 60:3044–3052, Oct 1999.

[12] Henning H. Mikkelsen, Jens Oddershede, John R. Sabin, and Ejvind Bonderup. A bethe theory for the directional dependence of stopping by molecules. *Nuclear Instruments and Methods in Physics Research Section B: Beam Interactions with Materials and Atoms*, 100(4):451 – 457, 1995.

[13] Stephan P. A. Sauer, Jens Oddershede, and John R. Sabin. Mean excitation energies and their directional characteristics for energy deposition by swift ions on the dna and rna nucleobases. *The Journal of Physical Chemistry C*, 114(48):20335–20341, 2010.

[14] K. D. Sen, editor. *Electronic Structure of Quantum Confined Atoms and Molecules.* Springer International Publishing, Switzerland, 2014.

[15] S. A. Cruz, J Sabin, and E Brandas, editors. *Advances in Quantum Chemistry*, volume 57. Elsevier, Amsterdam, June 2009.

[16] S. A. Cruz, J Sabin, and E Brandas, editors. *Advances in Quantum Chemistry*, volume 58. Elsevier, Amsterdam, June 2009.

[17] Russel B. Ross, Claudia M. Cardona, Dirk M. Guldi, Shankara Gayathri Sankaranarayanan, Matthew O. Reese, Nikos Kopidakis, Jeff Peet, Bright Walker, Guillermo C. Bazan, Edward Van Keuren, Brian C. Holloway, and Martin Drees. Endohedral fullerenes for organic photovoltaic devices. *Nat Mater*, 8(3):208–212, 2014.

[18] Simon C Benjamin, Arzhang Ardavan, G Andrew D Briggs, David A Britz, Daniel Gunlycke, John Jefferson, Mark A G Jones, David F Leigh, Brendon W Lovett, Andrei N Khlobystov, S A Lyon, John J L Morton, Kyriakos Porfyrakis, Mark R Sambrook, and Alexei M Tyryshkin. Towards a fullerene-based quantum computer. *Journal of Physics: Condensed Matter*, 18(21):S867, 2006.

[19] Stephen Ornes. Core concept: Quantum dots. *Proceedings of the National Academy of Sciences*, 113(11):2796–2797, 2016.

[20] Olga V. Pupysheva, Amir A. Farajian, and Boris I. Yakobson. Fullerene nanocage capacity for hydrogen storage. *Nano Letters*, 8(3):767–774, 2008. PMID: 17924697.

[21] Mirza Ali Mofazzal Jahromi, Parham Sahandi Zangabad, Seyed Masoud Moosavi Basri, Keyvan Sahandi Zangabad, Ameneh Ghamarypour, Amir R. Aref, Mahdi Karimi, and Michael R. Hamblin. Nanomedicine and advanced technologies for burns: Preventing infection and facilitating wound healing. *Advanced Drug Delivery Reviews*, 123:33 – 64, 2018. Advances and new technologies in the treatment of burn injury.

[22] M. Ya. Amusia, A. S. Baltenkov, and U. Becker. Strong oscillations in the photoionization of 5s electrons in xe@c$_{60}$ endohedral atoms. *Phys. Rev. A*, 62:012701, Jun 2000.

[23] J P Connerade, V K Dolmatov, P A Lakshmi, and S T Manson. Electron structure of endohedrally confined atoms: atomic hydrogen in an attractive shell. *Journal of Physics B: Atomic, Molecular and Optical Physics*, 32(10):L239, 1999.

[24] V.K. Dolmatov, A.S. Baltenkov, J.-P. Connerade, and S.T. Manson. Structure and photoionization of confined atoms. *Radiation Physics and Chemistry*, 70(13):417 – 433, 2004.

[25] V K Dolmatov, J L King, and J C Oglesby. Diffuse versus square-well confining potentials in modelling a@c$_{60}$ atoms. *Journal of Physics B: Atomic, Molecular and Optical Physics*, 45(10):105102, 2012.

[26] C Y Lin and Y K Ho. Photoionization of atoms encapsulated by cages using the powerexponential potential. *Journal of Physics B: Atomic, Molecular and Optical Physics*, 45(14):145001, 2012.

[27] S A Ndengué and O Motapon. Electric response of endohedrally confined hydrogen atoms. *Journal of Physics B: Atomic, Molecular and Optical Physics*, 41(4):045001, 2008.

[28] O. Motapon, S. A. Ndengué, and K. D. Sen. Static and dynamic dipole polarizabilities and electron density at origin: Ground and excited states of hydrogen atom confined in multiwalled fullerenes. *International Journal of Quantum Chemistry*, 111(15):4425–4432, 2011.

[29] W. Jaskólski. Confined many-electron systems. *Physics Reports*, 271(1):1 – 66, 1996.

[30] J P Connerade, V K Dolmatov, and P A Lakshmi. The filling of shells in compressed atoms. *Journal of Physics B: Atomic, Molecular and Optical Physics*, 33(2):251, 2000.

[31] M. F. Hasoğlu, H.-L. Zhou, and S. T. Manson. Correlation study of endohedrally confined alkaline-earth-metal atoms (a@c$_{60}$). *Phys. Rev. A*, 93:022512, Feb 2016.

[32] Mitio Inokuti. Inelastic collisions of fast charged particles with atoms and molecules—the bethe theory revisited. *Rev. Mod. Phys.*, 43:297–347, Jul 1971.

[33] N.F. Mott and H.S.W. Massey, editors. *Theory of Atomic Collisions.* Oxford University Press, U.K., 3 edition, November 1965.

[34] Hans A. Bethe and Roman Jackiw, editors. *Intermediate quantum mechanics.* Westview Press, Boulder, Colo., EE.UU., 3 edition, November 1997.

[35] R.K. Janev, Songbin Zhang, and Jianguo Wang. Review of quantum collision dynamics in debye plasmas. *Matter and Radiation at Extremes*, 1(5):237 – 248, 2016.

[36] Y. Y. Qi, J. G. Wang, and R. K. Janev. Photoionization of hydrogen-like ions in dense quantum plasmas. *Physics of Plasmas*, 24(6):062110, 2017.

[37] Y. Y. Qi, J. G. Wang, and R. K. Janev. Dynamics of photoionization of hydrogenlike ions in debye plasmas. *Phys. Rev. A*, 80:063404, Dec 2009.

[38] T. N. Chang and T. K. Fang. Atomic photoionization in a changing plasma environment. *Phys. Rev. A*, 88:023406, Aug 2013.

[39] D. H. H. Hoffmann, K. Weyrich, H. Wahl, D. Gardés, R. Bimbot, and C. Fleurier. Energy loss of heavy ions in a plasma target. *Phys. Rev. A*, 42:2313–2321, Aug 1990.

[40] A. B. Zylstra, J. A. Frenje, P. E. Grabowski, C. K. Li, G. W. Collins, P. Fitzsimmons, S. Glenzer, F. Graziani, S. B. Hansen, S. X. Hu, M. Gatu Johnson, P. Keiter, H. Reynolds, J. R. Rygg, F. H. Séguin, and R. D. Petrasso. Measurement of charged-particle stopping in warm dense plasma. *Phys. Rev. Lett.*, 114:215002, May 2015.

[41] Ge Xu, M. D. Barriga-Carrasco, A. Blazevic, B. Borovkov, D. Casas, K. Cistakov, R. Gavrilin, M. Iberler, J. Jacoby, G. Loisch, R. Morales, R. Mäder, S.-X. Qin, T. Rienecker, O. Rosmej, S. Savin, A. Schönlein, K. Weyrich, J. Wiechula, J. Wieser, G. Q. Xiao, and Y. T. Zhao. Determination of hydrogen density by swift heavy ions. *Phys. Rev. Lett.*, 119:204801, Nov 2017.

[42] George McGinn. Atomic and molecular calculations with the pseudopotential method. vii onevalenceelectron photoionization cross sections. *The Journal of Chemical Physics*, 53(9):3635–3640, 1970.

[43] P.G. Burke and W.D. Robb. The r-matrix theory of atomic processes. *Advances in Atomic and Molecular Physics*, 11:143 – 214, 1976.

[44] G Peach, H E Saraph, and M J Seaton. Atomic data for opacity calculations. ix. the lithium isoelectronic sequence. *Journal of Physics B: Atomic, Molecular and Optical Physics*, 21(22):3669, 1988.

[45] N. Zettili. *Quantum Mechanics: Concepts and applications.* John Wiley y Sons Inc., 1 edition, 2001.

[46] H. Bethe and Salpeter. *Quantum mechanics of one and two electrons.* Addison-Wesley Publishing company, 3 edition.

[47] H. Friedrich, editor. *Theoretical atomic physics.* Springer-Verlag, Berlin Heidelberg, 3 edition, 2006.

[48] L. M. Ugray and R. C. Shiell. Elucidating fermi's golden rule via bound-to-bound transitions in a confined hydrogen atom. *American Journal of Physics*, 81(3):206–210, 2013.

[49] Mitio Inokuti. Inelastic collisions of fast charged particles with atoms and molecules—the bethe theory revisited. *Rev. Mod. Phys.*, 43:297–347, Jul 1971.

[50] A. Zsabo and N. Ostlund. *Modern Quantum Chemistry, Introduction to Advanced Electric Structure Theory.* Dover Publications Inc., 1 edition, 1996.

[51] W. H. Bragg y R. Kleeman. *Phil. Mag.*, (10):305, 1918.

[52] H.J. Weber and G. B. Arfken. *Essential Mathematical Methods for Physicists.* Elsevier Academic Press, 6 edition, 2005.

[53] G.B. Arfken, H.J. Weber, and F.E. Harris. *Mathematical Methods for Physicists: A Comprehensive Guide.* Academic Press, Elsevier, 7th edition edition, 2013.

[54] R. Cabrera-Trujillo and S. A. Cruz. Confinement approach to pressure effects on the dipole and the generalized oscillator strength of atomic hydrogen. *Phys. Rev. A*, 87:012502, Jan 2013.

[55] L.N. Trujillo-Lopez, C. Martinez-Flores, and R. Cabrera-Trujillo. Universal scaling behavior of molecular electronic stopping cross section for protons colliding with small molecules and nucleobases. *Nuclear Instruments and Methods in Physics Research Section B: Beam Interactions with Materials and Atoms*, 313:5 – 13, 2013.

[56] San Y. Chu and Arthur A. Frost. Floating spherical gaussian orbital model of molecular structure. ix. diatomic molecules of firstrow and secondrow atoms. *The Journal of Chemical Physics*, 54(2):764–768, 1971.

[57] R. Cabrera-Trujillo and S. A. Cruz. Confinement approach to pressure effects on the dipole and the generalized oscillator strength of atomic hydrogen. *Phys. Rev. A*, 87:012502, Jan 2013.

[58] Steven Koonin and Dawn C. Meredith. *Computational Physics: Fortran Version.* Westview Press, 1998.

[59] J. C. Slater. A simplification of the hartree-fock method. *Phys. Rev.*, 81:385–390, Feb 1951.

[60] K. D. Sen, editor. *Electronic Structure of Quantum Confined Atoms and Molecules.* Springer International Publishing, Switzerland, 2014.

[61] Zhifan Chen and A. Z. Msezane. Photoionization of the xe atom and xe@c60 molecule. *The European Physical Journal D*, 65(3):353–356, 2011.

[62] M Ya Amusia, A S Baltenkov, L V Chernysheva, Z Felfli, and A Z Msezane. Dramatic distortion of the 4d giant resonance by the c 60 fullerene shell. *Journal of Physics B: Atomic, Molecular and Optical Physics*, 38(10):L169, 2005.

[63] V.K. Dolmatov. Photoionization of atoms encaged in spherical fullerenes. *Advances in Quantum Chemistry*, 58:13 – 68, 2009.

[64] Roger D. Woods and David S. Saxon. Diffuse surface optical model for nucleon-nuclei scattering. *Phys. Rev.*, 95:577–578, Jul 1954.

[65] E M Nascimento, F V Prudente, M N Guimaraes, and A M Maniero. A study of the electron structure of endohedrally confined atoms using a model potential. *Journal of Physics B: Atomic, Molecular and Optical Physics*, 44(1):015003, 2011.

[66] Andy Rüdel, Rainer Hentges, Uwe Becker, Himadri S. Chakraborty, Mohamed E. Madjet, and Jan M. Rost. Imaging delocalized electron clouds: Photoionization of c_{60} in fourier reciprocal space. *Phys. Rev. Lett.*, 89:125503, Aug 2002.

[67] S. W. J. Scully, E. D. Emmons, M. F. Gharaibeh, R. A. Phaneuf, A. L. D. Kilcoyne, A. S. Schlachter, S. Schippers, A. Müller, H. S. Chakraborty, M. E. Madjet, and J. M. Rost. Photoexcitation of a volume plasmon in c_{60} ions. *Phys. Rev. Lett.*, 94:065503, Feb 2005.

[68] Tatiana Korona, Andreas Hesselmann, and Helena Dodziuk. Symmetry-adapted perturbation theory applied to endohedral fullerene complexes: A stability study of h2@c60 and 2h2@c60. *Journal of Chemical Theory and Computation*, 5(6):1585 – 1596, 6 2009.

[69] Y. B. Xu, M. Q. Tan, and U. Becker. Oscillations in the photoionization cross section of c_{60}. *Phys. Rev. Lett.*, 76:3538–3541, May 1996.

[70] K. Nishikawa and M. Wakatani, editors. *Plasma Physics: Basic Theory with Fusion Applications*. Springer-Verlag Berlin Heidelberg, Switzerland, 3 edition, 2000.

[71] Oleksiy V. Penkov, Mahdi Khadem, Won-Suk Lim, and Dae-Eun Kim. A review of recent applications of atmospheric pressure plasma jets for materials processing. *Journal of Coatings Technology and Research*, 12(2):225–235, Mar 2015.

[72] Y Kuramitsu and Y Sakawa et al. Laboratory investigations on the origins of cosmic rays. *Plasma Physics and Controlled Fusion*, 54(12):124049, 2012.

[73] Michael S. Murillo and Jon C. Weisheit. Dense plasmas, screened interactions, and atomic ionization. *Physics Reports*, 302(1):1 – 65, 1998.

[74] A.N. Sil, S. Canuto, and P.K. Mukherjee. Spectroscopy of confined atomic systems: Effect of plasma. *Advances in Quantum Chemistry*, 58:115 – 175, 2009.

[75] E Hückel and P Debye. The theory of electrolytes: I. lowering of freezing point and related phenomena. *Phys. Z*, 24:185–206, 1923.

[76] L. G. Stanton and M. S. Murillo. Unified description of linear screening in dense plasmas. *Phys. Rev. E*, 91:033104, Mar 2015.

[77] G. P. Zhao, L. Liu, J. G. Wang, and R. K. Janev. Spectral properties of hydrogen-like ions in finite-temperature quantum plasmas. *Physics of Plasmas*, 24(5):053509, 2017.

[78] Y. Y. Qi, J. G. Wang, and R. K. Janev. Static dipole polarizability of hydrogenlike ions in debye plasmas. *Phys. Rev. A*, 80:032502, Sep 2009.

[79] Steven Koonin and Dawn C. Meredith. *Computational Physics: Fortran Version*. Westview Press, 1998.

[80] Y. B. Xu, M. Q. Tan, and U. Becker. Oscillations in the photoionization cross section of c_{60}. *Phys. Rev. Lett.*, 76:3538–3541, May 1996.

[81] V K Dolmatov, J L King, and J C Oglesby. Diffuse versus square-well confining potentials in modelling $a@c_60$ atoms. *Journal of Physics B: Atomic, Molecular and Optical Physics*, 45(10):105102, 2012.

[82] Hans-Dieter Betz. Charge states and charge-changing cross sections of fast heavy ions penetrating through gaseous and solid media. *Rev. Mod. Phys.*, 44:465–539, Jul 1972.

[83] M. Abdesselam, J.P. Stoquert, G. Guillaume, M. Hage-Ali, J.J. Grob, and P. Siffert. Stopping power of c and al ions in solids. *Nuclear Instruments and Methods in Physics Research Section B: Beam Interactions with Materials and Atoms*, 61(4):385 – 393, 1991.

[84] J. M. Anthony and W. A. Lanford. Stopping power and effective charge of heavy ions in solids. *Phys. Rev. A*, 25:1868–1879, Apr 1982.

[85] G. de M. Azevedo, M. Behar, J. F. Dias, P. L. Grande, D. L. da Silva, and G. Schiwietz. Random and channeling stopping powers of he and li ions in si. *Phys. Rev. B*, 65:075203, Jan 2002.

[86] R. Bimbot, H. Gauvin, I. Orliange, R. Anne, G. Bastin, and F. Hubert. Stopping powers of solids for 40ar and 40ca ions at intermediate energies (2080 mev/u). *Nuclear Instruments and Methods in Physics Research Section B: Beam Interactions with Materials and Atoms*, 17(1):1 – 10, 1986.

[87] R. Bimbot, C. Cabot, D. Gardes, H. Gauvin, R. Hingmann, I. Orliange, L. de Reilhac, and F. Hubert. Stopping power of gases for heavy ions: Gas-solid effect: I. 213 mev/u ne and ar projectiles. *Nuclear Instruments and Methods in Physics Research Section B: Beam Interactions with Materials and Atoms*, 44(1):1 – 18, 1989.

[88] H. Gauvin, R. Bimbot, J. Herault, R. Anne, G. Bastin, and F. Hubert. Stopping powers of solids for 16o ions at intermediate energies (2095 mev/u). *Nuclear Instruments and Methods in Physics Research Section B: Beam Interactions with Materials and Atoms*, 28(2):191 – 194, 1987.

[89] H. Gauvin, R. Bimbot, J. Herault, B. Kubica, R. Anne, G. Bastin, and F. Hubert. Stopping powers of solids for 84,86kr, 100mo and 129,132xe ions at intermediate energies (2045 mev/u) and the charge state distributions at equilibrium. *Nuclear Instruments and Methods in Physics Research Section B: Beam Interactions with Materials and Atoms*, 47(4):339 – 350, 1990.

[90] J. Herault, R. Bimbot, H. Gauvin, B. Kubica, R. Anne, G. Bastin, and F. Hubert. Stopping powers of gases for heavy ions (o, ar, kr, xe) at intermediate energy (20100 mev/u). vanishing of the gassolid effect. *Nuclear Instruments and Methods in Physics Research Section B: Beam Interactions with Materials and Atoms*, 61(2):156 – 166, 1991.

[91] Claus Hanke and Jens Laursen. Stopping cross sections for particles from 1.0 to 8.5 mev in h2, he, n2, o2, ne, kr and xe. *Nuclear Instruments and Methods*, 151(1):253 – 260, 1978.

[92] A. Javanainen, M. Sillanpaa, W. H. Trzaska, A. Virtanen, G. Berger, W. Hajdas, R. Harboe-Sorensen, H. Kettunen, T. Malkiewicz, M. Mutterer, J. Perkowski, A. Pirojenko, I. Riihimaki, T. Sajavaara, G. Tyurin, and H. J. Whitlow. Experimental linear energy transfer of heavy ions in silicon for radef cocktail species. *IEEE Transactions on Nuclear Science*, 56(4):2242–2246, Aug 2009.

[93] Joseph G. Kelley, Bach Sellers, and Frederick A. Hanser. Energy-loss and stopping-power measurements between 2 and 10 mev/amu for ^{12}C, ^{14}N, and ^{16}O in silicon. *Phys. Rev. B*, 8:103–106, Jul 1973.

[94] A.D. Fertman, T.Yu. Mutin, M.M. Basko, A.A. Golubev, T.V. Kulevoy, R.P. Kuybeda, V.I. Pershin, I.V. Roudskoy, and B.Yu. Sharkov. Stopping power measurements for 100-kev/u cu ions in hydrogen and nitrogen. *Nuclear Instruments and Methods in Physics Research Section B: Beam Interactions with Materials and Atoms*, 247(2):199 – 204, 2006.

[95] F. W. Martin and L. C. Northcliffe. Energy loss and effective charge of he, c, and ar ions below 10 mev/amu in gases. *Phys. Rev.*, 128:1166–1174, Nov 1962.

[96] J. Perkowski, J. Andrzejewski, A. Climent-Font, G. Knyazheva, V. Lyapin, T. Malkiewicz, A. Munoz-Martin, and W.H. Trzaska. Stopping power measurement of 48ca in a broad energy range in solid absorbers. *Nuclear Instruments and Methods in Physics Research Section B: Beam Interactions with Materials and Atoms*, 249(1):55 – 57, 2006. Ion Beam Analysis.

[97] J. Raisanen, E. Rauhala, M. Bjornberg, A. Z. Kiss, and J. Dominguez. Stopping powers of al and sn for 4he, 7li, 11b, 12c, 14n and 16o ions in the energy range 0.52.6 mev/amu. *Radiation Effects and Defects in Solids*, 118(2):97–103, 1991.

[98] Gerald Reiter, N. Kniest, E. Pfaff, and G. Clausnitzer. Proton and helium stopping cross sections in h2, he, n2, o2, ne, ar, kr, xe, {CH4} and {CO2}. *Nuclear Instruments and Methods in Physics Research Section B: Beam Interactions with Materials and Atoms*, 44(4):399 – 411, 1990.

[99] D.C. Santry and R.D. Werner. Stopping power measurements of c, al, si, ti, ni, ag, au and mylar using radioactive alpha sources. *Nuclear Instruments and Methods in Physics Research Section B: Beam Interactions with Materials and Atoms*, 1(1):13 – 15, 1984.

[100] Bach Sellers, Frederick A. Hanser, and Joseph G. Kelley. Energy-loss and stopping-power measurements between 2 and 10 mev/amu for ^{3}He and ^{4}He in silicon. *Phys. Rev. B*, 8:98–102, Jul 1973.

[101] C. Tschalär and Hans Bichsel. Mean excitation potential of light compounds. *Phys. Rev.*, 175:476–478, Nov 1968.

[102] H. Weick, H. Geissel, C. Scheidenberger, F. Attallah, T. Baumann, D. Cortina, M. Hausmann, B. Lommel, G. Munzenberg, N. Nankov, F. Nickel, T. Radon, H. Schatz, K. Schmidt, J. Stadlmann, K. Summerer, M. Winkler, and H. Wollnik. Slowing down of relativistic few-electron heavy ions. *Nuclear Instruments and Methods in Physics Research Section B: Beam Interactions with Materials and Atoms*, 164-165:168 – 179, 2000.

[103] M. Zadro, A. Di Pietro, P. Figuera, M. Fisichella, M. Lattuada, A. Maggio, F. Pansini, M. Papa, V. Scuderi, O.Yu. Goryunov, and V.V. Ostashko. Stopping power of helium gas for 9be ions from 2 to 31mev. *Nuclear Instruments and Methods in Physics Research Section B: Beam Interactions with Materials and Atoms*, 259(2):836 – 840, 2007.

[104] H. K. Reynolds, D. N. F. Dunbar, W. A. Wenzel, and W. Whaling. The stopping cross section of gases for protons, 30-600 kev. *Phys. Rev.*, 92:742–748, Nov 1953.

[105] Robin Golser and Dieter Semrad. Energy loss of hydrogen and helium ions in hydrogen and helium gas: looking for exceptions from velocity proportionality. *Nuclear Instruments and Methods in Physics Research Section B: Beam Interactions with Materials and Atoms*, 69(1):18 – 21, 1992.

[106] H. Geissel, Y. Laichter, W.F.W. Schneider, and P. Armbruster. Energy loss and energy loss straggling of fast heavy ions in matter. *Nuclear Instruments and Methods in Physics Research*, 194(1):21 – 29, 1982.

[107] A.Z. Kiss, E. Somorjai, J. Raisanen, and E. Rauhala. Stopping powers of 1.57.2 mev 4he ions in havar, nickel, kapton and mylar. *Nuclear Instruments and Methods in Physics Research Section B: Beam Interactions with Materials and Atoms*, 39(1):15 – 17, 1989.

[108] Pratibha, V. Sharma, P.K. Diwan, Shyam Kumar, S.A. Khan, and D.K. Avasthi. Energy loss and straggling in lr-115 and kapton polymeric foils for energetic ions. *Nuclear Instruments and Methods in Physics Research Section B: Beam Interactions with Materials and Atoms*, 266(11):2556 – 2563, 2008.

[109] E. Rauhala and J. Raisanen. Stopping powers of 0.58.3 mev protons in havar, nickel, kapton and mylar. *Nuclear Instruments and Methods in Physics Research Section B: Beam Interactions with Materials and Atoms*, 35(2):130 – 134, 1988.

[110] N. Shiomi-Tsuda, N. Sakamoto, and H. Ogawa. Stopping powers of mylar for protons from 4 to 11.5 mev. *Nuclear Instruments and Methods in Physics Research Section B: Beam Interactions with Materials and Atoms*, 103(3):255 – 260, 1995.

[111] D I Thwaites. Stopping cross-sections of liquid water and water vapour for alpha particles within the energy region 0.3 to 5.5 mev. *Physics in Medicine and Biology*, 26(1):71, 1981.

[112] Stephan P. A. Sauer, Jens Oddershede, and John R. Sabin. Mean excitation energies and their directional characteristics for energy deposition by swift ions on the dna and rna nucleobases. *The Journal of Physical Chemistry C*, 114(48):20335–20341, 2010.

[113] H. Baumgart, W. Arnold, H. Berg, E. Huttel, and G. Clausnitzer. Proton stopping powers in various gases. *Nuclear Instruments and Methods in Physics Research*, 204(23):597 – 604, 1983.

[114] Peter K. Weyl. The energy loss of hydrogen, helium, nitrogen, and neon ions in gases. *Phys. Rev.*, 91:289–296, Jul 1953.

[115] John T. Park and E. J. Zimmerman. Stopping cross sections of some hydrocarbon gases for 40-250 kev protons and helium ions. *Phys. Rev.*, 131:1611–1618, Aug 1963.

[116] E. Bonderup and P. Hvelplund. Stopping power and energy straggling for swift protons. *Phys. Rev. A*, 4:562–569, Aug 1971.

[117] J. E. Brolley and F. L. Ribe. Energy loss by 8.86-mev deuterons and 4.43-mev protons. *Phys. Rev.*, 98:1112–1117, May 1955.

[118] M. Bader, R. E. Pixley, F. S. Mozer, and W. Whaling. Stopping cross section of solids for protons, 50-600 kev. *Phys. Rev.*, 103:32–38, Jul 1956.

[119] Ch. Eppacher, R. Diez Muino, D. Semrad, and A. Arnau. Stopping power of lithium for hydrogen projectiles. *Nuclear Instruments and Methods in Physics Research Section B: Beam Interactions with Materials and Atoms*, 96(3):639 – 642, 1995. The Interaction of Swift Particles and Electromagnetic Fields with Matter.

[120] D.C. Santry and R.D. Werner. Stopping powers of c, al, si, ti, ni, ag and au for deuterons. *Nuclear Instruments and Methods in Physics Research*, 188(1):211 – 216, 1981.

[121] Peter Bauer. Stopping power of light ions near the maximum. *Nuclear Instruments and Methods in Physics Research Section B: Beam Interactions with Materials and Atoms*, 45(1):673 – 683, 1990.

[122] T.R. Ophel and G.W. Kerr. A study of the energy loss of 0.364.5 mev protons in thin carbon foils. *Nuclear Instruments and Methods*, 128(1):149 – 155, 1975.

[123] S. Gorodetzky, Mme A. Chevallier, A. Pape, J.Cl. Sens, Mme A.M. Bergdolt, M. Bres, and R. Armbruster. Mesure des pouvoirs d'arre c, ca, au et caf2 pour des protons d'rgie comprise entre 0.4 et 6 mev. *Nuclear Physics A*, 91(1):133 – 144, 1967.

[124] J.B. Swint, R.M. Prior, and J.J. Ramirez. Energy loss of protons in gases. *Nuclear Instruments and Methods*, 80(1):134 – 140, 1970.

[125] D.L. Mason, R.M. Prior, and A.R. Quinton. The energy straggling of 1-mev protons in gases. *Nuclear Instruments and Methods*, 45(1):41 – 44, 1966.

[126] Arthur B. Chilton, John N. Cooper, and James C. Harris. The stopping powers of various elements for protons of energies from 400 to 1050 kev. *Phys. Rev.*, 93:413–418, Feb 1954.

[127] Zhifan Chen and Alfred Z. Msezane. Photoabsorption spectra of xe atoms encapsulated inside fullerenes. *The European Physical Journal D*, 69(3):88, Mar 2015.

[128] Mohammad H. Javani, Himadri S. Chakraborty, and Steven T. Manson. Valence photoionization of noble-gas atoms confined in the fullerene c_{60}. *Phys. Rev. A*, 89:053402, May 2014.

[129] A S Baltenkov, S T Manson, and A Z Msezane. Jellium model potentials for the c 60 molecule and the photoionization of endohedral atoms, a@c 60. *Journal of Physics B: Atomic, Molecular and Optical Physics*, 48(18):185103, 2015.

[130] A. L. D. Kilcoyne, A. Aguilar, A. Müller, S. Schippers, C. Cisneros, G. AlnaWashi, N. B. Aryal, K. K. Baral, D. A. Esteves, C. M. Thomas, and R. A. Phaneuf. Confinement resonances in photoionization of $Xe@c_{60}^{+}$. *Phys. Rev. Lett.*, 105:213001, Nov 2010.

[131] H. Bethe. Zur theorie des durchgangs schneller korpuskularstrahlen durch materie. *Annalen der Physik*, 397(3):325–400, 1930.

[132] Arup Banerjee, K. D. Sen, Jorge Garza, and Rubicelia Vargas. Mean excitation energy, static polarizability, and hyperpolarizability of the spherically confined hydrogen atom. *The Journal of Chemical Physics*, 116(10):4054–4057, 2002.

[133] R. Cabrera-Trujillo and S.A. Cruz. Accurate evaluation of pressure effects on the electronic stopping cross section and mean excitation energy of atomic hydrogen beyond the bethe approximation. *Nuclear Instruments and Methods in Physics Research Section B: Beam Interactions with Materials and Atoms*, 320:51 – 56, 2014.

[134] Hans A. Bethe and Roman Jackiw, editors. *Intermediate quantum mechanics*. Westview Press, Boulder, Colo., EE.UU., 3 edition, November 1997.

[135] N.F. Mott and H.S.W. Massey, editors. *Theory of Atomic Collisions*. Oxford University Press, U.K., 3 edition, November 1965.

[136] P Moretto-Capelle, D Bordenave-Montesquieu, A Rentenier, and A Bordenave-Montesquieu. Interaction of protons with the c 60 molecule: calculation of deposited energies and electronic stopping cross sections (v 5 au). *Journal of Physics B: Atomic, Molecular and Optical Physics*, 34(18):L611, 2001.

[137] Wolfgang Lothar Wiese, Mo W Smith, and BM Glennon. Atomic transition probabilities. volume 1. hydrogen through neon. Technical report, National Bureau of standards Washington DC inst for basic standards, 1966.

[138] M. Ya. Amusia. Photoionization and vacancy decay of endohedral atoms. *Journal of Electron Spectroscopy and Related Phenomena*, 161(1):112 – 120, 2007.

[139] Hans Bichsel. Stopping power of hydrogen atoms. *Phys. Rev. A*, 43:4030–4031, Apr 1991.

[140] Madhusmita Das. Transition energies and polarizabilities of hydrogen like ions in plasma. *Physics of Plasmas*, 19(9):092707, 2012.

[141] H. W. Li and Sabyasachi Kar. Polarizabilities of li and na in debye plasmas. *Physics of Plasmas*, 19(7):073303, 2012.

[142] Hua-Wei Li, Sabyasachi Kar, and Pinghui Jiang. Calculations of dynamic dipole polarizabilities of li and na atoms in debye plasma using the model potential technique. *International Journal of Quantum Chemistry*, 113(10):1493–1497.

[143] Roger D. Woods and David S. Saxon. Diffuse surface optical model for nucleon-nuclei scattering. *Phys. Rev.*, 95:577–578, Jul 1954.

[144] Shuai Kang, You-Chang Yang, Juan He, Fei-Qiao Xiong, and Ning Xu. The hydrogen atom confined in both debye screening potential and impenetrable spherical box. *Central European Journal of Physics*, 11(5):584–593, May 2013.

[145] B. Saha, P. K. Mukherjee, and G. H. F. Diercksen. Energy levels and structural properties of compressed hydrogen atom under debye screening. *A & A*, 396:337, Nov 2002.

[146] Sonia Lumb, Shalini Lumb, and Vinod Prasad. Photoexcitation and ionization of a hydrogen atom confined by a combined effect of a spherical box and debye plasma. *Physics Letters A*, 379(18):1263 – 1269, 2015.

[147] Sonia Lumb, Shalini Lumb, and Vinod Nautiyal. Photoexcitation and ionization of hydrogen atom confined in debye environment. *The European Physical Journal D*, 69(7):176, Jul 2015.

[148] C. Y. Lin and Y. K. Ho. Effects of screened coulomb (yukawa) and exponential-cosine-screened coulomb potentials on photoionization of h and he+. *The European Physical Journal D*, 57(1):21–26, Mar 2010.

[149] M. Ya. Amusia. Photoionization and vacancy decay of endohedral atoms. *Journal of Electron Spectroscopy and Related Phenomena*, 161(1):112 – 120, 2007.

[150] R. Cabrera-Trujillo and S.A. Cruz. Accurate evaluation of pressure effects on the electronic stopping cross section and mean excitation energy of atomic hydrogen beyond the bethe approximation. *Nuclear Instruments and Methods in Physics Research Section B: Beam Interactions with Materials and Atoms*, 320:51 – 56, 2014.

[151] Hans Bichsel. Stopping power of hydrogen atoms. *Phys. Rev. A*, 43:4030–4031, Apr 1991.

[152] J.N. Bardsley. Pseudopotential calculations of alkali interactions. *Chemical Physics Letters*, 7(5):517 – 520, 1970.

[153] Peter Schwerdtfeger. The pseudopotential approximation in electronic structure theory. *ChemPhysChem*, 12(17):3143–3155, 2011.

[154] R.K Nesbet and R.E Watson. Restricted and unrestricted hartree-fock calculations for atomic lithium. *Annals of Physics*, 9(2):260 – 271, 1960.

[155] A Hibbert. Z -1/2 expansion of the unrestricted hartree-fock equations for the ground state of lithium. *Journal of Physics B: Atomic and Molecular Physics*, 1(6):1048, 1968.

[156] A. W. Weiss. The calculation of atomic oscillator strengths: the lithium atom revisited. *Canadian Journal of Chemistry*, 70(2):456–463, 1992.

[157] Kwong T. Chung. Theory of transition rates in fewelectron ions. *AIP Conference Proceedings*, 274(1):381–388, 1993.

[158] Frederick W. King. Progress on high precision calculations for the ground state of atomic lithium. *Journal of Molecular Structure: THEOCHEM*, 400:7 – 56, 1997. Ab Initio Benchmark Studies.

[159] R. D. Hudson and Virginia L. Carter. Atomic absorption cross sections of lithium and sodium between 600 and 1000 å∗. *J. Opt. Soc. Am.*, 57(5):651–654, May 1967.

[160] George McGinn. Atomic and molecular calculations with the pseudopotential method. vii onevalenceelectron photoionization cross sections. *The Journal of Chemical Physics*, 53(9):3635–3640, 1970.

[161] P.G. Burke and W.D. Robb. The r-matrix theory of atomic processes. *Advances in Atomic and Molecular Physics*, 11:143 – 214, 1976.

[162] J.N. Bardsley. Pseudopotential calculations of alkali interactions. *Chemical Physics Letters*, 7(5):517 – 520, 1970.

[163] G Peach, H E Saraph, and M J Seaton. Atomic data for opacity calculations. ix. the lithium isoelectronic sequence. *Journal of Physics B: Atomic, Molecular and Optical Physics*, 21(22):3669, 1988.

[164] Peter Schwerdtfeger. Table of experimental and calculated static dipole polarizabilities for the electronic ground states of the neutral elements (in atomic units). 2016.

[165] M. Ya. Amusia, N. A. Cherepkov, Dj. Živanović, and V. Radojević. Photoabsorption for helium, lithium, and beryllium atoms in the random-phase approximation with exchange. *Phys. Rev. A*, 13:1466–1474, Apr 1976.

[166] Qi Yue-Ying, Wu Yong, Wang Jian-Guo, and Ding Pei-Zhu. Calculations of photo-ionization cross sections for lithium atoms. *Chinese Physics Letters*, 25(10):3620, 2008.

[167] Charlotte Froese Fischer. A general multi-configuration Hartree-Fock program. *Computer Physics Communications*, 14(12):145 – 153, 1978.

[168] C.F. Bunge, J.A. Barrientos, and A.V. Bunge. Roothaan-hartree-fock ground-state atomic wave functions: Slater-type orbital expansions and expectation values for z = 2-54. *Atomic Data and Nuclear Data Tables*, 53(1):113 – 162, 1993.

[169] Jens Oddershede and John R. Sabin. Orbital and whole-atom proton stopping power and shell corrections for atoms with $z \leq 36$. *Atomic Data and Nuclear Data Tables*, 31(2):275 – 297, 1984.